The Dissertation Committee for Xin Wang Certifies that this is the approved version of the following dissertation:

Monte Carlo Simulation of Charge Transport in Si-based Heterostructure Transistors

Committee:

Sanjay Banerjee, Supervisor

Leonard F. Register

Jack Lee

Dean Neikirk

Graham F. Carey

Monte Carlo Simulation of Charge Transport in Si-based Heterostructure Transistors

by

Xin Wang, B.S., M.S.

Dissertation

Presented to the Faculty of the Graduate School of
The University of Texas at Austin
in Partial Fulfillment
of the Requirements
for the Degree of

Doctor of Philosophy

The University of Texas at Austin
May, 2002

To my parents and wife

Acknowledgements

I would like to thank my supervisor, Dr. Sanjay K. Banerjee, for his encouragement, patience and stimulating guidance. In the past four years, I have been impressed by his wide knowledge, strong curiosity to acquire new knowledge and enthusiasm for research. He gave me great academic freedom in my research, which helped me gradually establish independent research ability. It is very important for my academic training as a graduate student.

I also like to thank professor Leonard F. Register. Although I met him less than two years ago, I am very impressed by his knowledge and experience in research, enthusiasm towards research and generosity of time towards students. His supervision played an irreplaceable role in my work. I gained a lot of knowledge and experience from stimulating and fruitful discussions with him.

I would like to express my sincere appreciation to a special colleague, Dr. Brian Winstead. In the last year of my graduate study, we had pleasing and fruitful collaboration on the development of MOCA. He introduced MOCA into my research world and patiently helped me to become familiar with it. It set up a solid base for my later work.

Lots of colleagues and friends have given me help and shown me a good time during my time at the Microelectronics Research Center. My thanks go to David L. Kencke, Siva Mudanai, Qiqing Ouyang, Xiaofeng Fan, Haihong Wang, Yang-yu Fan, Kou-chen Liu, Xiangdong Chen, Wenjie Qi, Renee Nieh, Xiao

Chen, Tat Nagi, Zhengmao Ye, Huang Hua, Shuling Wang, Bo Yang, Feng Ma, Zengzong Zou, Qinwei Mo, Xiaoguang Sun and Hao Chen.

My gratitude also goes to my doctoral committee. Finally, I am deeply indebted to my parents, brother and lovely wife. Their consideration, support and understanding are the most powerful motivations for my research.

Xin Wang
The University of Texas at Austin
April, 2002

Monte Carlo Simulation of Charge Transport in Si-based Heterostructure Transistors

Publication No._____________

Xin Wang, Ph.D.
The University of Texas at Austin, 2002

Supervisor: Sanjay K. Banerjee

Strain and bandgap engineering of strained materials has emerged as an important technique for improving the device performance other than conventional scaling method. The purpose of this work is to develop a Monte Carlo simulation tool to investigate properties of these strained materials and carrier transport in deep submicron novel devices with heterostructures and strained materials.

A general full-band Monte Carlo simulation tool with high flexibility about device structure and material profiles is developed for the first time. The transport model is based on energy-dependent scattering rates including inelastic acoustic phonon scattering with longitudinal and transverse modes, optical phonon scattering, impact ionization, surface roughness scattering, impurity scattering and alloy scattering. The full-band treatment for strained material model substantially advances the state-of-the-art method relying on simpler valley model for the scattering rates. The multi-material profiles in devices are treated with parameterization of band structure. The tunneling across a potential barrier is treated with Feynman's effective potential scheme.

An orthorhombically-strained silicon (OS-Si) is reported in this work. The six degenerate valleys in OS-Si near X points break into three pairs with different energy minima due to the orthorhombic strain. Thus the drift velocity is enhanced under an electric field transverse to the longitudinal-axis of the lowest valleys. The OS-Si grown on a compressively-strained $Si_{0.6}Ge_{0.4}$ sidewall has a mobility almost twice that of bulk Si and electron saturation velocity approximately 20% higher.

For homogenous strained silicon on $Si_{0.7}Ge_{0.3}$ (001), in-plane mobility of 2670 $cm^2/(Vs)$ for electrons is obtained, with enhancement by a factor of 1.8 compared to the unstrained case. Electron transport in a strained Si nMOSFET with 50 nm channel length is also investigated by full-band Monte Carlo. Strained silicon devices exhibit around 60% increase of drain current compared to unstrained silicon. Strained SiGe is also studied with full-band Monte Carol tool. A 90% enhancement in hole mobility is obtained for strained $Si_{0.7}Ge_{0.3}$ compared with bulk Si. The preliminary investigation of hole transport in vertical pMOSFETs with graded SiGe channel is also reported in this work.

Table of Contents

CHAPTER FOUR 65

CHAPTER FIVE 91

CHAPTER SIX 125

List of Tables

List of Figures

CHAPTER ONE

Introduction

In recent years, tremendous development has been made to improve the device performance of Si-based devices, e.g., higher density, faster speed and lower power dissipation. In conventional Si-based metal oxide semiconductor field effect transistors (MOSFET's), the device and process technologies have almost been pushed to the limit. New materials are needed to achieve even better device performance. The new materials and device structures should not only provide favorable electrical properties but also offer compatibility with the mature and robust Si technology to achieve cost effectiveness. In addition, in the optoelectronics area, they should be competitive with GaAs, an alternative material with high speed and desirable optoelectronic properties but high cost compared with Si.

Compared with Si, Ge, iso-electronic with Si, has a similar band structure with smaller electron and hole effective masses and narrower band gap. The lattice mismatch between Ge and Si is 4%, and Ge is completely miscible with Si. It is feasible to grow SiGe alloys with any magnitude of Ge mole fraction. It is known that the fundamental band gap of bulk SiGe alloys is smaller than that of Si [Bra58], and the effective masses are smaller [Peo84]. Additionally these features can be engineered by adjusting the Ge mole fraction in the alloy. Thus SiGe is a feasible candidate compatible with current Si technologies in enhancing the device properties of semiconductor devices.

In the past, two types of SiGe-based materials, strained SiGe and strained Si grown on a bulk SiGe substrate, have been studied and applied to semiconductor devices. It has been demonstrated that a high-quality compressively strained SiGe alloy layer, grown on (100) plane of a bulk silicon substrate, can be fabricated by molecular beam epitaxy (MBE) [Bea84] and chemical vapor deposition (CVD) [Gre86]. If the strained SiGe layer is kept sufficiently thiner than the critical thickness of SiGe alloy (around 200 Å for Ge content 0.4 at 873 K [Peo86]), the SiGe/Si interface is free of misfit dislocations and the lattice mismatch in the structure is accommodated by coherent layer strain. Due to the larger lattice constant of bulk Ge than that of Si, the pseudomorphic SiGe alloy layer is compressively strained (CS). The band structure of a CS-SiGe layer with the mole fraction of Ge below 0.85 remains Si type. But the strain lifts the degeneracy at the band edges, six-fold for conduction band and two-fold for valence band, as shown in Fig. 1.1. In the conduction band of CS-SiGe (Fig. 1.1(a)), four Ä$_4$ valleys around X points on the growth plane (100) move down in energy, while two Ä$_2$ valleys along the growth direction move up. Thus more electrons occupy the in-plane Ä$_4$ valleys. To a first-order approximation, the effective mass components of the Ä valleys are unchanged under the strain. So the average effective mass component along the growth direction is lower, and the mobility in that direction should be enhanced. In addition, the degeneracy lifting suppresses *f*-type intervalley scattering between neighboring Ä valleys, which enhances the mobility too. But alloy scattering may degrade that enhancement. In the direction parallel to the growth plane the mobility is lower than that of bulk Si, due to higher average effective mass and alloy scattering. In the valence band of CS-SiGe (Fig. 1.1(b), the heavy-hole (HH) valley moves up in energy above the light hole (LH), and the heavy-hole effective mass is decreased [Man91] under the strain. It is reported the hole mobilities in CS-SiGe are enhanced by 50% over that of Si at room temperature [Gar91], even though alloy scattering degrades the gain from less interband scattering and smaller hole effective mass. The indirect band gap of CS-SiGe is lowered further from that of bulk SiGe which itself is narrower than that of bulk Si. The band gap of CS-SiGe spans the 1.30 ìm to 1.55 ìm range [Bra58], which makes such alloys extremely attractive for applications involving long wavelength integrated optoelectronics [Mur95].

A tensily strained Si layer is fabricated in a similar way as CS-SiGe. It is grown on a relaxed or strained SiGe alloy layer. When grown on a (100) relaxed SiGe substrate, the strained Si layer is tetragonally tensily-strained (TS). Similarly the strain lifts the degeneracy of the conduction and valence band edges, as shown in Fig. 1.2. In the conduction band of TS-Si, the four-fold in-plane Ä$_4$ valleys move up in energy, while the Ä$_2$ valleys in growth direction move down and can accommodate more electrons. Also less *f*-type intervalley scattering occurs. Thus, TS-Si has higher in-plane electron mobility. The hole mobility of TS-Si is also high, because the light-hole valley moves up and there is less inter-band scattering.

In addition, heterostructure concepts can be incorporated into Si technology by using SiGe. The band offsets in a heterojunction allow the realization of a number of heterostructure devices, modulation doped field effect transistors (MODFET's), heterojunction bipolar transistors (HBT's), p-i-n photodetectors and novel MOSFETs with strained SiGe in source/drain or channel. For example, in a MODFET made of CS-SiGe/bulk Si heterostructure, because of the higher valence band edge in CS-SiGe than in bulk Si, holes are confined in the CS-SiGe layer and have higher mobility.

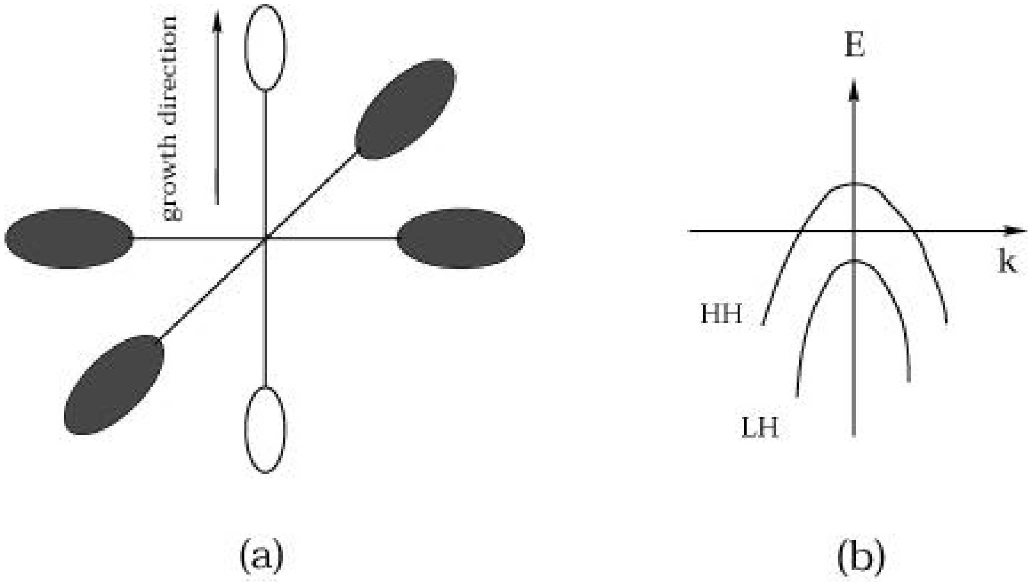

Figure 1.1. (a) Schematic equi-energy surfaces of the six split valleys in the first conduction band in CS-$Si_{1-x}Ge_x$. The minimum energies of the dark valleys are lower than those of the open ellipsoids. (b) Schematic energy diagrams of heavy hole (HH) and light hole (LH) bands in CS-$Si_{1-x}Ge_x$

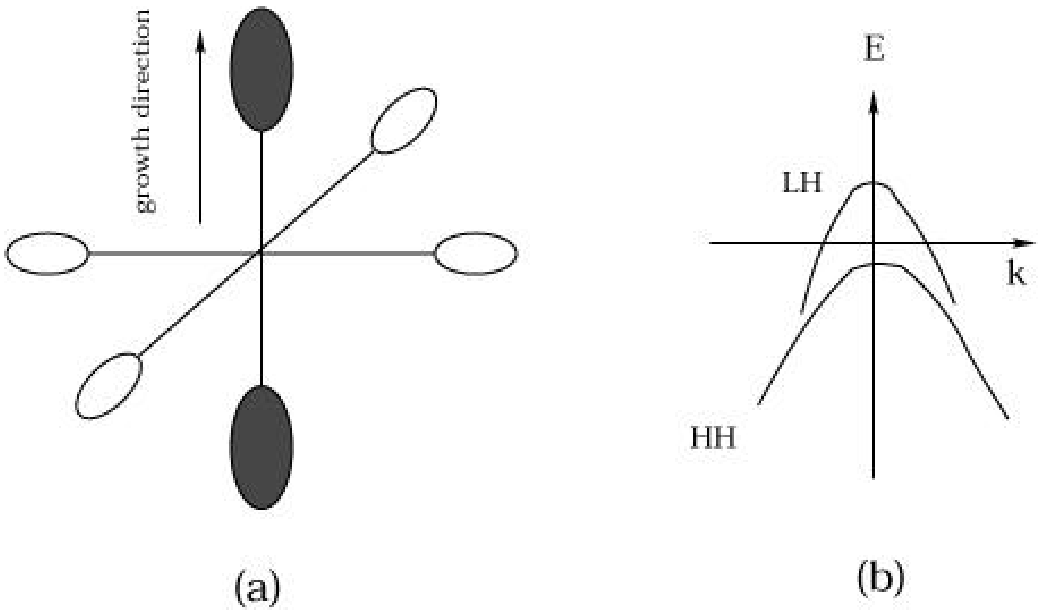

(a) (b)

Figure 1.2. (a) Schematic equi-energy surfaces of the six split valleys in the first conduction band in TS-Si. The minimum energies of the dark valleys are lower than those of the open ellipsoids. (b) Schematic energy diagrams of heavy hole (HH) and light hole (LH) bands in TS-Si.

Effective SiGe-based device design is ultimately based on the understanding of band structures of the materials, band offsets at the heterojunctions and accurate simulation of carrier transport in the device. This work focuses on the theoretical calculation of the band structure and band offsets, and on Monte Carlo (MC) simulation of transport properties in SiGe-based devices. The band structures of a strained Si or strained SiGe layer with various stresses are calculated by a variety of methods: first-principles density-functional theory (DFT); empirical pseudopotential (EP) calculation and tight binding (TB) calculation. The band offsets can be obtained by a first-principles calculation or model-solid theory. Among the existing device simulation methods, the MC technique is capable of providing us more complete understanding of the carrier transport than drift-diffusion or hydrodynamic transport models. Although it requires appreciable computer resources, the simplicity of implementation and relatively complete description of semi-classical transport make the MC method appealing for semiconductor simulation. In order to describe the charge transport in a device consisting of strained materials and heterostructures, the existing UT MC simulation codes (slapshot and utmc) and UIUC MC code (MOCA) have been modified to handle heterostructure devices. In this work, three Si-based materials (OS-Si, TS-Si and CS-SiGe) have been studied by MC simulations.

The next chapter describes the theoretical models for calculating atomic and band structures of the strained material, band offsets at heterojunction and charge transport properties in MC. Chapter 3 presents the electron transport properties of OS-Si studied by modified slapshot. Chapter 4 and 5 describe the simulated material properties and device features of TS-Si and CS-SiGe, respectively. The conclusions and recommendations are in the last chapter.

CHAPTER TWO

Theoretical Models

2.1 ATOMIC STRUCTURE OF A STRAINED LAYER

It is possible to grow a dislocation-free, strained thin epitaxial layer on a elementary or alloy substrate involving different bulk lattice constants from that of the substrate. The lattice mismatch is accommodated totally by strain. Thus, in studying the atomic structure of the strained layer, we assume the interface between the substrate and the epitaxial layer is ideal, i.e., the in-plane lattice constants are the same across the interfaces. The normal lattice constants can be determined by minimizing the macroscopic elastic energy, according to a study of quantum-mechanical energy minimization of a macroscopic system [Wal86] and confirmed by experimental observation [Fel87]. For instance, in strained **Si**$_{1-x}$Ge$_x$ grown on a bulk <100> Si substrate, the parallel lattice constant of Si$_{1-x}$Ge$_x$ a$_{SiGe,}$ (x) reduces to match that of bulk silicon a$_{Si,o}$ at the interface from the bigger lattice constant a$_{SiGe,o}$(x) of relaxed SiGe, and the perpendicular lattice spacing a$_{SiGe,}$ (x) is determined according to elasticity theory. This generates the following results:

$$a_{SiGe,//}(x) = a_{Si,o}\ , \tag{2.1a}$$

$$a_{SiGe,\perp}(x) = a_{SiGe,o}(x)\left(1 - \frac{2C_{12}(x)}{C_{11}(x)}\frac{a_{Si,o} - a_{SiGe,o}(x)}{a_{SiGe,o}(x)}\right), \tag{2.1b}$$

where the elastic constants of $Si_{1-x}Ge_x$, $C_{11}(x)$ and $C_{12}(x)$, are approximated by Vegard's law, the linear interpolation of those of bulk Si and Ge. In this work, x of $Si_{1-x}Ge_x$ refers to the Ge mole fraction in the strained $Si_{1-x}Ge_x$ layer. The bulk lattice and elastic constants [Mcs53] of Si and Ge are listed in Table 2.1.

Material	Si	Ge
a (Å)	5.43	5.65
C_{11} (Mbar)	1.68	1.32
C_{12} (Mbar)	0.65	0.49

Table 2.1. Lattice constants a and elastic constants C_{11} and C_{12} for silicon and germanium.

2.2 BAND STRUCTURE CALCULATION

The band structure of a semiconductor is one of the most important inputs into a Monte Carlo simulation. Three band structure calculation methods have been investigated and employed in this work. These methods can be classified into two categories: empirical method and first-principles calculation. Density-functional theory (DFT) belongs to first-principles calculation. The empirical methods include empirical pseudopotential method (EPM) and tight-binding (TB) calculation. Generally, the empirical methods are simpler and require much less number of parameters than first-principle method. So they require less computation time and resources. But those parameters are adjusted to fit experimental measurement, which may limit their usage. On the contrary, first-principles calculation is quite general and can be used to almost any environment, which is attributed to the no fitting parameter requirement. The trade off is its high computational requirements. It usually takes more time and memory to obtain band structures. So large unit cells are only feasible at the cost of a reduction in the precision of results. The following introduce the theory details of these methods.

2.2.1 Density-functional theory

A first-principles method without adjustable parameters is an ideal approach for the strained system lacking experimental results to be fitted to. In recent years, progress in DFT [Hoh64] [Koh65] has made it possible to calculate properties of solids from first principles. It is widely used to study the motion of nuclei, thermodynamic properties and electronic properties of molecules, bulk materials and surfaces [Bur95] [Boc95] [Kac94]. The key variable in DFT is the electron density *n(r)*. The ground state energy $E_0(\{R_J\})$ of an equilibrium system with given positions of the nuclei R_J is the minimum of the Kohn-Sham (KS) total-energy functional [Hoh64] [Koh65] with respect to the electron density. The total ground-state energy $E[n]$ is

$$E[n] = T^s[n] + E^H[n] + E^{e-nuc}[n] + E^{XC}[n] + E^{nuc-nuc}, \tag{2.2}$$

where T^s is the kinetic energy of non-interacting electrons, E^H is the Hartree energy, E^{e-nuc} is the electron-nuclei interaction energy, E^{XC} is the exchange-correlation energy, and $E^{nuc-nuc}$ is the nuclei-nuclei energy. After minimizing the total energy with respect to the electron density, the corresponding effective one-electron Schrödinger equation, also called the Kohn-Sham (KS) equation, is

$$\left(-\frac{1}{2}\nabla^2 + V^{e-nuc}[n] + V^H[n] + V^{XC}[n]\right) f_a(r) = e_a f_a(r), \tag{2.3}$$

where V^{e-nuc} is the electron-nuclei interaction, and V^{H} and V^{XC} are the Hartree and exchange-correlation terms, respectively. The eigenstate $f_a(r)$ is the wave function of an electron in the ground state, and e_a is the corresponding DFT eigenvalue. Also the electron density is obtained by

$$n(r) = \sum_a f_a \left| f_a(r) \right|^2 , \tag{2.4}$$

where f_a is the occupation number.

The band structure calculated by DFT does not fully account for the quasi-particle energy, which is the change in the total energy of a system after adding or removing one electron. It is given by solving a quasi-particle equation [Hed69]

$$\left[-\frac{1}{2}\nabla^2 + V^{e-nue}(r) + V^{H}(r) - E_{quasi} \right] y(r) + \int \Sigma(r, r^{'}, E_{quasi}) y(r^{'}) dr^{'} = 0 , \tag{2.5}$$

where $\Sigma(r, r^{'}, E_{quasi})$ is the self-energy operator. While studies on the relation between quasi-particle energy and DFT eigenvalues of Si [God88] [Bec92] show that DFT underestimates the band gap, a Monte Carlo transport simulation mainly uses only information about the electron valence or conduction bands, not the band gap, except for impact ionization processes (in these processes, the experimental energy gap is used). The conduction bands of DFT are at most 5% different at , L and X points from those of quasi-particle theory [Bec92]. So the DFT approach is sufficient to provide an accurate description of the electron band structure for the MC simulation.

Also, since there are no adjustable parameters, it makes DFT more easily applicable to a strained material with arbitrary symmetry. A well-tested DFT package [Boc97] was used. We iteratively solve the KS equation Eq. (2.3) to get a self-consistent ground state electron density with minimum total energy. The exchange-correlation term term V^{XC} is treated by a local-density approximation (LDA) [Cep80] [Per81], and non-local norm-conserving pseudopotentials [Bac82] [Ham89] in the fully separable Kleinman-Bylander form [Kle82] describe the electron-nuclei interaction term V^{e-nue}. Electron waves are expanded by plane waves, the number of which is determined by a cut-off energy. Integration in momentum space is approximated as a weighted summation of a number of special k-points [Mon76] in the irreducible Brillouin zone (BZ).

In an alloy system, e.g., SiGe alloy, Ge atoms are randomly distributed among Si atoms. The positions of Ge atoms can be determined by minimizing the total energy of the alloy using molecular dynamics (MD). But MD is time-consuming. Kelires and Tersoff [Kel89] employed a set of empirical interatomic potentials to model interactions between atoms (Si-Si, Ge-Ge and Si-Ge) and use a MC algorithm to flip the entity (Si or Ge) at every lattice point to minimize the total energy. Although this method can provide positions of Ge atoms in a random SiGe alloy, it often needs a larger supercell to accommodate various alloy profiles. So in DFT calculation of band structure, a large number of special k-points is needed, requiring more computer memory; also the folded band structure is not suitable for a MC transport simulation. Chen employed the virtual-crystal approximation (VCA) [Che80] to treat the randomness. In VCA, the lattice point of an alloy is not occupied by the constituent atoms but an interpolated atom representing the randomness. Consequently, based on Vegard's law, a set of interpolated pseudopotentials is generated from the pseudopotentials of the constituent atoms for DFT. The new set of pseudopotentials represents the interaction between an electron and an “averaged” atom.

2.2.2 Empirical Pseudopotential Theory

Empirical pseudopotential method is widely used to calculate the band structures of bulk elementary semiconductors [Che76]. In face-centered cubic (FCC) material like bulk Si with lattice constant a_0, due to the symmetry of FCC, the band structure is determined by the first three non-zero empirical pseudopotential $V(q)$ at three sets of reciprocal lattice points $q = \sqrt{3}$, $\sqrt{8}$ and $\sqrt{11}(2p / a_0)$ which are adjusted to match the electronic energies of symmetry points in principal directions with the experimental excitation spectrum of the bulk. In strained materials, besides the above three non-zero empirical pseudopotentials, the pseudopotentials at other q points also contribute to the band structure caused by symmetry breaking of FCC unit cells. Lacking the experimental excitation spectrum for a strained solid with various strain levels, those extra non-zero pseudopotentails are obtained by interpolating the values at above three points with the form [Fri89]:

$$V_a(q) = \frac{a_1(q^2 - a_2)}{e^{a_3(G^2 - a_4)} + 1}\left[\frac{1}{2}\tanh\left[\frac{a_5 - q^2}{a_6}\right] + \frac{1}{2}\right], \tag{2.6}$$

where $V(q)$ is normalized by the cell volume and the tanh part ensures a fast cutoff for large values of q. The interpolation parameters [Fri89] $a_1 - a_6$ are listed in Table 2.1 in atomic units. The validation of Eq. (2.6) and its parameters are justified by Fridel, et al [Fri89] for Si and Ge.

In this work, we modified the empirical pseudopotential band structure calculation code for bulk Si to a general version capable of studying strained material by employing Eq. (2.6). In the calculation, cutoff energy 10Ry is used to ensure convergence. Also in SiGe alloy, the pseudopotentials are obtained by linear interpolation between Si and Ge.

	a_1	a_2	a_3	a_4	a_5	a_6
Si	106.0686	2.2278	0.6060	-1.9720	5.0	0.3
Ge	54.4512	2.3592	0.7400	-0.3800	5.0	0.3

Table 2.2. The interpolation parameters for pseudopotentials of Si and Ge.

2.2.3 Tight-binding Theory

Tight-binding (TB) technique [Che80] is another widely-used method in band structure calculation attributed to its intuitive simplicity, realistic description of structural and small sets of basis functions [Maj87]. In the empirical TB method, a matrix representation of the Hamiltonian between atomic-like orbitals is constructed where the matrix elements are adjusted to fit experimental energy bands. In minimal sp^3 basis and nearest-neighbor interactions, it can satisfactorily reproduce valance-band dispersion relation, while it fails to calculate the conduction band. Richardson and co-workers [Ric87] showed that the unoccupied atomic *d* states contribute the *d* symmetry character in charge density at X, Ã and L of conduction band. So the s^* and *d* states are included in the minimal sp^3 basis to mimic the d states contribution. In this work, we employed Staele and Vogl's TB code with $sp^3d^5s^*$ basis and the on-site energies and coupling parameters in TB provided by [Jan98]. To describe the strain effect on the band structures, the matrix elements of Hamiltonian are scaled with respect to the bond-angle distortion and bond-length change. Due to the weak variation of the on-site energies [Jan98], the on-site energies are kept constant. The two-center coupling parameters V_{ijk} between the atomic wave functions i and j are scaled based on a generalization of Harrison's d^{-2} law [Ren82]:

$$V_{ijk}(d) = V_{ijk}(d_0)\left(\frac{d_0}{d}\right)^{n_{ijk}}, \tag{2.7}$$

where d and d_0 are the bond length of strained and unstrained materials, respectively. Orbital-dependent exponents n_{ijk} reflect the localization of interatomic interaction. Ref. [Jan98] lists the fitted values of n_{ijk} to reproduce the experimental measurements of deformation potentials.

2.3 BAND OFFSET CALCULATION

Band offsets between two layers at a heterojunction is the discontinuity in energy band edge. It is of crucial importance for a heterojunction device, and theoretically can be obtained from a first-principles calculation and model-solid theory. The fundamental problem in calculating the band offsets at the heterojunction is that for a bulk solid, there is no unique reference with which to compare the potentials for two different solids [Van86], because of the long range of the Coulomb interaction, the zero energy is undefined for an infinite crystal.

2.3.1 First-principles calculation of band offsets

In a first-principle calculation, a heterojuction is modeled by a periodic superlattice with a supercell (Fig. 2.1) consisting of substrate material, say relaxed (R) Si, on one side of an interface and strained layer material (SiGe) on the other side. Of course, what we are interested in is an isolated interface. If the interested quantities, e.g., electrostatic potential, are not changed with the increase of the size of the supercell, a limited-atom supercell can model the isolated interface. The atom structure in the supercell is determined by elastic theory and empirical interatomic potentials [Kel89] (for an alloy layer).

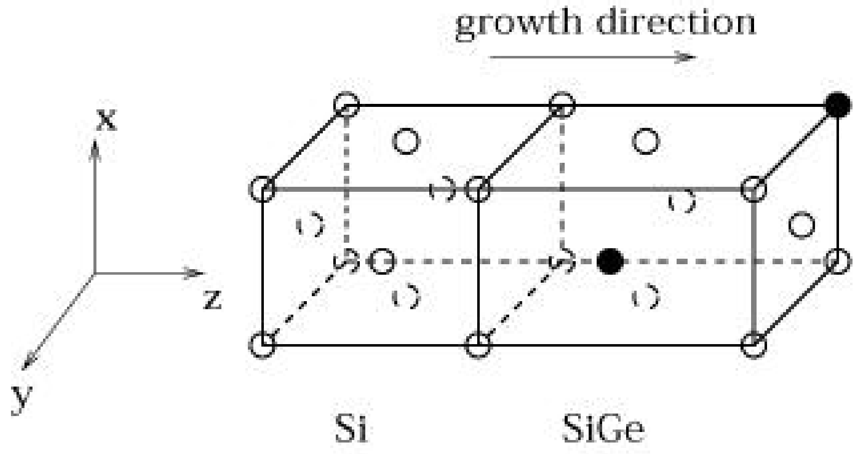

Figure 2.1. Schematic of a supercell consisting of R-Si/CS-$Si_{1-x}Ge_x$ heterojunction, filled circles representing Ge atoms and open circles representing Si atoms.

A first-principles DFT calculation for the superlattice (Fig. 2.1) generates electrostatic potential, sum of ionic, Hartree and exchange and correlation potentials, throughout the supercell. After averaging the in-plane (x-y plane) components, only potential depending on the growth direction (along z direction), perpendicular to the interface, is left. Fig. 2.2 shows the average potential (solid line) along z direction for a 32-atom supercell with eight Ge atoms on the SiGe side modeling a $Si/Si_{0.5}Ge_{0.5}$ heterojunction. We note that a dipole momentum is set up around the junction. The potential is distorted around the heterojunction, while in the region away from the interface, it converges to that of bulk material (shown later) and we have average values V_{Si} and V_{SiGe}. In order to calculate the band offsets between two materials, DFT is used again to calculate the electrostatic potentials and band edges of isolated systems, substrate and strained layer, with the same atomic structure as those in the supercell. After matching the electrostatic potentials for isolated materials (dashed line in Fig. 2.2) with those for supercell (solid line in Fig. 2.2), we note that one layer away from the interface the potential assumes the form of the bulk potential. Thus the band edge discontinuities, band offsets, can be obtained from the average potential shift $V=V_{\mathrm{Si}}-V_{\mathrm{SiGe}}$ and difference between the band edges and the average potential V shown in Fig. 2.3. Although there is no unique reference with which to compare the potentials for two different solids, the above procedure only uses the energy difference from the same DFT calculation.

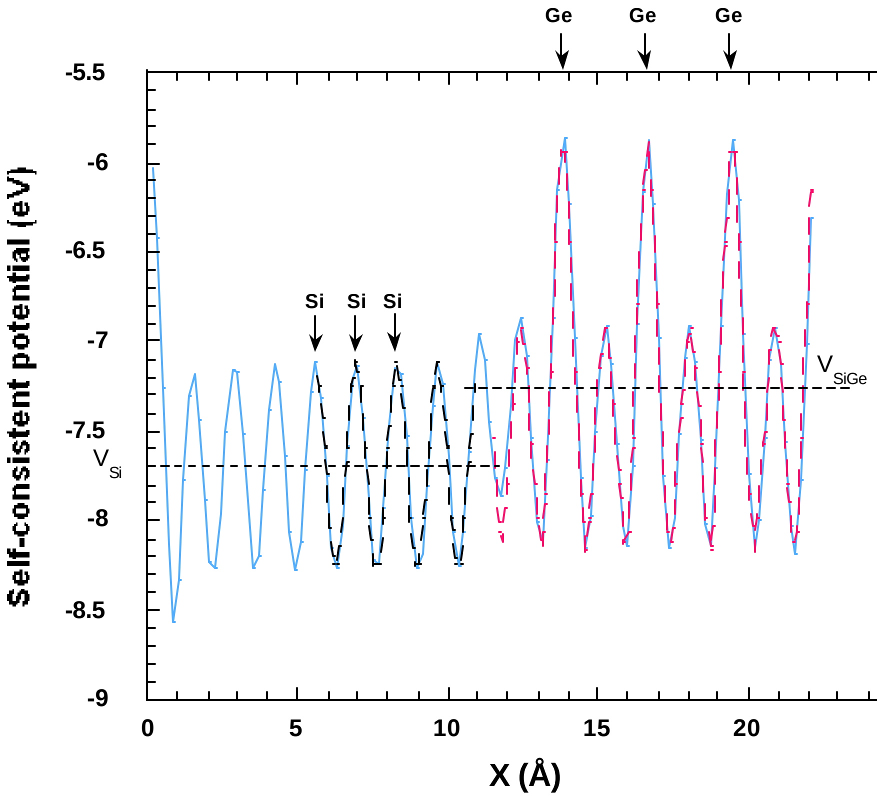

Figure 2.2. Average electrostatic potentials across the R-Si/CS-$Si_{0.5}Ge_{0.5}$ heterojunction along growth direction.

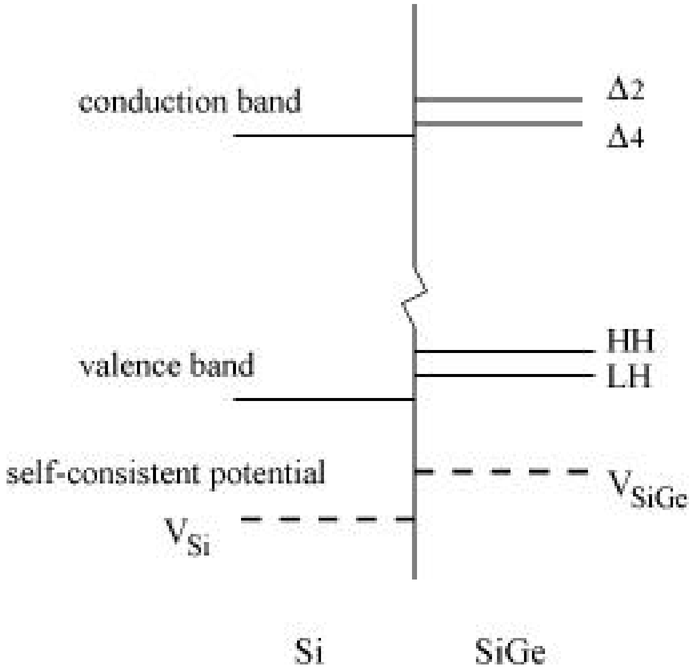

Figure 2.3. Schematic band line up at a R-Si/CS-SiGe interface.

As mentioned in Sec. 2.2.1, the band gap from DFT is severely underestimated and the conduction band should be shifted up according to experimental results. In the calculation for conduction band offset, due to the same energy gap correction of DFT for Si and Ge [Van86], the conduction band offset from direct comparison is reliable.

Fig. 2.4 shows the band offsets between Si substrate and a CS-SiGe alloy layer. The band offsets from DFT are in good agreement with the experimental results [Nau92] and the interpolated theoretical results between Si/Si and Si/Ge interface [Van86].

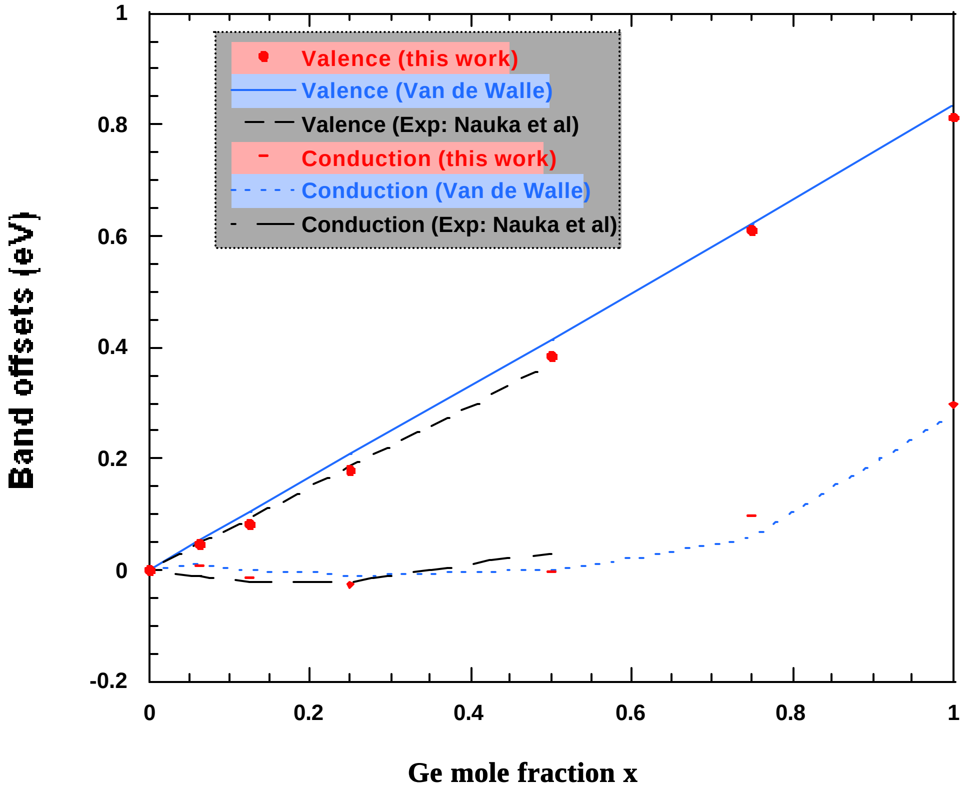

Figure 2.4. Conduction and valence-band offsets of bulk Si/CS-SiGe heterojunctions.

2.3.2 Model-solid theory

Although it is possible to perform first-principles calculations to obtain band offsets at a heterojunction, the computational complexity is very high, which limits its use as a tool in the design of novel heterostructures. Particularly in the case of strained-layer or alloy interfaces, carrying out a self-consistent calculation for every imaginable strain and alloy configurations is not feasible. This illustrates the need for a reliable model theory that can predict band offsets for a wide variety of interfaces without the need for heavy calculation. Van de Walle's model-solid theory [Van89] is one of these models. The model-solid theory has two aspects: first, the generation of energy of band edges in conduction and valence bands for strained (and alloy) materials, and second, the alignment of the band edges on an ``absolute" scale.

The first part is accomplished by performing the DFT calculations on individual unstrained semiconductors. Although the deficiency of the DFT calculation is the underestimated band gap, the correct conduction-band edge of bulk semiconductor can be obtained by using experimental results. Van de Walle provided the energy band edges of most bulk semiconductors in [Van89]. Then the strain-induced shift and splittings of the band edges are added to the band edges of the bulk materials. The shift- and splitting-change of the band edges can be generated from deformation potentials obtained from experimental results or the DFT calculation. In the following, we focus on band edge change for strained Si or SiGe alloy. The valence-band edge, $\tilde{A}$ ($k = 0$) point, of Si is six-fold degenerate in the absence of spin and stress, and transforms as $\tilde{A}_{25}^{+}$ of the cubic group O_h [Kos57]. The inclusion of spin-orbit coupling splits the degenerate states into a fourfold ($J = \frac{3}{2}$) state, heavy and light holes, and a twofold state, spin-orbit state ($J = \frac{1}{2}$), J being the total angular momentum. The strains, hydrostatic and shear, further shift the band edges and lift the degeneracy. The hydrostatic strain causes the shift of the band edges due to the volume change of the strained layer, while the shear strain splits the degenerate states. The shift and splitting of the band edges are described by a strain Hamiltonian. At $\tilde{A}$ ($k = 0$) point of the valence band of Si-like material stressed along <100>, the strain Hamiltonian [Has63] is simplified to

$$\begin{aligned} H &= D_d^v(e_{xx}+e_{yy}+e_{zz}) \\ &+ 2D_u\left[\left(I_x^2-\tfrac{1}{3}I^2\right)e_{xx}+\left(I_y^2-\tfrac{1}{3}I^2\right)e_{yy}+\left(I_z^2-\tfrac{1}{3}I^2\right)e_{zz}\right], \\ &+\frac{1}{3}\Delta_0 I\bullet \boldsymbol{s} \end{aligned} \tag{2.8}$$

where D_d^v is the hydrostatic deformation potential pertinent to the fractional volume change $e_{xx}+e_{yy}+e_{zz}$, e_{xx}, e_{yy} and e_{zz} are diagonal components of strain tensor, D_u is the deformation potential related to uniaxial strain, I_x, I_y and I_z are the components of the orbital angular momentum operators, I^2 is the square of the magnitude of the orbit angular momentum, that is $I^2=I_x^2+I_y^2+I_z^2$, Δ_0 is the spin-orbit coupling parameter, and $\boldsymbol{s}$ denotes the Pauli spin.

Using a basis composed of the states $\left|\tfrac{3}{2},\pm\tfrac{3}{2}\right\rangle$, $\left|\tfrac{3}{2},\pm\tfrac{1}{2}\right\rangle$ and $\left|\tfrac{1}{2},\pm\tfrac{1}{2}\right\rangle$, which are the eignstates of total angular momentum $J=I+\tfrac{1}{2}\boldsymbol{s}$ and its magnetic component M_J, the strain Hamiltonian at Γ can be represented by 6×6 matrix

$$\begin{aligned} H &= D_c^v(e_{xx}+e_{yy}+e_{zz})\vec{I} \\ &+\begin{bmatrix} \frac{\Delta_0}{3}+\boldsymbol{e} & 0 & -\boldsymbol{e}_1 & 0 & 0 & \sqrt{2}\boldsymbol{e}_1 \\ 0 & \frac{\Delta_0}{3}-\boldsymbol{e} & 0 & \boldsymbol{e}_1 & \sqrt{2}\boldsymbol{e} & 0 \\ -\boldsymbol{e}_1 & 0 & \frac{\Delta_0}{3}-\boldsymbol{e} & 0 & 0 & \sqrt{2}\boldsymbol{e} \\ 0 & \boldsymbol{e}_1 & 0 & \frac{\Delta_0}{3}+\boldsymbol{e} & -\sqrt{2}\boldsymbol{e}_1 & 0 \\ 0 & -\sqrt{2}\boldsymbol{e} & 0 & -\sqrt{2}\boldsymbol{e}_1 & -\frac{2\Delta_0}{3} & 0 \\ \sqrt{2}\boldsymbol{e}_1 & 0 & \sqrt{2}\boldsymbol{e} & 0 & 0 & -\frac{2\Delta_0}{3} \end{bmatrix}, \end{aligned} \tag{2.9}$$

where $\vec{I}$ is an unit 6×6 matrix, $\boldsymbol{e}=\frac{2}{3}D_u(e_{zz}-\frac{e_{xx}+e_{yy}}{2})$ and $\boldsymbol{e}_1=\frac{2}{3}D_u(\frac{e_{xx}-e_{yy}}{2})$. The eignvalues of the strained Hamiltonian give the energies of heavy, light holes and spin-orbit states in the strained material. As mentioned previously, the alloy effect is treated by interpolation (VCA).

In the conduction band of a Si-like material, the conduction band edges are $0.85\frac{2p}{a}$ away from the Ã points in $\langle 100\rangle$ directions. The lowest six-fold valleys of conduction bands at the band edges also experience shift under a stress. The energy shift ΔE_c^i of valley *i* can be described by [Bal65]

$$\Delta E_c^i = \left[\Xi_d \vec{I} + \Xi_u \{\hat{a}_i \hat{a}_i\}\right] : \vec{e} \, , \tag{2.10}$$

where Ξ_d and Ξ_u are the dilation and uniaxial deformation potentials of the lowest valleys, respectively, $\hat{a}_i$ is a unit vector parallel to the k vector of valley *i*, $\hat{a}_i \hat{a}_i$ denotes a dyadic product, and $\vec{e}$ is the strain tensor.

The second aspect of model-solid theory is of establishing an absolute energy scale. Since typical bulk calculation is carried out in an infinite crystal, no vacuum level is available as an absolute common reference. In model-solid theory, the common reference is accomplished by modeling the solid as a superposition of neutral atoms. In each atom, the electrostatic potential of material is rigorously defined with respect to the vacuum level. Thus, the average electrostatic potential is, by superposition, also well defined on the absolute energy scale. In the calculation of the electrostatic potential of each atom, the same *ab inito* pseudopotential as that in the DFT calculation of band edges for bulk solid is used. Since the obtained band-edge energy is also referred to the average electrostatic potentials, the band offsets can be obtained by alignment of the average electrostatic potentials of the bulk semiconductors in the heterojunction. The spin-orbit splittings Δ_0, average $E_{v,av}$ and the deformation potentials [Van89] of conduction band valence bands and for Si and Ge are listed in Table 2.2.

	$E_{v,av}$ (eV)	$_0$ (eV)	D_u (eV)	D_d (eV)	$\hat{I}_u$ (eV)	$\hat{I}_d$ (eV)
Si	-7.03	0.04	2.46	3.53	4.18	9.16
Ge	-6.35	0.3	1.24	3.83	-1.54	9.42

Table 2.3. Values of $E_{v,av}$ (average of three uppermost valence bands at Ã), spin orbit splittings and deformation potentials of valence and conduction bands for Si and Ge.

2.4 MONTE CARLO SIMULATION OF CARRIER TRANSPORT

The Monte Carlo (MC) method [Pri79] [Jac83] is a widely used stochastic approach for studying charge transport in semiconductors and semiconductor devices. It involves the simulation of the motion of charge carriers subject to a wide variety of scattering mechanisms and external forces. Although it requires appreciable computer resources, the simplicity of implementation and relatively complete description of semi-classical transport make the MC method appealing for semiconductor simulation. It is the most accurate approach to treat transport at high fields. The MC simulation consists of iterations of free flight, scattering-type selection and post-scattering momentum selection for an ensemble of particles. According to the band structure used in the MC simulation of electron transport, there are three types of implementation. The most computationally efficient is a low-energy model using a single parabolic or nonparabolic band [Jac83] that is only applicable to those electrons with energy below 0.5 eV [Wan93]. The second class uses a hybrid model [Wan93] [Bru89] [Vog92] to reduce the computation time. The third class uses a full band structure [Tan83] [Fis88] with as many as four conduction bands. In this dissertation, Slapshot0d, a hybrid model, has been used to study the material transport properties of orthorhombically-strained Si. The features of the hybrid model are described in the next chapter. We also developed a Monte Carlo simulator, MOCA, with two features: full-band version including the treatment of carrier scattering and simulation of strained Si-based multi-material heterostructure devices. In the rest of this section, we will introduce the basic features of full-band Monte Carlo simulator and major development of MOCA in terms of simulation of strained multi-material devices. Fig. 2.5 describes the flow chart of a full-band Monte Carlo simulator, MOCA. The core of the simulator is to simulate a particle ensemble, whose detailed flow chart is shown in Fig. 2.6.

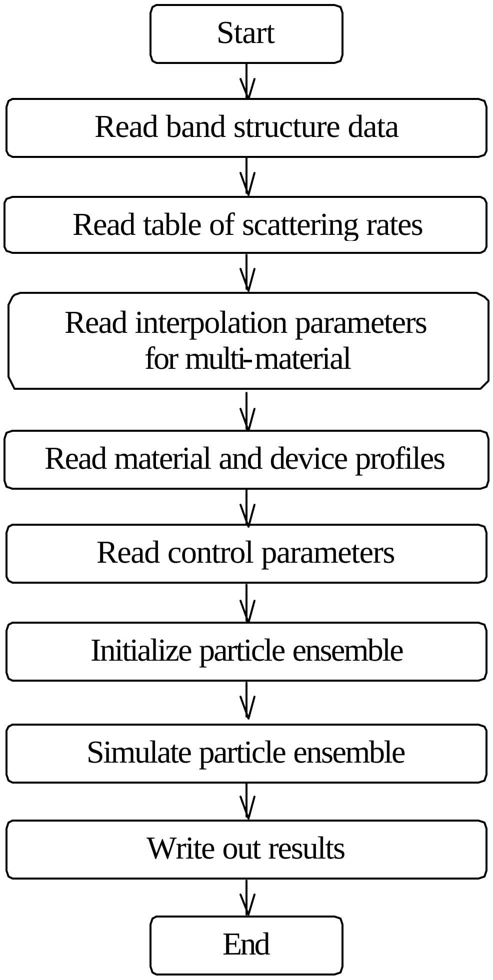

Figure 2.5. Flow chart of full-band Monte Carlo simulation.

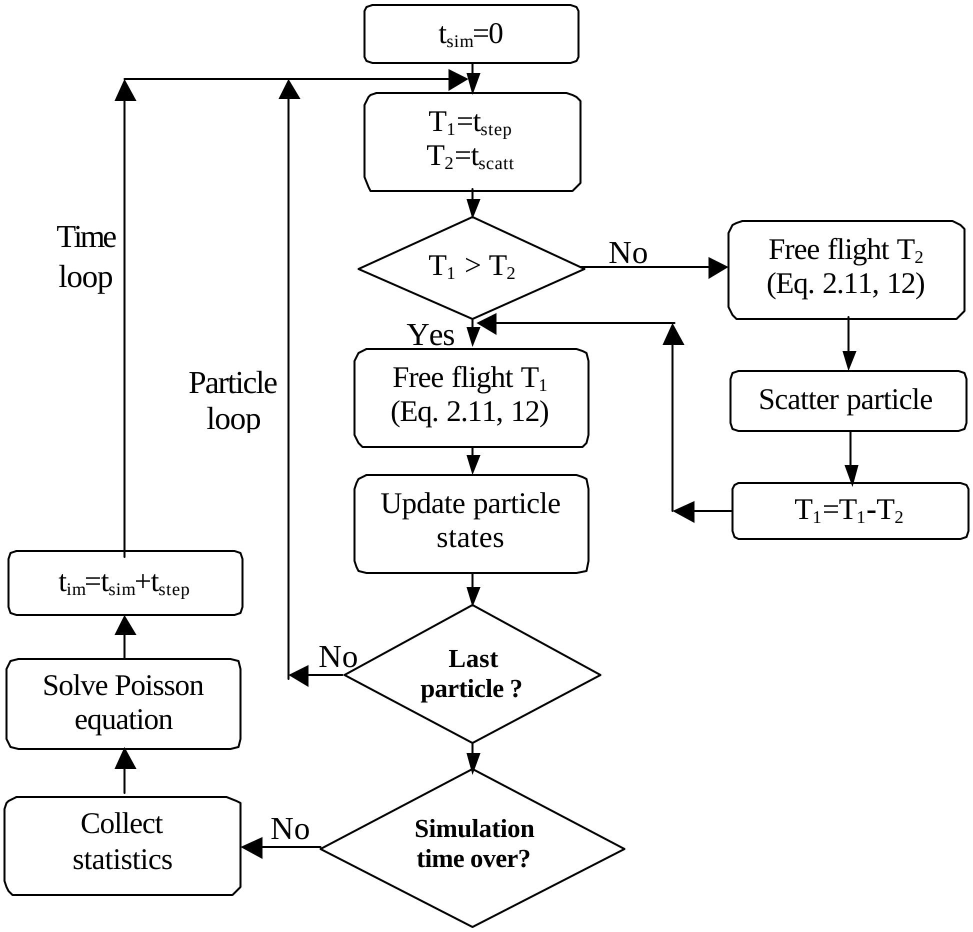

Figure 2.6. Detailed flow chart for particle ensemble simulation.

2.4.1 Transport of carriers

The transport of carriers (electrons and holes) in real and momentum spaces is described in the semi-classical ways:

$$\frac{dr}{dt} = \frac{1}{\hbar}\nabla_k E_m(\vec{k}) \tag{2.11}$$

and

$$\frac{d\vec{k}}{dt} = \frac{q}{\hbar}\left(F_{ext}(\vec{r},t) + \tfrac{d}{dm}\left(E_m(k) + V_{edge}(m)\right)\cdot \tfrac{dm}{dr}\right), \qquad (2,12)$$

where $E_n(k)$ is the energy of carrier with momentum k and strain index m, and F is electrostatic field at time t and carrier's position r. The $E_m(k)$ comes from the band structure of material. F_{ext} is the summation of external field and Columbic potentials of other carriers in self-consistent simulations, obtained by solving Poisson's equation with proper boundary conditions, ionized dopant concentration and carrier density. In MOCA, the Poisson equation is solved with a Newton method, using the Conjugate-Gradient technique and a line search to determine the Newton descent direction and step size.

2.4.2 Carrier Scattering

The free and continuous transport of the carriers in momentum space may be interrupted by interactions between carrier and imperfect ions of periodic potential of the lattice caused by lattice vibrations, impurity, surface roughness and other mechanisms. After the interruption, the momentum of the carriers may suddenly change to other values. This process is called scattering. It degrades the velocity and energy (in inelastic scattering) of the carrier. After the scattering, the carrier starts its next transport process. We consider phonon scattering, impurity scattering, impact ionization, surface roughness scattering and alloy scattering (for alloys) in the simulation. As a first-order perturbation, Fermi's golden rule gives the scattering rate of an interaction.

The scattering rate *P(k)* for an election of momentum *k* interacted with phonon, acoustic and optical, are considered in a conventional way:

$$P_{h,v}(k) = \sum_{o'} \frac{1}{(2p)^3} \int_{BZ} \frac{p}{rw_h(q)} \Delta^2_{n,n'}(q)\left|g(q)\right|^2 d\left[E_{n'}(k') - E_n(k) \pm \hbar w_h(q)\right]\left(N_q + \tfrac{1}{2} \pm \tfrac{1}{2}\right), \tag{2.13}$$

where í and í' are the band indices of initial and final electron, ç is the phonon mode including acoustic and optical, longitudinal and transverse. $Ä_{í,í'}(q)$ is a coupling constant. $\hbar w_h(q)$ and N_q are phonon energy and number, respectively. The upper and lower signs represent phonon emission and absorption. $g(q)$ is the overlap integral:

$$g(q) = \frac{3}{(qR_{WS})^3}\left[\sin(qR_{WS}) - qR_{WS}\cos(qR_{WS})\right]. \tag{2.14}$$

R_{WS} is the radius of the spherical Wigner-Seitz cell [Zim60] and $V_{RC} = \frac{4}{3} p R_{WS}{}^3$, where V_{RC} is the volume of unit cell. Fig. 2.7 shows the overlap integral for Si.

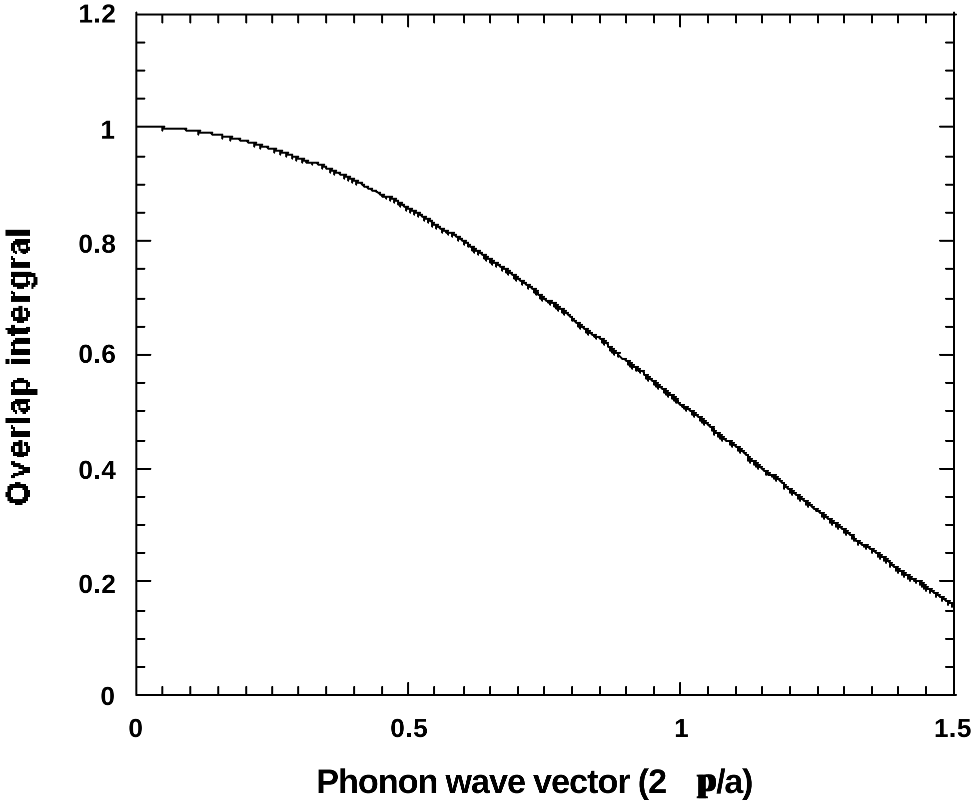

Figure 2.7. Overlap intergral $g(q)$ as a function of phonon wave vector q. The silicon lattice constant a is 5.431 A.

Acoustic phonon dispersion $\hbar\omega_h(q)$ is approximated isotropically [Fis88]:

$$\hbar\omega_h(q) = \begin{cases} \hbar\omega_{h,\max}\left[1-\cos\frac{qa}{4}\right]^{\frac{1}{2}} & q \le \frac{2\pi}{a} \\ \hbar\omega_{h,\max} & q > \frac{2\pi}{a} \end{cases} \tag{2.15}$$

The maximum frequency $\omega_{h,\max}$ is related with sound velocity u by $\frac{4u}{a}$ and a is the lattice constant. The optical phonon energy is modeled with a constant $\hbar\omega_{op}$. The sound velocities and optical phonon energies of Si and Ge are provided in Table IV in [Can75]. In principle, $\Delta_{n,n'}(q)$, originated from matrix element term in Fermi golden rule, can be calculated from the pseudopotential theory at the long-wavelength approximation. Here we assume the acoustic phonon coupling constants to be linearly dependent on phonon momentum q, $\Delta_{n,n'}(q) = q\Delta_n$ for longitudinal-acoustic (LA) and transverse-acoustic (TA), and the optical phonon coupling constant ΔK_{op} is independent of phonon momentum. These constants are adjusted to fit the experimental velocity-field characteristics. The fitting results are shown in the following chapters. Thus

$$P_{\eta,\nu}(k) = \sum_{\nu'} \tfrac{1}{(2\pi)^3} \int_{BZ} \tfrac{\pi}{\rho} \Delta^2 \delta\left[E_{n'}(k') - E_n(k) \pm \hbar\omega_\eta(q)\right] f(q)\,, \tag{2.16}$$

and

$$f(q) = \begin{cases} \dfrac{q^2}{\omega_{ac}(q)} \left|g(q)\right|^2 \left(N_q + \tfrac{1}{2} \pm \tfrac{1}{2}\right) & accoustic\ phonon \\ \dfrac{1}{\omega_{op}} \left|g(q)\right|^2 \left(N_q + \tfrac{1}{2} \pm \tfrac{1}{2}\right) & optical\ phonon \end{cases}. \tag{2.17}$$

In order to facilitate the treatment of energy and momentum reservations in choosing the k', rejection and self-scattering techniques are employed. First the q-dependent factor $f(q)$ is calculated and stored in a look-up table before simulation. Then a maximum scattering rate is applied to a carrier with energy E_0 using the maximum of $f(q)$, $f_{\max}$. Also the energy of the carrier after scattering E' is chosen randomly and uniformly between E_0 and $E_0 \pm \hbar\omega_{\eta,\max}$, and correspondingly the momentum k'. The relative phonon momentum is $q = k' \mp k$, and the phonon energy $\hbar\omega_\eta(q)$ is obtained from Eq. 2.14. Next the energy conservation is checked within a pre-determined small energy width $\Delta\varepsilon$: $\left|E'(k') \mp \left(E_0(k) \pm \hbar\omega_\eta(q)\right)\right| \le \Delta\varepsilon$, another test E' is chosen until the conservation law is satisfied. Finally, the final state is kept if $f(q)/f_{\max}$ is bigger than a random number, and the energy uncertainty, $E'(k') \mp \left(E_0(k) \pm \hbar\omega_h(q)\right)$ is compensated for in next scattering. The carriers with reject acceptable final states are treated by self-scattering. This scheme can properly and easily treat energy and momentum conservation in phonon scattering.

Generally the electron-ionized impurity scattering can be implemented by Brooks-Herring (BH) formula [Bro51] or Conwell-Weisskopff (CW) formula [Con50]. Two-body BH model uses the electron screening effect to limit the influence of other impurity center, while in CW model the range of Coulombic potential of one impurity is cut off to half the inter-impurity spacing to justify the one-center scattering assumption. On the whole, the BH model is preferred to CW model. But CW model is better than BH in treating high doping and low temperature situations attributed to the inaccurate treatment of screening effect of BH model in these cases. Ridley [Rid77] took the effect of second scattering center into account and generated a treatment connecting the BH and CW models. In this work Ridley's formula is implemented.

At high electric field electrons may gain sufficient energy from external field to excite a hole in a valence band to conduction band. This scattering mechanism is called impact ionization (I.I.). The energy required for impact ionization is known as threshold energy. It is determined by both energy and momentum conservations.

In electron simulation, we employed Cartier's [Car93] multi-threshold energy formula:

$$\frac{1}{\tau_{ii}(E)} = \sum_{i=1}^{3} \theta\left(E - E_{th}^{(i)}\right) P^{(i)} \left(\frac{E - E_{th}^{(i)}}{E_{th}^{(i)}}\right)^2, \qquad (2.18)$$

where E is the electron energy, è is a step function, threshold energy $E_{th}^{(i)} = 1.2$, 1.8 and 3.45 eV, $P^{(i)} = 6.25\times10^{10}$, 3.0×10^{12} and 6.8×10^{14} S^{-1}, for i=1, 2 and 3, respectively. These three threshold energies are consistent with the indirect gap E_{gap}, $3E_{gap}/2$ and direct gap of Si. The formula better accounts for the complexity of silicon band structure in a simple empirical formula.

In hole simulation, we used Kunikiyo's [Kun96] fitted soft-threshold formula:

$$\frac{1}{\boldsymbol{t}_{ii}(E)} = 1.14\times(E-1.49)^{3.4}. \tag{2.19}$$

This formula fits the Kunikiyo's direct calculation of impact ionization rate based on realistic Si band structure.

Carrier mobility in devices is degraded in inversion layer of MOSFETs due to the strong gate field. The vertical field caused by gate and roughness of Si and SiO_2 interface make the carrier transport in device simulation different from bulk case. So a surface roughness scattering is introduced in the interface region. The surface roughness can be characterized by correlation length L and rms height of the amplitude of the roughness ΔZ. In this work, Yamakawa's [Yam96] exponential autocovariance function and formulas are used to consider electron surface roughness scattering. In case of hole, the roughness scattering rate is described as a semi-empirical formula [Jal96]:

$$S_{SR}(E) = C_{SR}D(E)L^2\Delta Z^2 {E_{eff}}^{a} e^{-2m^* E L^2 \Delta Z^2/(q\hbar^2)}, \tag{2.20}$$

where E is the carrier energy, $D(E)$ is the density of states, E_{eff} is hole concentration weighted vertical fields and m^* is density of states effective mass. C_{SR} and a are two fitting parameters to match experimental mobility.

In SiGe alloys, an additional carrier scattering, alloy scattering, occurs due to a disorder potential arising from the random distribution (or virtual crystal approximation) of the constituent atoms (Si and Ge) among the various sites of the lattices. In a widely-used inner potential model [Har76] (i.e., scattering from hard spheres of suitable radius, R_a and depth ΔU), the scattering kernel associated with this process takes the form [Fis96]

$$\begin{aligned} S(k'\beta;k\alpha) = \frac{2\pi}{\hbar}\Omega_c x(1-x)\left|G(q)\right|^2 \Delta U^2 \left|I(k'\beta;k\alpha)\right|^2 \\ \times\delta\left[E^a(k) - E^b(k')\right] \end{aligned}, \tag{2.21}$$

where k and k' are initial and final momentum of carrier in the scattering, $q = k' - k$ is the momentum transfer, Ω_c is the volume of the unit cell, and ΔU is the effective depth of the scattering well whose radius can be taken to be equal to the radius of a sphere with volume equal to the unit cell (i.e., $R_a = a_0[3/(16\pi)]^{1/3}$) or be the nearest-neighbor distance $\sqrt{3}a_0/4$, $I(k'\beta;k\alpha)$ is the overlap integral between Bloch waves of k' and k in bands β and α, approximately taken to be unity, and $G(q)$ is the form factor of the hard sphere,

$$G(q) = 3\frac{\sin(qR_a) - (qR_a)\cos(qR_a)}{(qR_a)^3}, \tag{2.22}$$

The strong dependence of Eq. (2.22) on q (as $(qR_a)^{-4}$ at large q), will effectively suppress the possibility of *f*-type intervalley scattering.

In treatment of the alloy scattering, a main uncertainty is the value of potential well ΔU. Fischetti and Laux [Fis96] employ 0.7 eV for electron and 0.9 eV for hole in their simulation of strained SiGe, based on fitting the Bush and Vogt's [Bus60] experimental mobility data of relaxed SiGe. Gicksman [Gli58] and Manku [Man92] have reported smaller value (0.46 eV) for electron, while Li *et. al*. [Bus60] obtained a much smaller value (0.2 eV). Large ΔU causes alloy scattering to dominate the carrier scattering and degrades (even dissipated) the advantage of strained SiGe gained from split valleys and lower effective masses.

2.4.3 Strained multi-material devices related development

In multi-material heterostructure device simulation, every node in real-space mesh is labeled with a material type and degree of stress. Correspondingly the band structures of all kinds of materials used in the device with various strains should be stored in memory. This requires enormous memory. In this work, we developed an interpolation technique with tables of fitted functions to simplify the storage of band structures of various strained material. Before runtime, a set of band structures of material with discrete strain was calculated and fitted with polynomial for every point in momentum space. We found a quadratic fit function can accurately describe the change of energy and velocity with strain fore very momentum point. Thus in runtime, only band structure of relaxed Si is stored as a look-up table along with related momentum-dependent fit the coefficients. In the MOCA simulation code, two kinds of band structures are needed and used differently. The band structure for carrier transport is a $40\times40\times40$ grid in momentum space and used to directly find energy for a given momentum. In order to find the energy in a strained material with strain index m, the energy in relaxed Si is found and the corresponding fitting coefficients and strain index m are used to get energy in strained material. The other $100\times100\times100$ grid of band structure is used indirectly to find momentum states for a given energy after scattering. In this band structure, the momentum is ordered from low energy to high values. Thus in runtime, final momentum with a given energy after scattering can be efficiently found with a twin binary search. The method accounts for the density of states. In the multi-material case, the search for momentum states for a given energy is complicated. First, momentum state for a given energy is found based on relaxed Si band structure. The momentum state serves as an initial guess and starting point. Then the momentum states around that guess point with a predetermined range is randomly checked to see whether the energy calculated from fitting coefficients and energy of relaxed Si matches the final energy. Fig. 2.8 shows the flow chart of direct and indirect use of band structure in strained material.

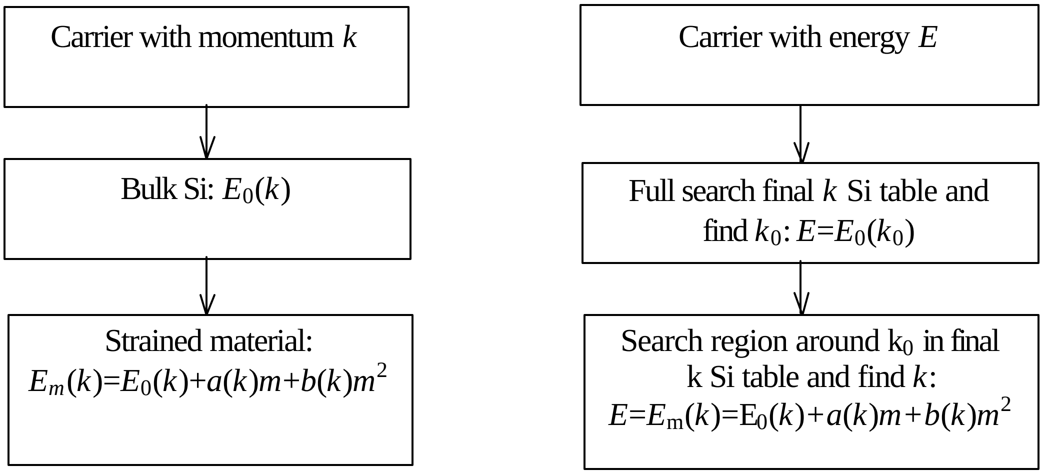

Direct Interpolation

Indirect Interpolation

Figure 2.8. Procedure for Monte Carlo band structure interpolation for strained material with index m.

The scattering rates are usually momentum dependent. For computational and coding efficiency, the scattering rates are considered energy dependent by using averaged rates. It is a good approximation for relaxed Si due to the symmetry and can dramatically decrease the memory and coding requirement without sacrificing accuracy. In strained material, the symmetry is broken by strain. It may cause more anisotropic scattering. i.e. momentum states with the same energy may have big difference in scattering rates. Thus the energy-dependent scattering table may be questionable. Fig. 2.8 shows the momentum-dependent scattering rates for bulk Si and strained Si grown on relaxed $Si_{0.7}Ge_{0.3}$. In high energy region, Fig. 2.9(a), the scattering rate is almost isotropic for both Si and strained Si. In low energy region, Fig. 2.9(b), the anisotropic behavior appears in strained Si. But the relative difference is still small compared with the scattering rate. That means the averaged energy-dependent scattering rate is still a good approximation for strained material.

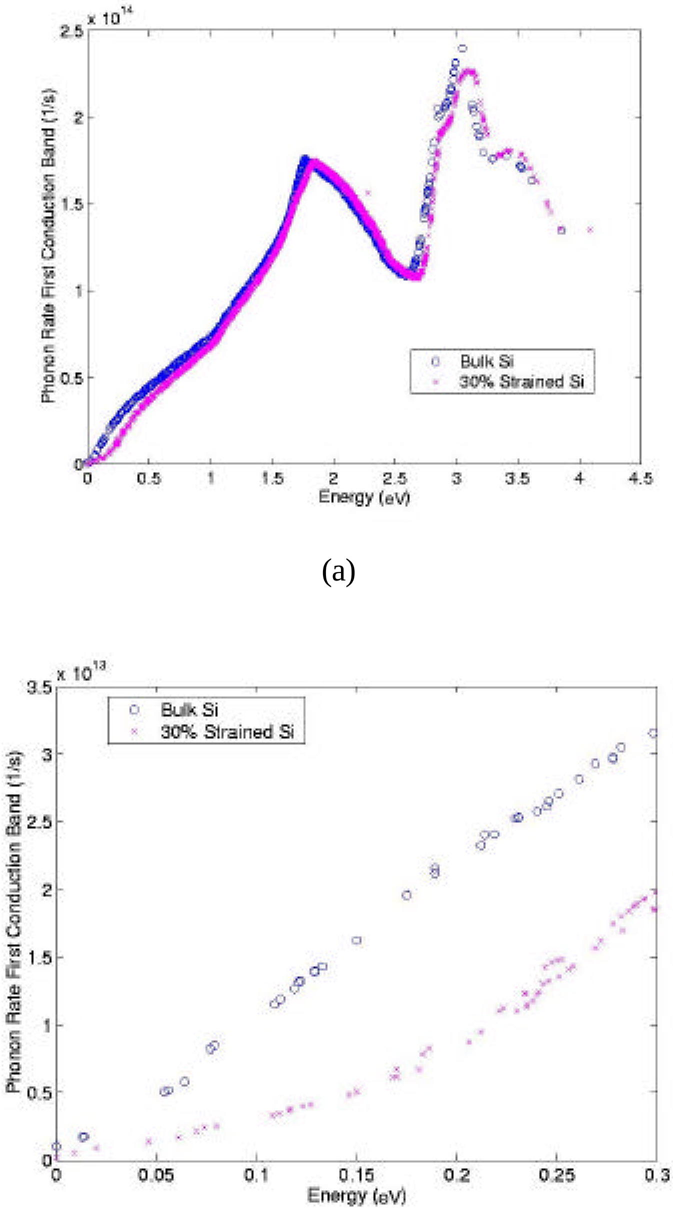

(a)

(b)

Figure 2.9. Phonon scattering rates of first conduction band for unstrained Si and strained Si grown on relaxed Si$_{0.7}$Ge$_{0.3}$. The momentum-dependent rates are directly plotted on the energy scale without smoothing. (a): The scattering rates in high energy region and (b): in low energy region.

As mentioned in Sec. 2.3, there are abrupt potential changes, steps or barriers, caused by different materials in multi-material devices. The carriers may tunnel through the potential barriers. Ideally, transfer-matrix method [Tsu73] can describe the tunneling accurately. But in Monte Carlo simulation, it is too time-consuming. We use Feynamn's [Fey65] effective potential, V_{eff}, to simply and reasonably treat the quantum effect (see Fig. 2.10). Because the wave characteristics of carriers in quantum mechanics, a carrier feels not only local potential but the potential in the range of wave function. Thus V_{eff} should include the effect of potentials surrounding the carrier:

$$\begin{aligned} V_{eff}(x) &= \frac{1}{\sqrt{2pa}} \int_{-\infty}^{\infty} V(x_0) e^{-\frac{(x_0-x)^2}{2a^2}} dx_0 \\ a &= \frac{\hbar^2}{12m^* k_B T} \end{aligned} \quad . \tag{2.23}$$

Eq. (2.23) shows that the potential actually seen by a carrier at position x is a smearing of the non-local potentials in a small range a. In the simulation, we treat a as a fitting parameter by fitting the tunneling current from effective potential method to transfer-matrix results in a simple but typical step-function like potential (Fig. 2.11(a)) with various potential barriers and temperatures. Fig. 2.11(b) shows good agreement of the calculated tunneling current with $a = 14$ Å at room temperature with the two methods.

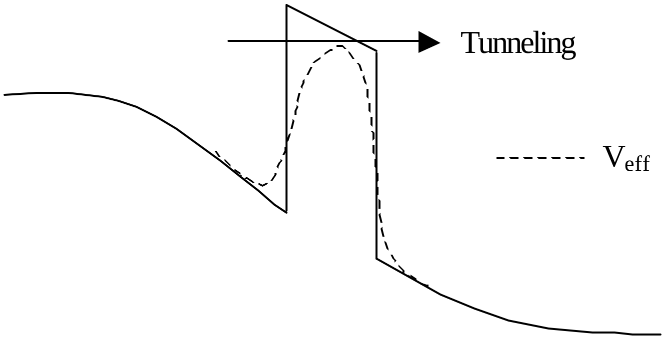

Figure 2.10. Schematic of potential barrier and "effective Feynman potential" after considering quantum effect.

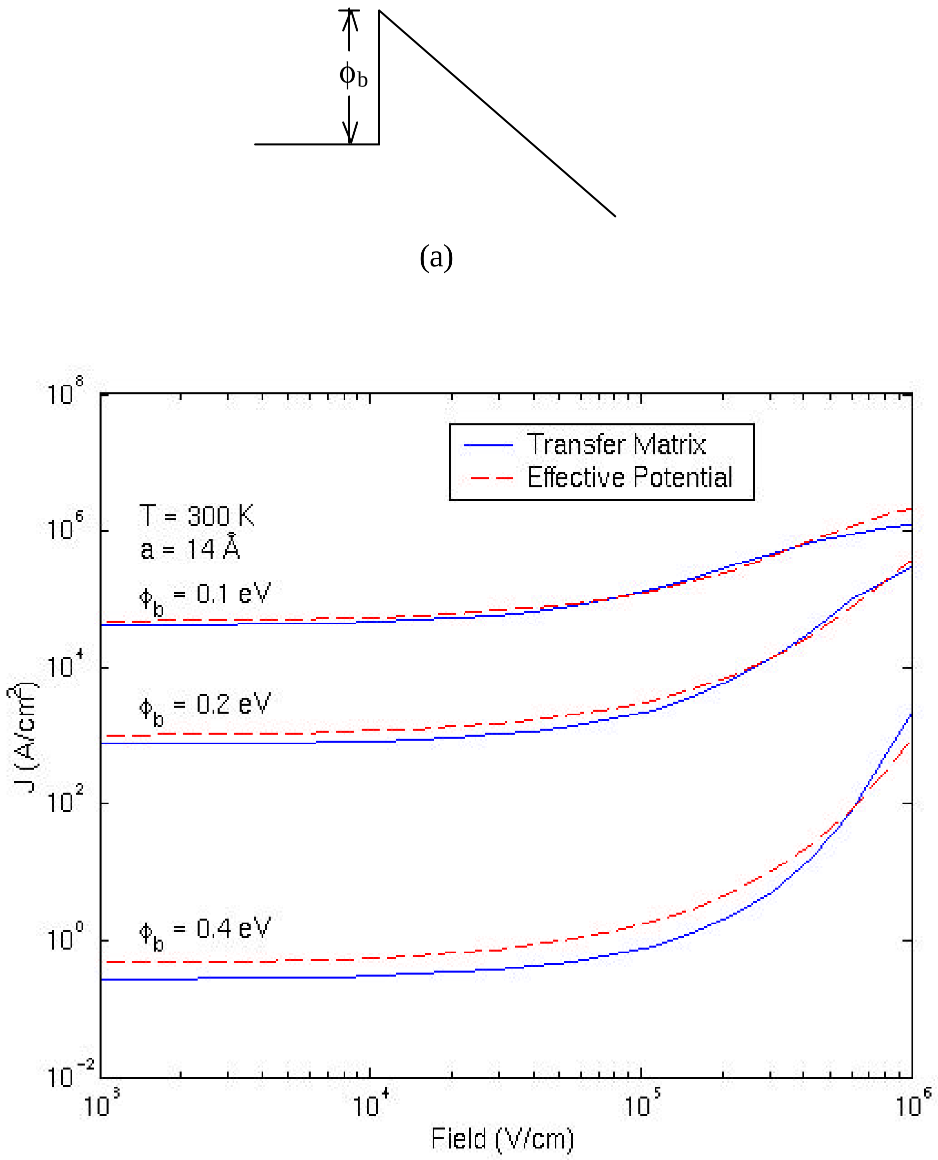

(a)

(b)

Figure 2.11. (a) Schematic of the trianglular potential barrier. (b) Comparison of tunneling current through the triangular barriers with various barrier heights between transfer-matrix method and effective potential.

CHAPTER THREE

Orthorhombic Silicon

3.1 MOTIVATION

The development of vertical MOSFET's has led to the growth of simple orthorhombically-strained silicon by Liu *et. al.* [Liu99] who fabricated a vertical n-MOSFET with a strained sidewall silicon channel (Fig. 3.1). In this device a thin SiGe layer is pseudomorphically grown on a Si substrate and then a Si cap layer is grown on the sidewall of the SiGe pillar as a channel. Finally a source and drain are formed by ion implantation. The Si cap that forms the channel comprises an unusually configured material. With Si grown as a sidewall on the edge of a compressively-strained SiGe (CS-SiGe) layer, it is surmised that this Si material becomes deformed into a simple orthorhombic lattice. In this case, all three dimensions of the unit cell are different from each other in length since the base on which the material grows is a rectangle with one side that conforms to the Si lattice constant and one side that is elongated according to the Poisson ratio to accommodate the SiGe alloy pseudomorphically (Fig. 3.2). The third dimension is determined as the material grows, and like biaxially tensily-strained, tetragonal Si, the Si sidewall should have a lattice constant in the growth direction that is less than the lattice constant of cubic Si. However, unlike the tensily-strained Si (TS-Si), all three $\langle 100 \rangle$ dimensions of the orthorhombically-strained Si (OS-Si) unit cell have different lengths. The rest of this chapter describes the properties of this novel material including lattice structure, band structure and carrier transport.

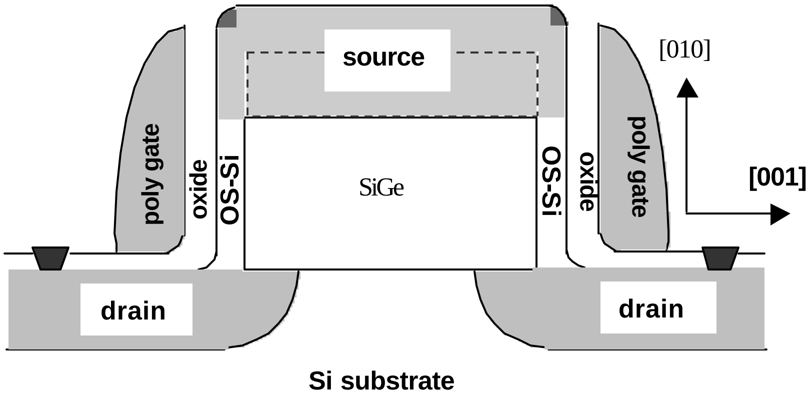

Figure 3.1. Schematic cross section of a vertical silicon n-MOSFET.

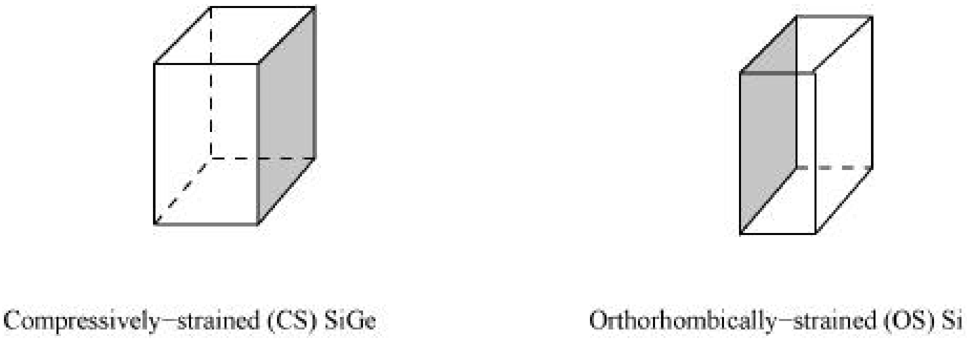
Compressively−strained (CS) SiGe

Orthorhombically−strained (OS) Si

Figure 3.2. Unit cells of compressively-strained SiGe and orthorhombically-strained Si.

3.2 LATTICE STRUCTURE, BAND OFFSETS AND BAND GAP

In the OS Si, three directions have three different lattice constants caused by the confinement of its substrate, strained SiGe. The lattice structure is calculated by elastic theory (Sec. 2.1). Fig. 3.3 shows the changes of lattice constants of OS Si with Ge mole fraction x. Under the constraint of the bulk Si substrate, the [100] lattice constant of the $Si_{1-x}Ge_x$ pillar and, thus the OS-Si layer remains that of bulk Si, while in the [010] direction the lattice of OS-Si is enlarged to conform the extended side of the compressively strained $Si_{1-x}Ge_x$ pillar. The lattice spacing in [001] is compressed to minimize the elastic energy coming from the tensile [010] strain.

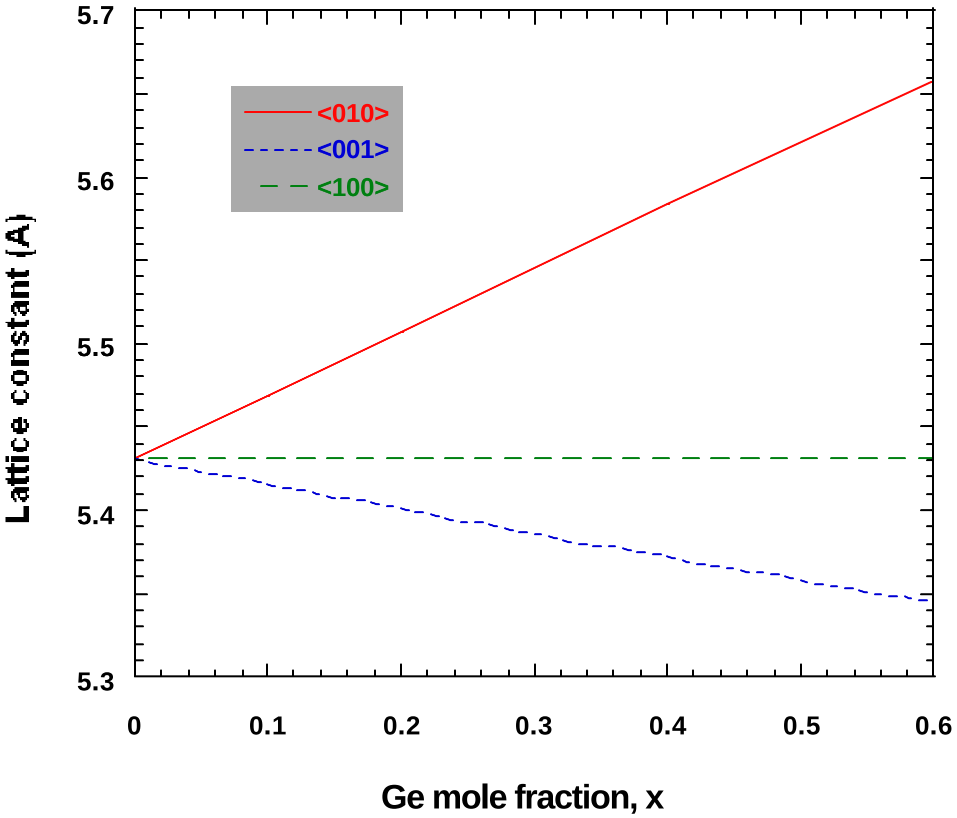

Figure 3.3. Lattice constants of OS-Si for various mole fraction x of Ge in the $Si_{1-x}Ge_x$ layers.

Fig. 3.4(a) shows the band offsets, valence and conduction bands, between the orthorhombic-strained Si and the sidewall of a $Si_{1-x}Ge_x$ layer, calculated from model-solid theory (Sec. 2.3.2). We note that the band edge shift and splitting of

OS-Si are similar to those of TS Si, and the compressive strain in the strained SiGe layer moves the conduction band down and pull the valence band up. Thus, compared to the band offsets between TS-Si and R-SiGe alloy, the OS-Si/CS-SiGe interface has lower conduction-band offset and higher valence-band offset. After using the band gap result from experiment, the band gap of OS-Si is presented in Fig. 3.4(b). In OS-Si, only one dimension is expended on the interface, while both dimensions are extended on that plane in TS-Si. So less strain is induced in OS Si than TS-Si, and the band gap of OS-Si is larger. The band gap of OS-Si can be expressed by

$$E_g(x) = 1.11 - 0.86x \, , \tag{3.1}$$

which is used in impact ionization process of a MC simulation of OS-Si.

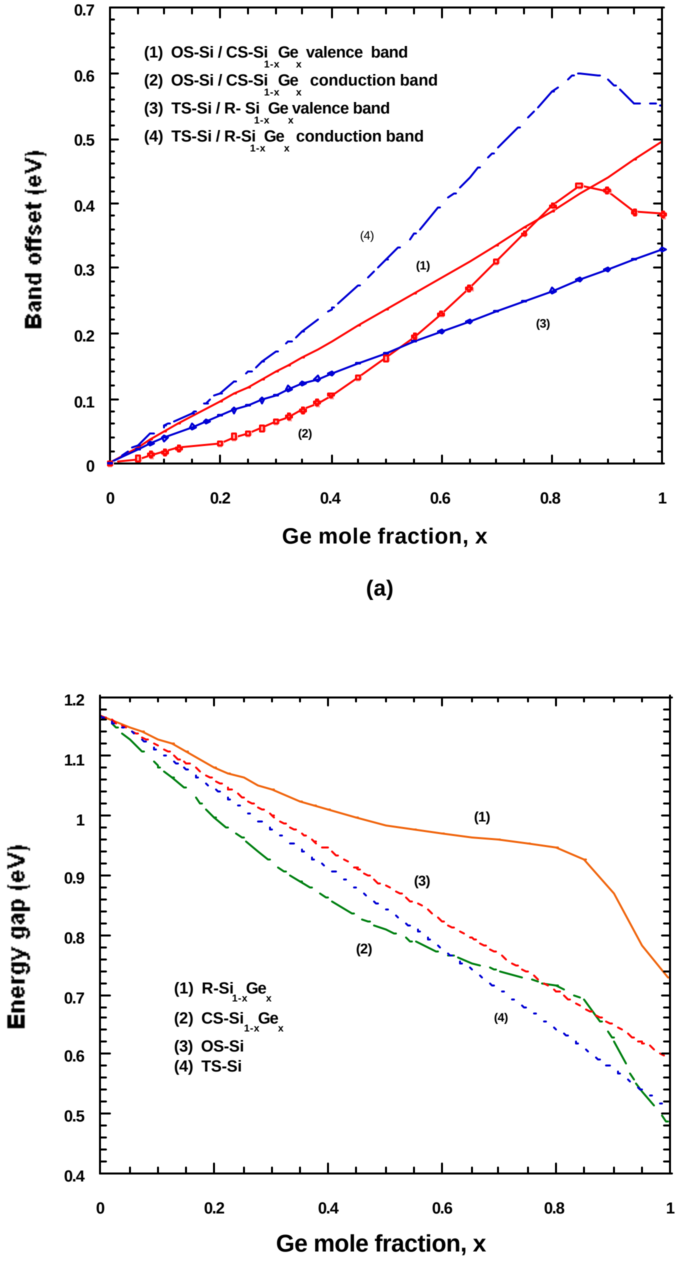

(a)

(b)

Figure 3.4. (a) Band offsets of OS-Si/CS-Si$_{1-x}$Ge$_x$ and TS-Si/R-Si$_{1-x}$Ge$_x$ heterojunctons; (b) Band gaps of OS-Si, CS-Si$_{1-x}$Ge$_x$, TS-Si and R-Si$_{1-x}$Ge$_x$

3.3 BAND STRUCTURE OF OS-SI

The band structure of this novel material is studied by DFT (Sec. 2.2.1) due to its high flexibility. The six lowest Ä valleys of the first conduction band are crucial to the electron transport properties of silicon under low and intermediate external electric fields. The hydrostatic and uniaxial strain of OS-Si breaks the six-fold degenerate valleys into three pairs shown in Fig. 3.5. Two-fold degenerate tensily-strained [010] valleys move up; compressively-strained [001] valleys move down; and the third pair, for which the [100] lattice constant is the same as that of bulk Si, only experiences hydrostatic strain and moves up a little because of a positive hydrostatic deformation potential [Van89] for Si. The valley splittings are shown in Fig. 3.6, where $dE_1 = E_{[100]} - E_{[001]}$ and $dE_2 = E_{[010]} - E_{[001]}$, and E refers to the lowest energy of the Ä valley. Fig. 3.7 shows the DOS of OS-Si, calculated from the full band structure. We see the valley splitting broadens and lowers the DOS peaks, but the band structure remains predominantly Si-like. As can be seen from the Fermi golden rule, the electron scattering rate is a function of the DOS. Thus the DOS change in OS-Si will affect the electron transport properties.

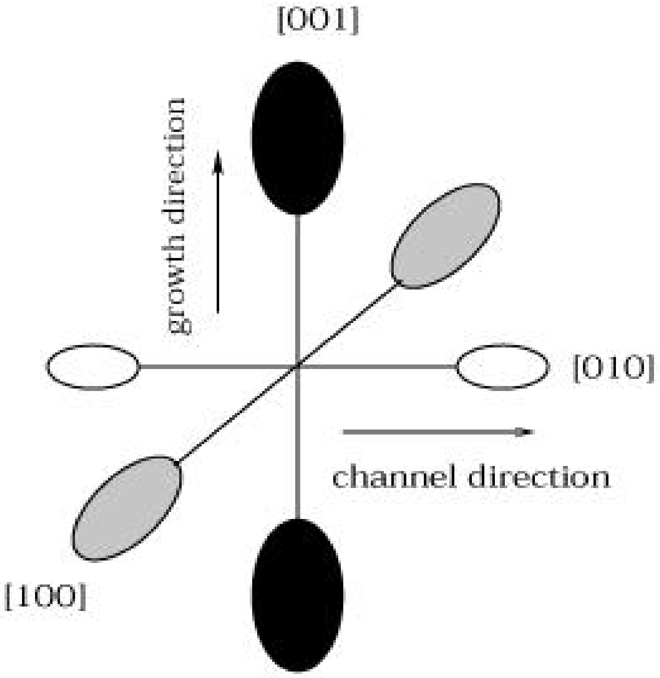

Figure 3.5. Schematic equi-energy surfaces of the six split valleys in the first conduction band of OS-Si. The minimum energies of the dark valleys are lowest, the gray ones have intermediate minimum energies and the minima of the open ellipsoids are the highest.

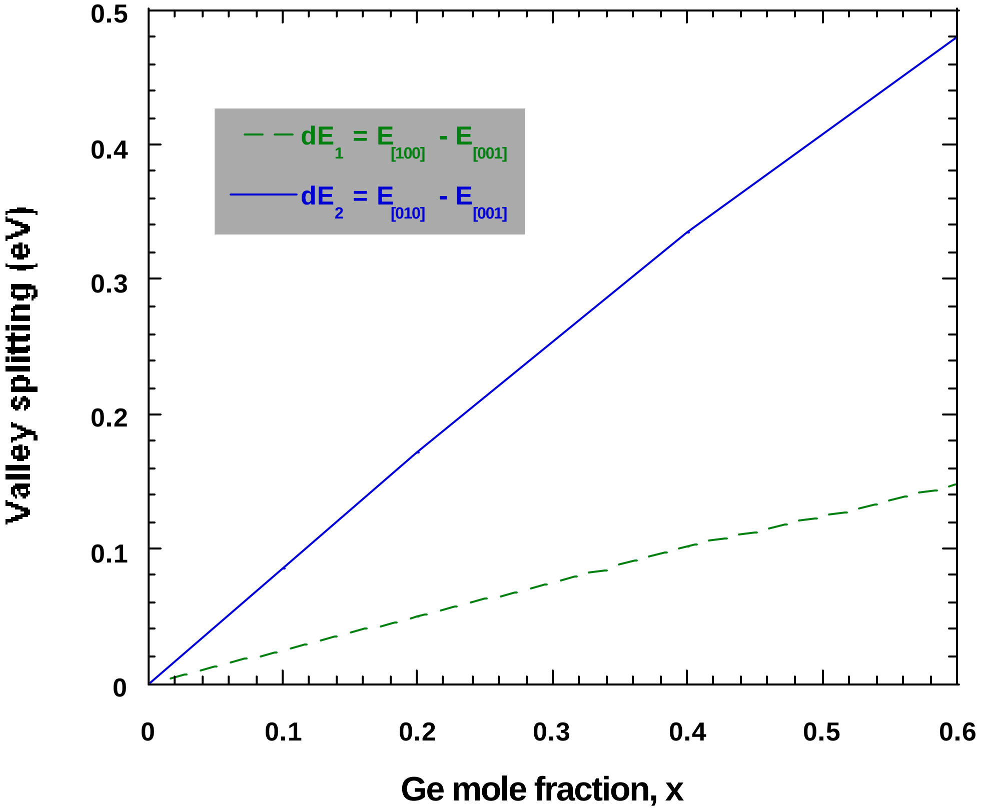

Figure 3.6. Ä valley splitting in a sidewall OS-Si as a function of Ge mole fraction. We set minimum of $\Delta_{[001]}$ as the energy reference.

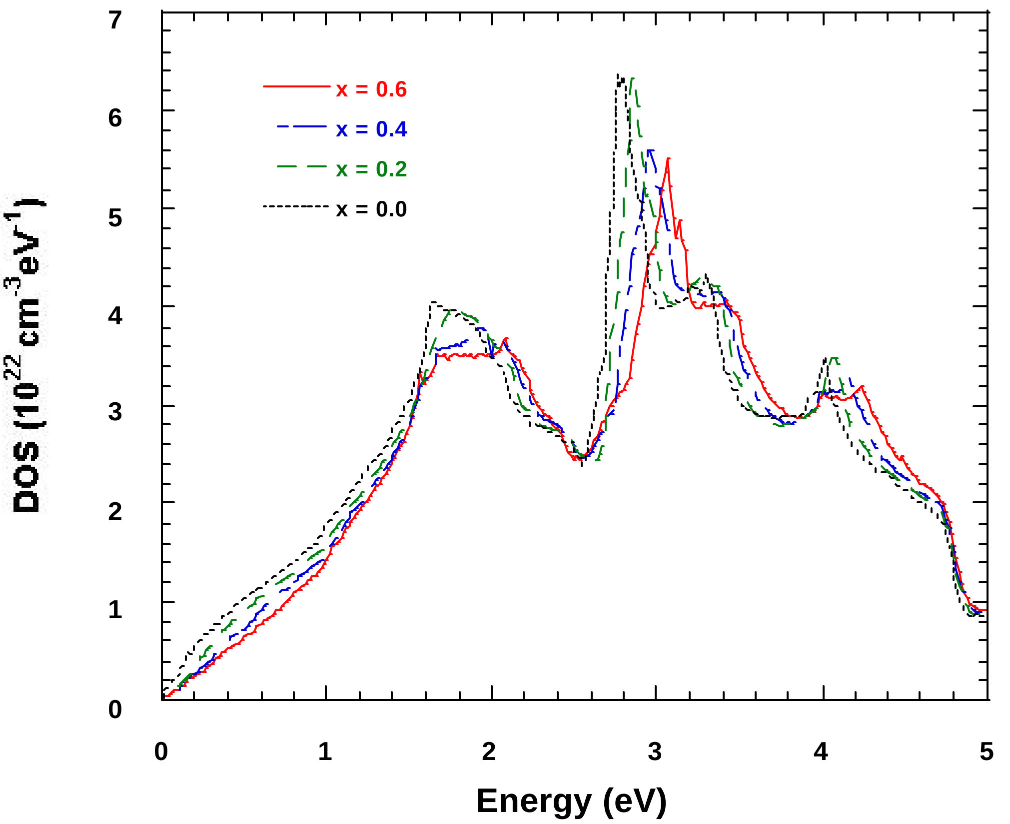

Figure 3.7. Conduction band density of states of bulk Si and OS-Si grown on $Si_{1-x}Ge_x$ sidewalls.

3.4 TRANSPORT SIMULATION RESULTS

3.4.1 Calibration of electron transport in unstrained Si

We adopt a hybrid MC code, slapshot0d [Wan93] developed by Wang *et al.* to study the electron transport properties. It uses a full band structure in generating scattering rates and a set of well-fitted anisotropic, analytical bands [Wan93] for both electron free-flight and post-scattering momentum selection processes. This technique saves time in the post-scattering momentum selection and includes the effects of the full band structure in the scattering rates. If the analytic bands fit the dispersion relation ($E(k)$) well, this model can give a result essentially as accurate as pure full-band models in much less time.

In order to accurately describe both electron free flight, depend on the E(k) relation, and postscattering momentum selection, related to density of states (DOS) and the E(k) relation, both the DOS and E(k) relations in principle crystal directions are fitted by a set of nonparabolic bands

$$E(k)(1+aE(k))=\frac{\hbar^2}{2p}\sum_{i=1}^{3}\frac{k_i^2}{m_i}\ , \tag{3.2}$$

where E and k are the electron energy and the wave vector measured from valley minimum, á is the nonparabolicity and m_i is the electron effective mass in principle direction i. We use a nonlinear, least-squares algorithm (Levenberg-Marquardt) to obtain the optimized á and m_i of every valley. Also these parameters are adjusted to fit the DOS obtained from full band shown in Fig. 3.8. The fitting parameters in Eq. (3.1) of Ä valleys are listed in Table 3.1.

We calibrate the electron transport properties of unstrained Si with low doping concentration, 10^{15} cm^{-3} at 300K. After matching velocity (Fig. 3.9(a)) with experimental [Can75] [Jac77] and simulation [Fis88] results at both low ($\leq 10^4$ V/cm) and high field ($\geq 10^5$ cm), a set of coupling constants is found:

$$\Delta_{LA} = \Delta_{TA} = \begin{cases} 1.3eV & (1st\ band) \\ 0.9eV & (2nd\ band) \\ 0.7eV & (3rd\ band) \end{cases} , \tag{3.3a}$$

$$\Delta K_{op} = \begin{cases} 4.2 \times 10^8\ eVcm^{-1} & (1st\ band) \\ 3.7 \times 10^8\ eVcm^{-1} & (2nd\ band) \\ 3.5 \times 10^8\ eVcm^{-1} & (3rd\ band) \end{cases} \tag{3.3b}$$

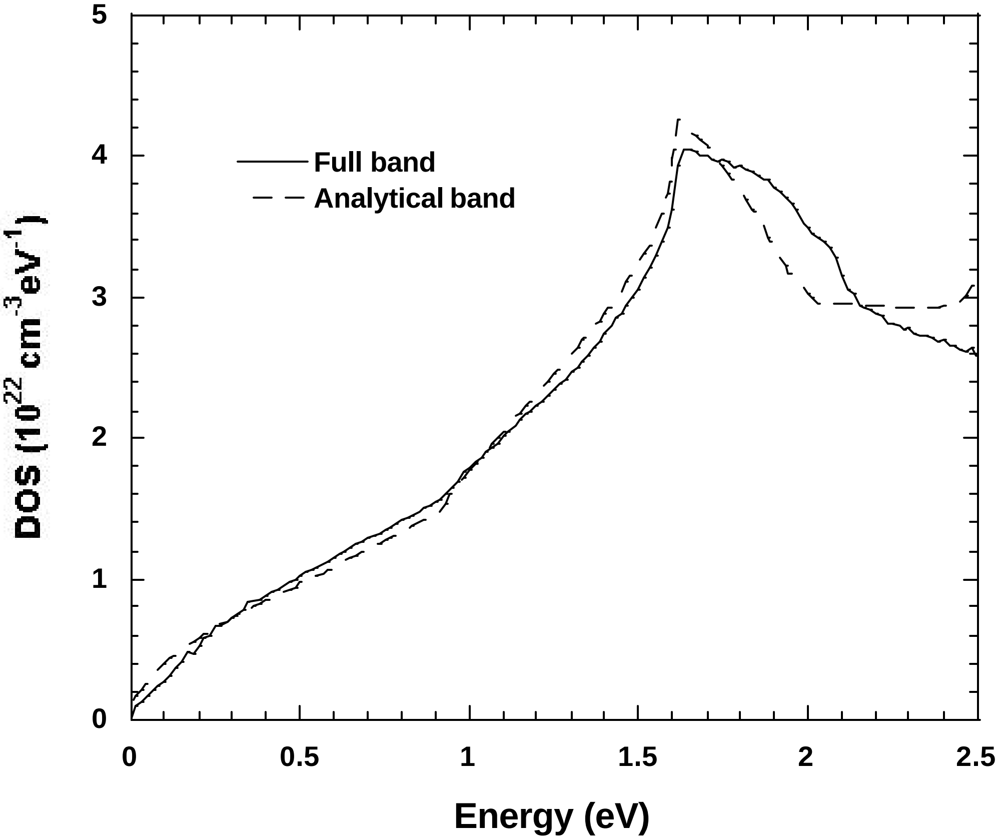

Figure 3.8. Fitted density-of-states based analytical band. The density-of-states from full band structure is also shown for comparison.

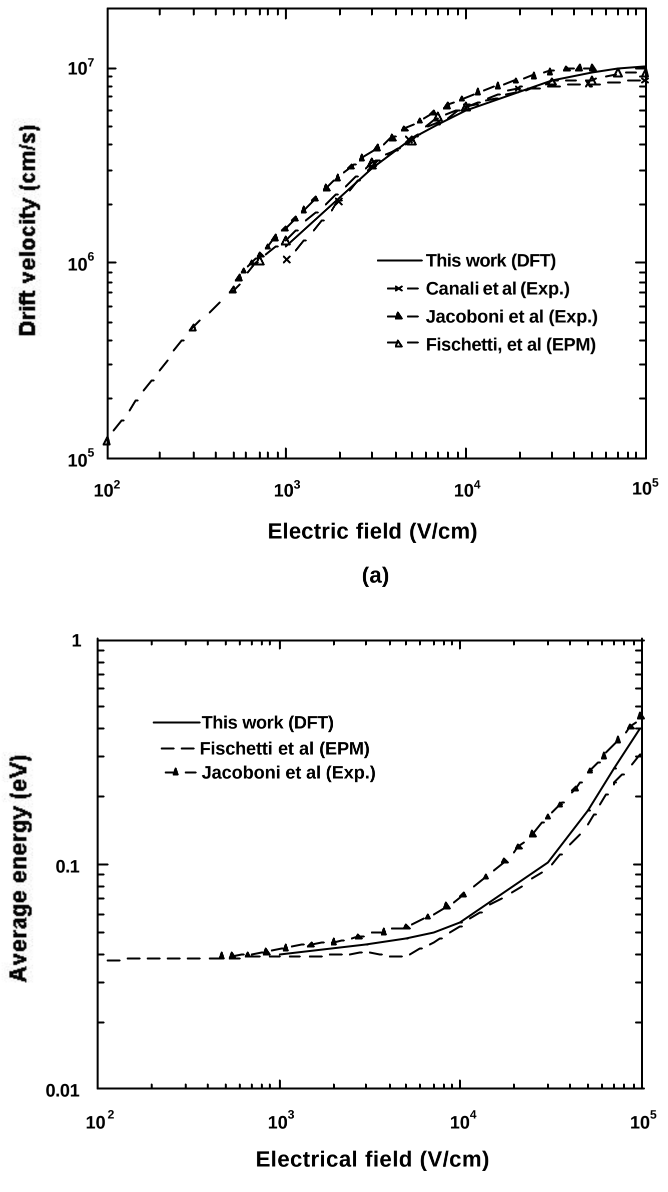

Figure 3.9. (a) Simulated electron drift velocity for unstrained as a function of electric field along (100) direction. (b) Simulated average electron energy for unstrained Si. Results of previous experimental studies and Monte Carlo simulation based on empirical pseudopotential method (EPM) are shown as comparisons.

3.4.2. OS-Si material properties

After taking aforementioned symmetry breakdown into account in a strained layer, we use a bigger irreducible BZ, one sixteenth (tetragonal unit cell) or on eighth (orthorhombic unit cell) of the size of first BZ, rather than the standard 1/48th as in a FCC cell. DFT generates first-three electron bands on a fine even mesh with point of size $\frac{1}{4}\frac{2\pi}{a}$, a is the lattice constant of bulk silicon. The strain-dependent three full bands are used in generating a scattering rate look-up table for choosing scattering type. This is critical to the accurate calculation of electron energy. The effective mass and nonparabolicity in Eq. 3.2 for OS-Si (Table 3.1) are obtained by fitting the full-band density of states in the same as unstrained Si. We note that the longitudinal effective masses m_l of OS-Si are almost the same for various degrees of strain, $m_l = 0.9 m_0$, in which m_0 is the free electron mass. The transverse effective mass m_t is also essentially unchanged at $m_t = 0.3 m_0$. Also the minima are around $0.85\frac{2\pi}{a}$. Only the $\Delta_{[010]}$ valley of OS-Si on $Si_{0.4}Ge_{0.6}$ has a significantly higher longitudinal effective mass, representing more distortion.

	$\Delta_{[100]}$				$\Delta_{[010]}$				$\Delta_{[001]}$			
Ge mole fraction	$k_{\min}$	m_l	m_t	a	$k_{\min}$	m_l	m_t	a	$k_{\min}$	m_l	m_t	a
0.0	0.84, 0, 0	0.94	0.30	0.25	0, 0.84,0	0.94	0.30	0.25	0, 0, 0.84	0.94	0.30	0.25
0.1	0.84, 0, 0	0.94	0.30	0.25	0, 0.84, 0	0.94	0.30	0.25	0, 0, 0.84	0.94	0.30	0.25
0.2	0.85, 0, 0	0.92	0.31	0.25	0, 0.84, 0	0.93	0.31	0.25	0, 0, 0.85	0.90	0.30	0.25
0.4	0.84, 0, 0	0.94	0.30	0.25	0, 0.83, 0	1.00	0.30	0.25	0, 0, 0.85	0.93	0.30	0.25
0.6	0.84, 0, 0	0.89	0.21	0.2	0, 0.84, 0	1.00	0.25	1.10	0, 0, 0.85	0.93	0.25	0.25

Table 3.1. Fitting parameters of Ä valleys in OS-Si. The unit of $k_{\min}$ is $\frac{2p}{a}$, and m_l and m_t are in terms of free electron mass.

Fig. 3.10 shows the electron occupancies in the Ä valleys for OS-Si on CS-Si$_{0.8}$Ge$_{0.2}$ as a function of fields applied along [010] and [100] directions. Due to the valley splitting, at low fields most of electrons occupy the Ä$_{[001]}$ valleys which are lowest in energy. The Ä$_{[100]}$ valleys are less preferred, while the higher Ä$_{[010]}$ valleys are essentially empty. With the increase of field strength, more electrons move up to the high-energy valleys, Ä$_{[100]}$ and Ä$_{[010]}$, until they are almost evenly distributed among the Ä valleys at very high fields. We note that at high fields, the total occupancy of the Ä valleys also drops as electrons reach, in particular, the [001] X valleys in the second conduction band.

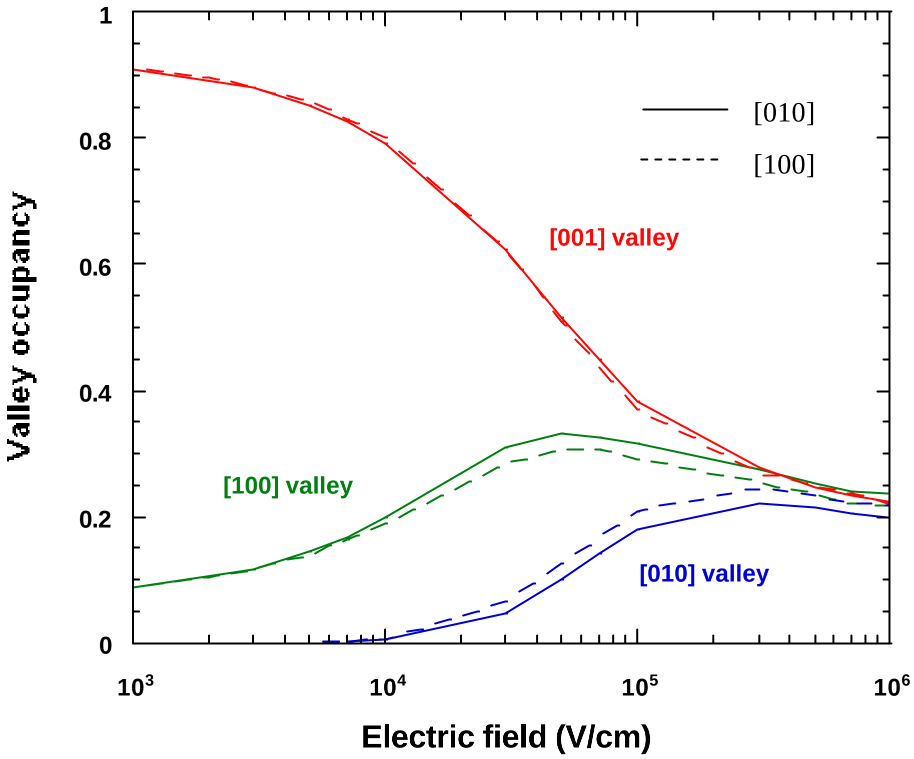

Figure 3.10. Electron distribution among Ä valleys for OS-Si grown on CS-$Si_{1-x}Ge_x$ sidewalls.

Fig. 3.11(a) presents the electron drift velocity for [100], [010] and [001] field orientations for OS-Si on CS-$Si_{0.8}Ge_{0.2}$, and Fig. 3.11(b) the associated average energies. Because most electrons occupy $Ä_{[001]}$ valleys at low and intermediate field strengths, most electrons have the smaller effective mass component m_t parallel to the field for either the [100] or [010] orientated field. As a consequence, the drift velocities and energy distributions are comparable for these two field orientations. At intermediate fields, however, the relative increase in electron concentration in the Ä$_{[100]}$ valley does lead to some splitting of the drift velocities. Electrons in the Ä$_{[100]}$ valleys have the heavier mass component m_l along the [100] field direction. For [001] orientated fields, on the other hand, most electrons have the heavier mass component m_l parallel to the field for low and intermediate field strengths. At low and moderate fields, this heavier mass results in somewhat lower average energies and a much lower drift velocities for this latter field orientation than for either [100] or [010] field orientation. At high fields where the carriers are more evenly distributed among the valleys (and where impact ionization dominates the energy loss) the average energies converge and the drift velocities merge to a saturation velocity of approximately 1.2×10^7 cm/s.

In the vertical n-MOSFET (Fig. 3.1), we are interested in the transport properties along the channel, the [010] direction, so the remaining calculations focus on the transport characteristics for [010] orientated fields. In Fig. 3.12(a) the drift velocities are compared for various Ge mole fractions, x=0.1, 0.2, 0.4 and 0.6, in the Si$_{1-x}$Ge$_x$ on which OS-Si sidewall is grown. Increasing Ge mole fraction produces more valley splitting and, thus, more electrons reside in the Ä$_{[001]}$ valleys, where the electron effective mass parallel to the field is the lighter value m_t. Valley splitting also suppresses the *f*-type intervalley scattering among neighboring Ä valleys causing drift velocities to increase with mole fraction at low and intermediate fields in OS-Si. The average energies, in Fig. 3.12(b) also increase a little correspondingly.

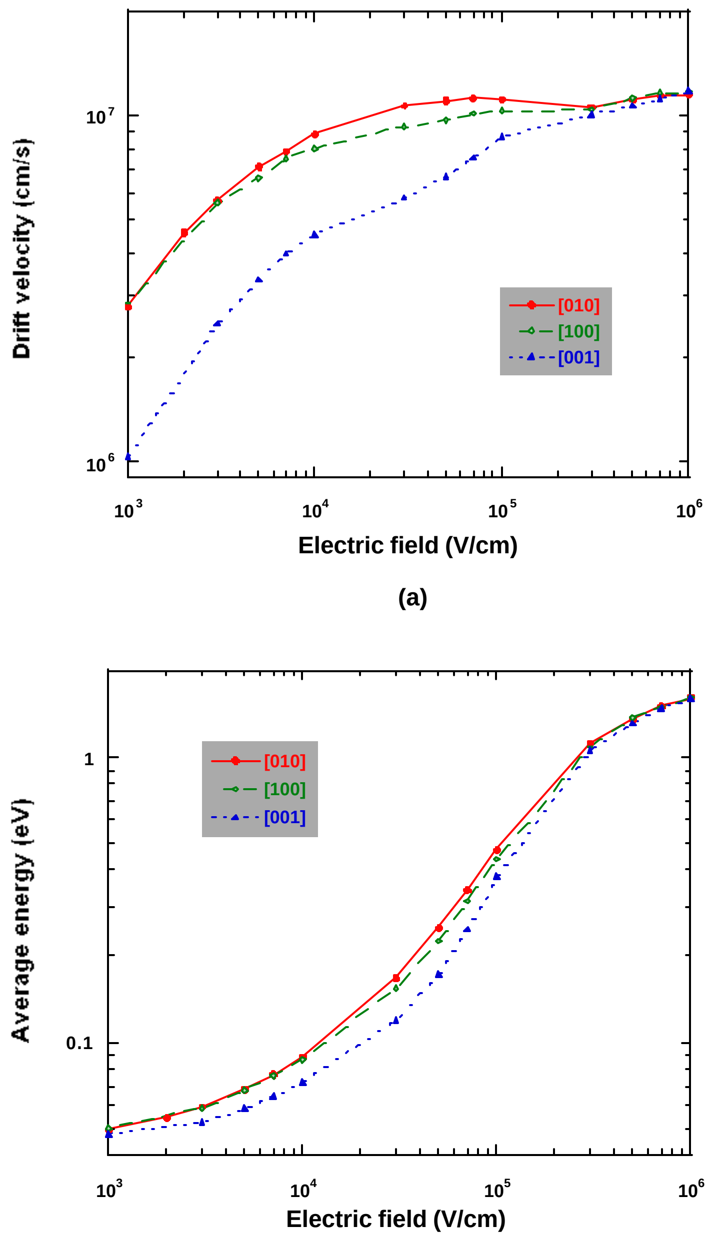

(a)

(b)

Figure 3.11. Transport properties for OS-Si grown on a $Si_{0.8}Ge_{0.2}$ sidewall as a function of electric field: (a) drift velocity; (b) average energy.

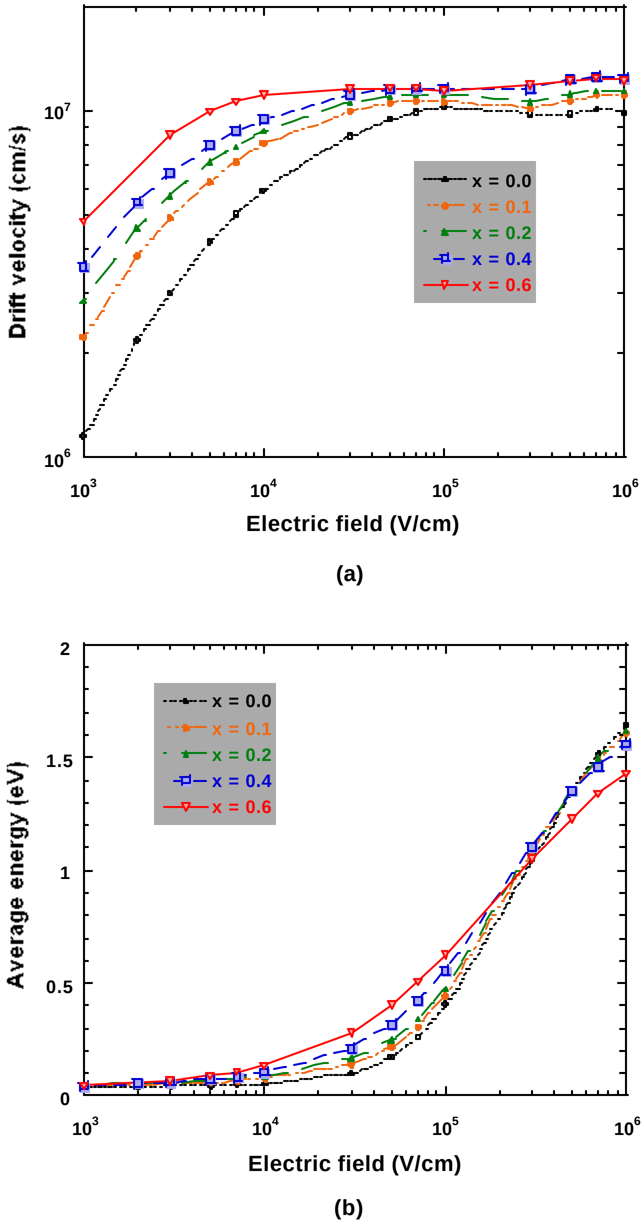

Figure 3.12. (a) Drift velocities; and (b) average energy for OS-Si grown on $Si_{1-x}Ge_x$ for field along [010] as a function of Ge mole fraction.

For hydrodynamic simulation, the energy relaxation time, ô, is an important parameter. In this work it is obtained from

$$\boldsymbol{t} = \frac{\langle E \rangle - \langle E_0 \rangle}{qFv_d} \ , \tag{3.4}$$

where $\langle E \rangle$ and $\langle E_0 \rangle$ are average electron energy and thermal energy in equilibrium, respectively, q is the electron charge, F is the magnitude of field and $\boldsymbol{n}_d$ is the drift velocity. The comparison of energy relaxation times for OS-Si and Si in Fig. 14 exhibits a strong relative enhancement of ô for OS-Si at low to moderate fields that increases with the Ge mole fraction. The increase in energy relaxation times suggests that significant velocity overshoot can be expected in vertical n-MOSFET devices with an OS-Si channel.

The calculated impact ionization coefficients in OS-Si are shown in Fig. 3.14. Yeom, Hinckley and Singh [Yeo94] suggest that the smaller band gap determines the impact ionization coefficients in strained $Si_{1-x}Ge_x$. The situations similar here except that there is no additional alloy scattering to reduce the rate. A larger impact ionization coefficient is obtained in OS-Si for larger Ge mole fraction as a result of the narrowing of the band gap in OS-Si (Eq. 3.1) which reduces the threshold energies for II. However, in the calculation for OS Si, only the threshold energies of the empirical II formula [Car93] were modified, according to the OS-Si energy gap. The reduction in the DOS above the band edge is not taken into account, so the calculated impact ionization coefficients for OS-Si may be slightly overestimated.

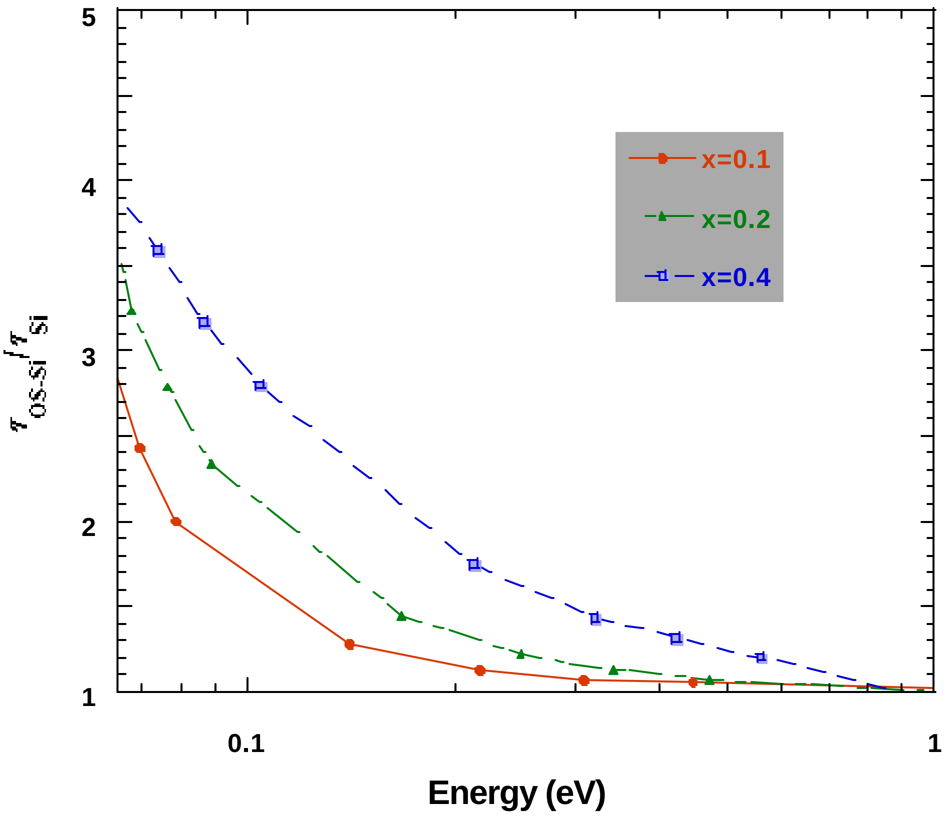

Figure 3.13. The ratio of energy relaxation times for OS-Si grown on $Si_{1-x}Ge_x$ to that of bulk Si as a function of average electron energy.

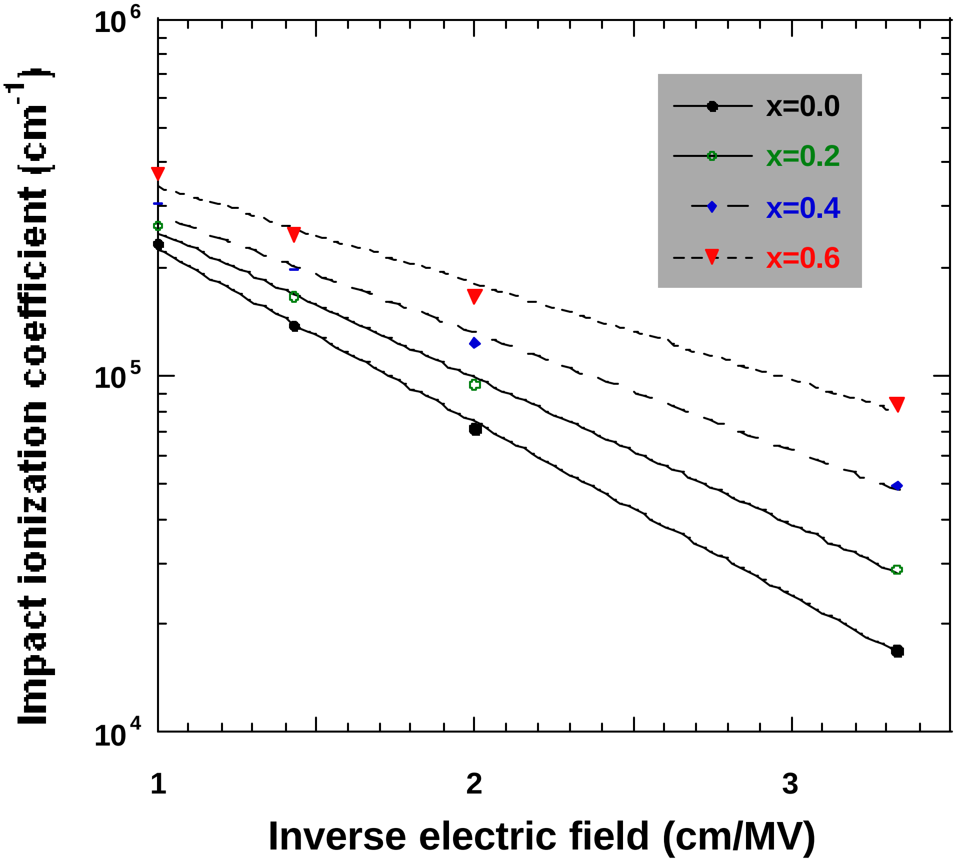

Figure 3.14. Impact ionization coefficients in OS-Si.

Table 3.2 shows the electron mobility enhancement in OS-Si. Compared with bulk Si, less *f*-type intervalley scattering and higher occupancy in the low lying Ä$_{[001]}$ valleys, which have lower effective mass component m_t in the field direction, increases the drift velocity. The mobility of OS-Si grown on Si$_{0.6}$Ge$_{0.4}$ can be twice as large as that of bulk Si.

In conventional TS-Si grown on a relaxed $Si_{1-x}Ge_x$ buffer layer, at low fields most electrons have the lower effective mass m_t in the field direction as in OS-Si. However, electrons in the next higher lying Ä alleys in OS-Si also have the lower effective mass m_t in the field direction, while electrons in the higher lying Ä valleys in TS Si are split among valleys with m_t in the field direction, and with the heavier effective mass m_l in the field direction. Thus, for moderate fields one would expect a higher drift velocity in OS-Si. Compared to the simulation results of TS-Si [Miy93], a comparable mobility but higher saturation velocity was found for OS-Si in this work. From a technological view point, the strain in OS-Si grown on a CS-$Si_{1-x}Ge_x$ is less than that in TS-Si on a relaxed $Si_{1-x}Ge_x$ layer, for the same Ge mole fraction, and, thus, OS-Si should have a larger critical layer thickness that will maintain the strain pseudomorphically. Finally, TS-Si requires a high quality relaxed $Si_{1-x}Ge_x$ buffer layer, which is more difficult to grow experimentally than the CS-$Si_{1-x}Ge_x$ layer used to obtain OS-Si. OS-Si thus has many of the advantages of TS-Si when grown in vertical devices on Si substrates.

Ge mole fraction x	$\frac{m_{OS-Si}}{m_{Si}}$
0.1	1.7
0.2	1.9
0.4	2.2
0.6	3.8

Table 3.2. Electron mobility enhancement of OS-Si. m_{Si} is the mobility of bulk Si.

CHAPTER FOUR

Strained Si nMOSFET

4.1 MOTIVATION

Silicon MOSFETs have been scaled down to deep sub-micron dimensions in order to increase the device performance. Scaling raises issues such as velocity saturation/overshoot effects, leakage current through gate oxide and polysilicon gate depletion effects. These issues may diminish the improvement caused by scaling. Further improvement requires more complicated device structures and cost more. Instead of scaling, changing the material properties provides another way to improve the device performance. As discussed in chapter 1, tensily-strained Si grown on relaxed SiGe has higher in-plane electron mobility and has been studied extensively for application in nMOSFETs in order to gain higher drain current than Si control device. In this chapter, the multi-material full-band Monte Carlo simulation tool is used to study electron transport in strained Si and device performance of strained Si nMOSFET.

4.2 ELECTRON BAND STRUCTURE OF TENSILY-STRAINED SI

The electron band structures of tensilely-strained (TS) Si are calculated by empirical pseudopotential method (EPM). The calculation details are described in Sec. 2.2.2 and relevant references. Strain in TS Si breaks the symmetry in unstrained Si. Thus the energy degeneracy points in momentum space may split into different values. Among them, the most important splitting happens at the bottom of Δ valleys in first conduction bands. If we assume the growth direction is along z axis, the bottom of Δ valleys along z direction, $E_{[001]}$, have lower energy than those of Δ valleys along x and y direction, $E_{[100]}$ and $E_{[010]}$. Fig. 4.1 shows the valley splitting versus Ge mole fractions in SiGe substrates. We set the bottom of Δ along z direction as energy reference. The valley splitting is linearly proportionally to Ge mole fraction. The valley splitting causes the decrease and shifts in density of states (Fig. 4.2). Correspondingly the scattering rates decrease, which induces high low field mobility. Besides the valley splitting we also show the effective masses change with strain in strain Si in Fig. 4.3. In low field region, most of carriers occupy the valleys in growth direction. In Fig.4.3 only effective masses m_l and m_t of those valleys are shown. Longitudinal effective mass slightly decreases with Ge mole fraction of substrate, while the transverse component increases a bit. So in the strain cases considered in the work, the effective mass change should have no effects on carrier transport. In TS Si, the band gap decrease with Ge mole fraction (Fig. 4.4), which lower the threshold energy in impact ionization process.

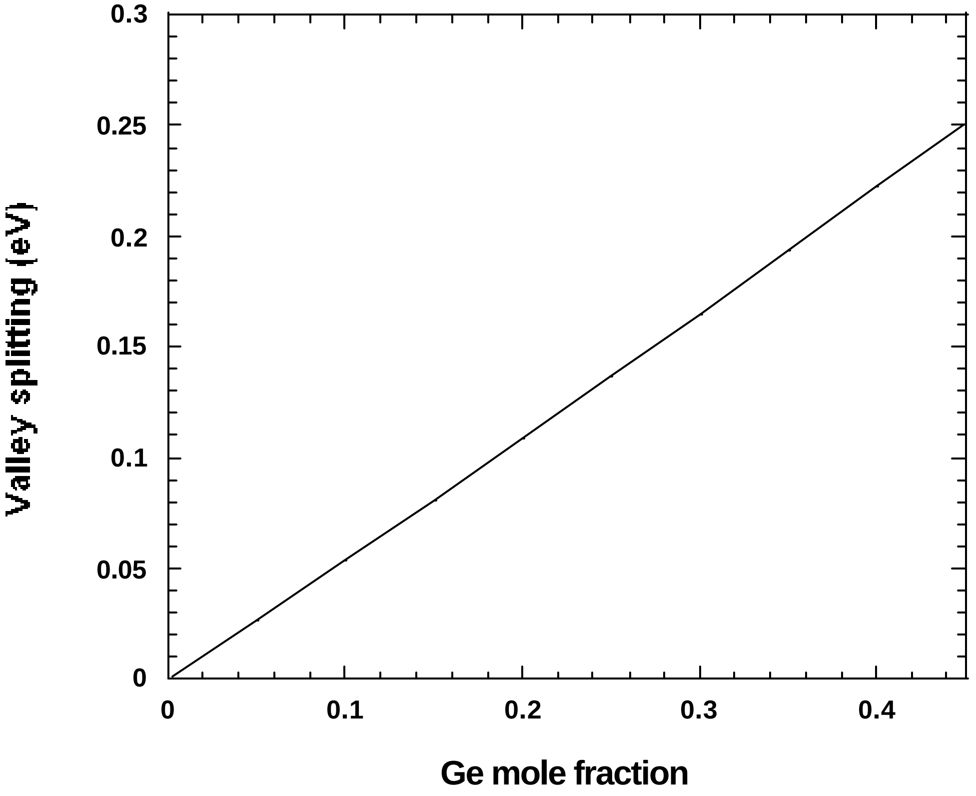

Figure 4.1. Energy splittings between the bottom of in-plane and out-of plane valleys in TS-Si grown on relaxed SiGe.

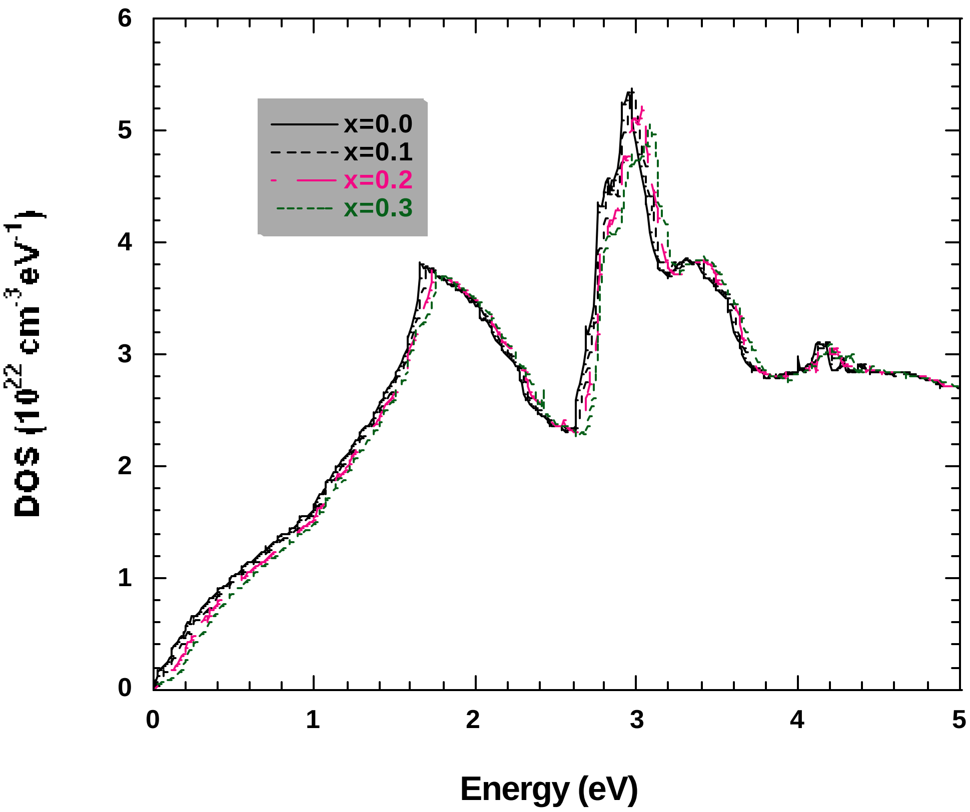

Figure 4.2. Density-of-states in conduction bands of various strained Si systems.

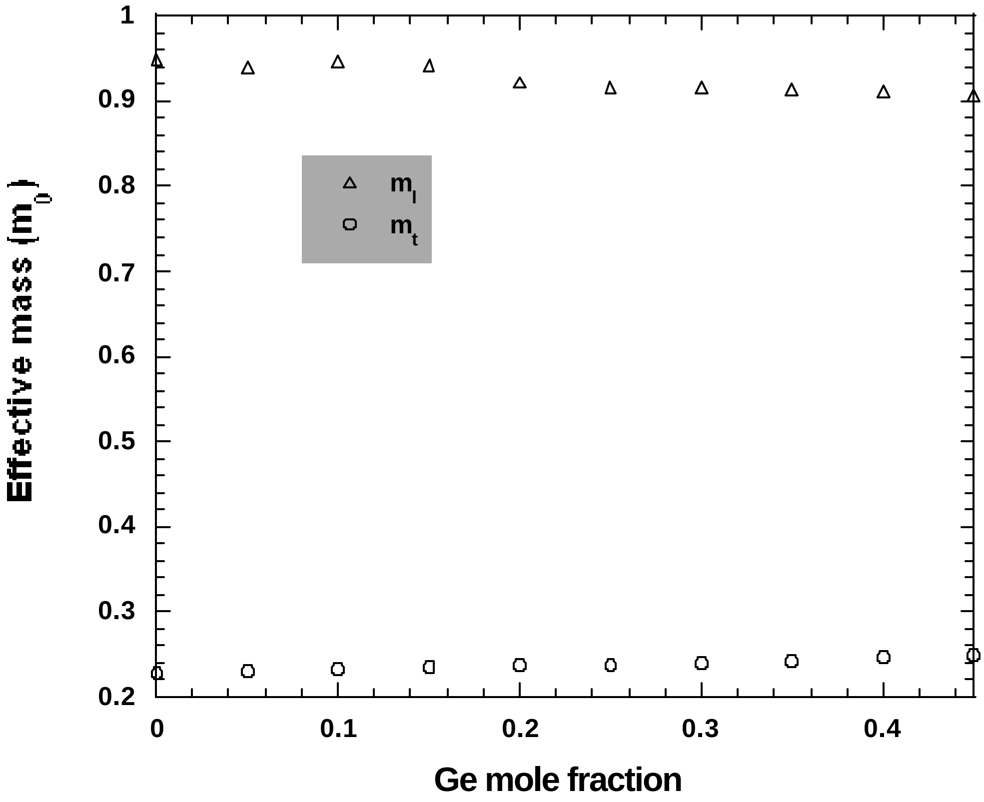

Figure 4.3. Longitudinal and transverse effective masses of the valleys in growth direction (with lowest energy) in strained Si grown on relaxed SiGe.

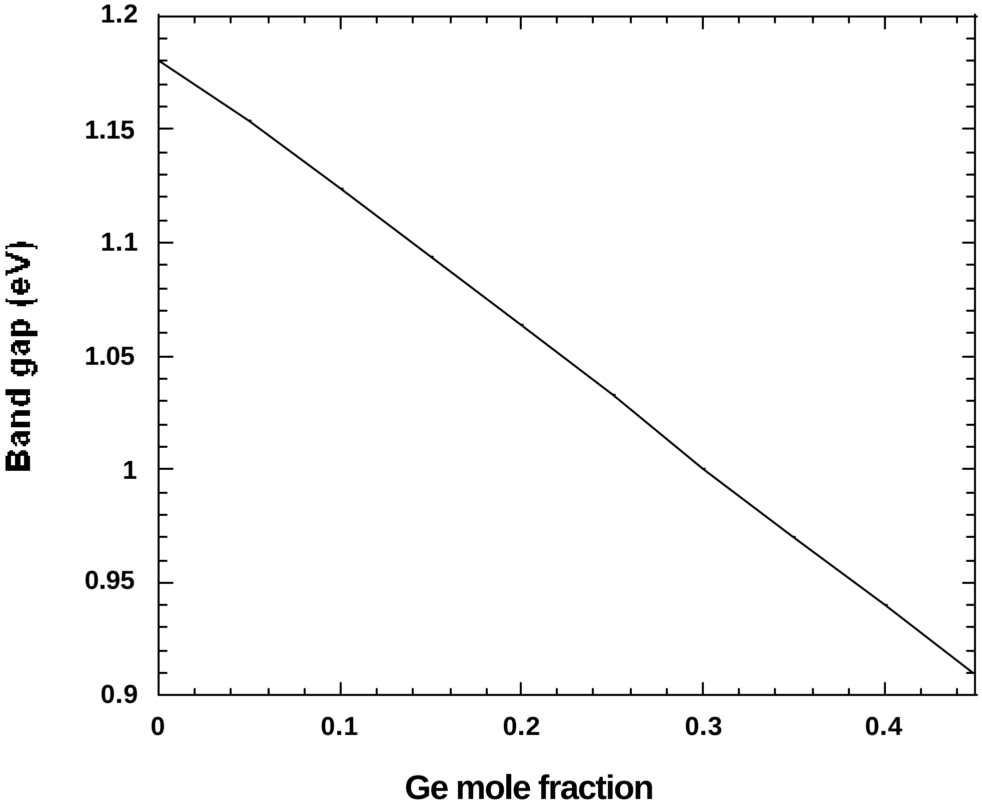

Figure 4.4. Band gap lowering in strained Si grown on relaxed SiGe.

4.3 CALIBRATION OF ELECTRON TRANSPORT IN BULK SI

In the study of electron transport of strained Si using MC method, we first need to calibrate the transport properties of bulk Si. Since the device is operated at room temperature, in the following we focus on the transport properties at 300 K. In the calibration, the phonon scattering coupling constants in Eq. 2.13 are adjusted to match the simulated velocity-field characteristics from low to high fields region to measurements (Canali *et. al.* [Can75]) and other simulation (Jacoboni *et. al.* [Jac83] and Fischetti *et. al.* [Fis88]) results. Our best-fitting set is:

$$\begin{aligned}
\Delta_{LA} &= \begin{cases} 3.54\, eV & (1st\ band) \\ 3.0\, eV & (higher\ bands) \end{cases} \\
\Delta_{TA} &= \begin{cases} 1.49\, eV & (1st\ band) \\ 1.0\, eV & (higher\ bands) \end{cases} . \\
\Delta K_{op} &= \begin{cases} 5.6\times 10^{8}\, eVcm^{-1} & (1st\ band) \\ 6.0\times 10^{8} eVcm^{-1} & (higher\ bands) \end{cases}
\end{aligned} \tag{3.1}$$

Fig. 4.5(a) shows the electron velocities at the various fields. As we know, the velocity is linearly proportional to the field at low fields and saturates at high fields. Compared with experimental and other simulation results, the coupling constants used in this work give good agreements in velocity-field curve. In the average energy-field curve, Fig. 4.5(b), at low field the energy values from our study are a little higher than in Fischetti and Jacoboni's studies, while our energy values at high field are between the results of their works. It should be emphasized is that this set is not unique. Other sets can match the same velocity-field plot. The low-field mobility of electron decreases with the increase of impurity scattering shown in Fig. 4.6. It is noted that the simulation results based on Ridley's model agree well with Jacaboni's simulation [Jac83] in the large range of doping concentration. Also the mobility change due to the surface roughness scattering in various effective vertical fields is plotted in Fig. 4.7. Takagi's universal mobility [Tak92] curve is well reproduced by this work.

In the study of strained Si, we neglected differences in the phonon system between strained and unstrained Si. Hence the same set of coupling constants are applied in the strained Si case. Also we assume the impurity scattering in strained Si are the same as those in unstrained Si. Although the surface roughness between oxide and strained Si may be different from that between oxide and unstrained Si, we assume the same treatment in strained Si case to simplify the simulation. The emphasis in strained Si study is on the strain-induced valley splitting and its effect on the electron transport. These simplifications can isolate the strain effects on transport. Also no contradiction is noticed by comparing with other simulation models.

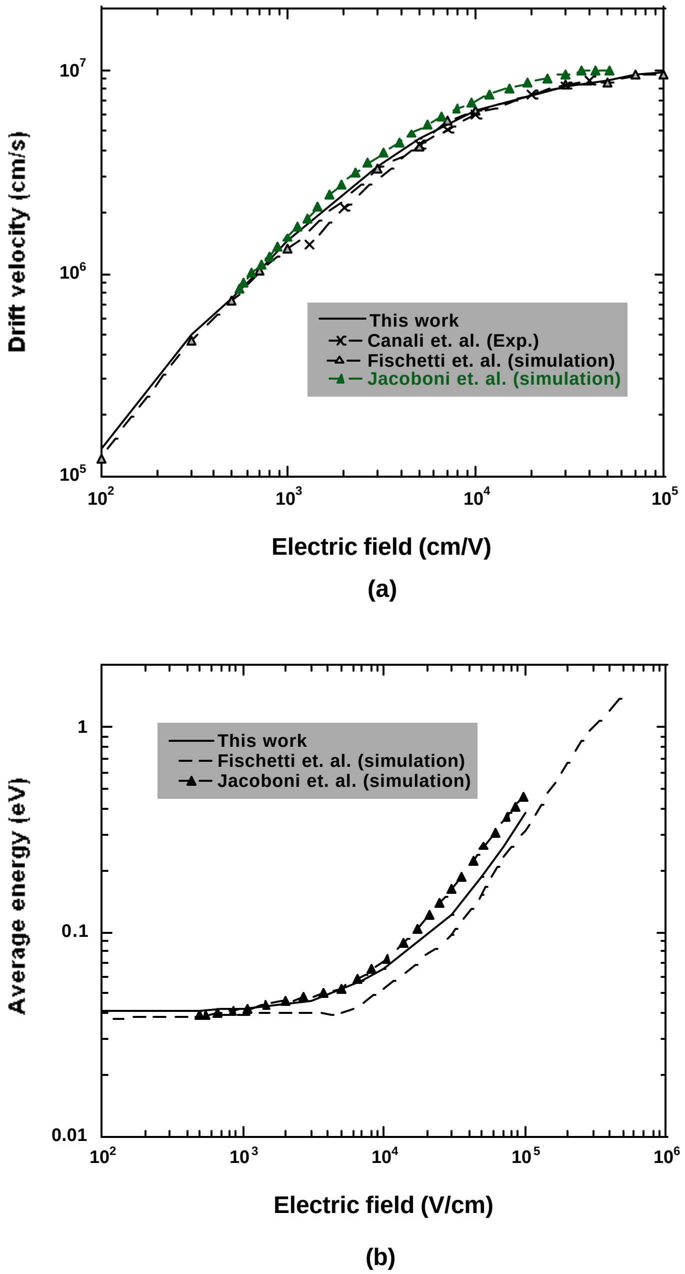

Figure 4.5. (a) Drift velocity of electron in bulk Si as a function of electric field. (b) Average energy of electron in bulk Si as a function of electric field. For comparison, the measurements and simulation results are also shown.

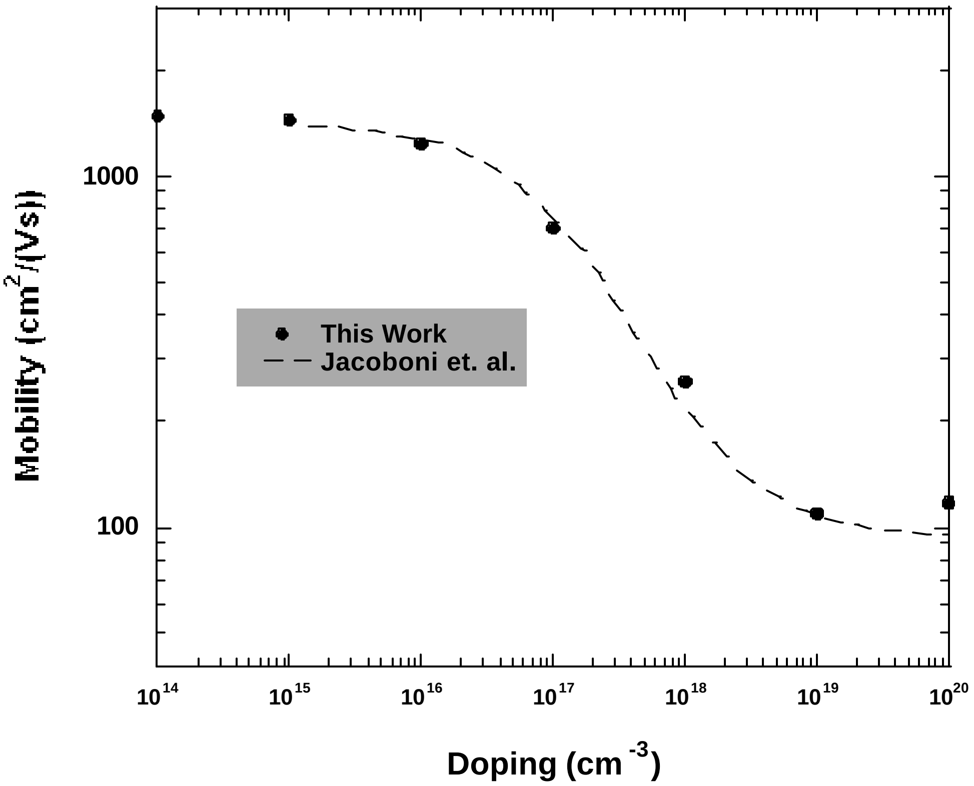

Figure 4.6. Low-field electron mobility versus doping concentrations.

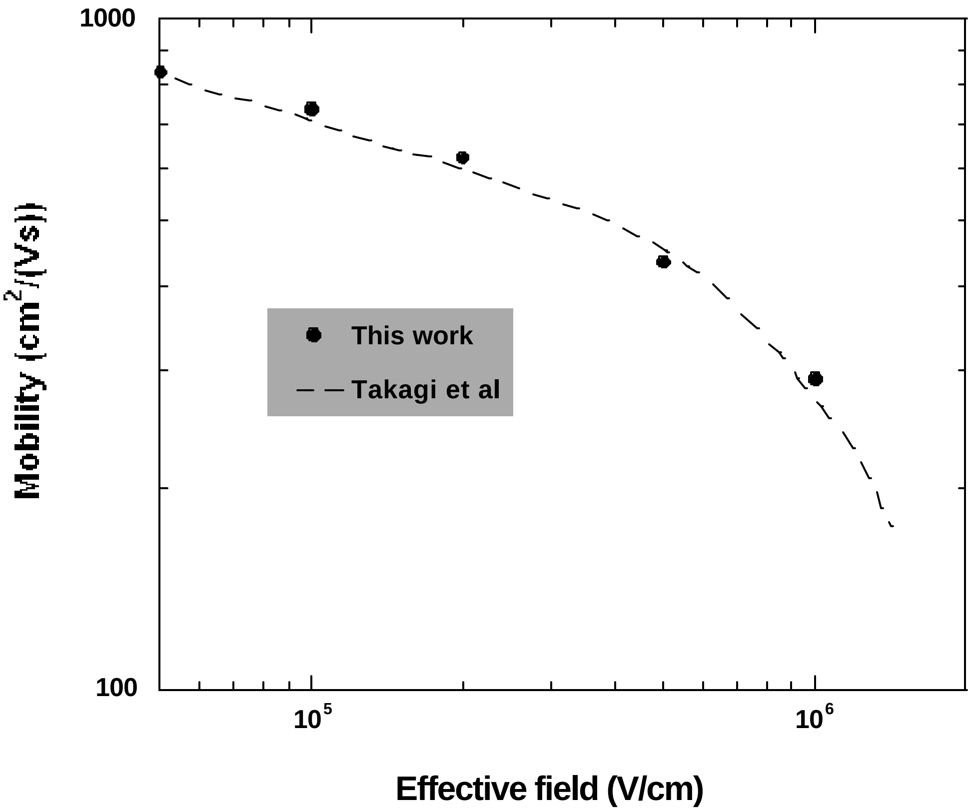

Figure 4.7. Low-field mobility as a function of normal effective field.

4.4 THE SCATTERING RATES

As mentioned in Sec. 4.1, the scattering rates are reduced by the valley splitting in strained Si. Fig. 4.8 show the comparisons of total phonon scattering rates between unstrained Si and strained Si grown on SiGe substrate with 30% Ge. We show only the first conduction band scattering rates to simplify the plot. In low energy region (0-1.7eV) the scattering rates of strained Si are lower than those of unstrained Si. At higher region, the valley splitting causes the scattering rates to be lower and shift to higher energy region. In order to show the scattering rate at low energies the acoustic and optical phonon scattering rates below 0.5eV are shown in Fig. 4.9 (a) and (b). In that energy region the scattering rates of strained Si are much lower than those of Si. The step at 20 meV in acoustic phonon emission rate of unstrained Si corresponds to the *f*-type intervalley scattering. In strained Si the onset of *f*-type intervalley scattering is around 180 meV, where the extra 160 meV comes from the valley splitting (Fig. 4.1). The effect of valley splitting is more obvious in optical phonon emission scattering rates. The onset of optical phonon emission scattering is at 62 meV which is the optical phonon energy. In strained Si, the onset of intravalley optical phonon emission scattering for electron in higher energy valleys is around 220 meV with the bottom the lowest valley as energy reference. Thus there is a step around 220 meV in optical phonon emission scattering in strained Si.

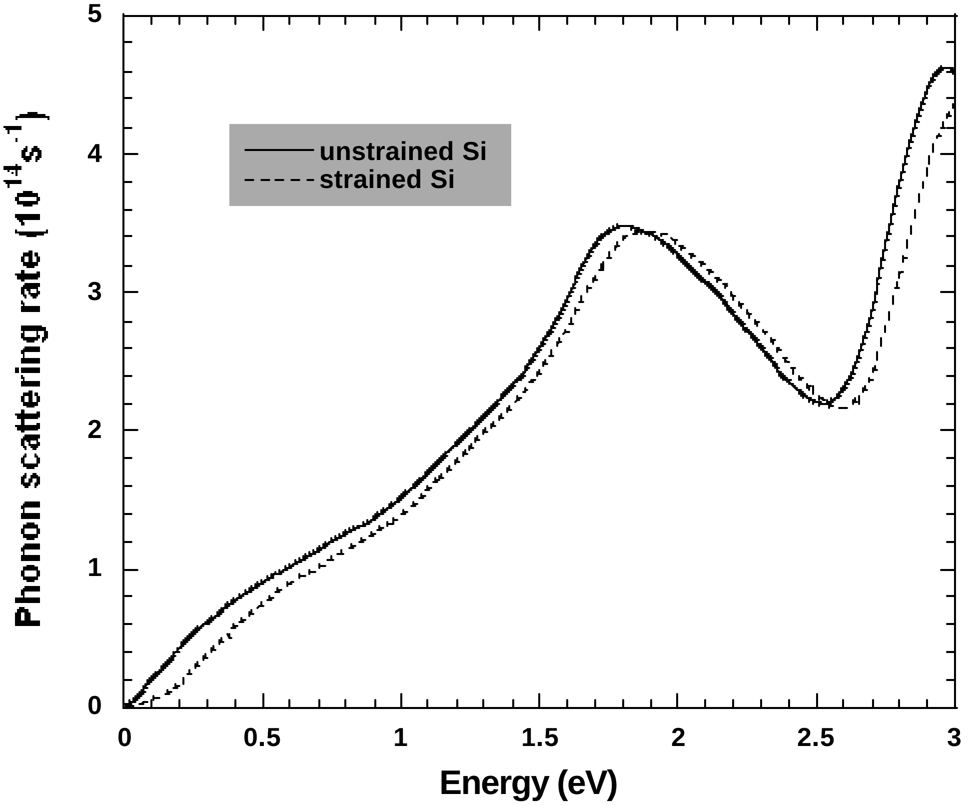

Figure 4.8. Total phonon scattering rates of unstrained Si and strained Si grown on relaxed $Si_{0.7}Ge_{0.3}$.

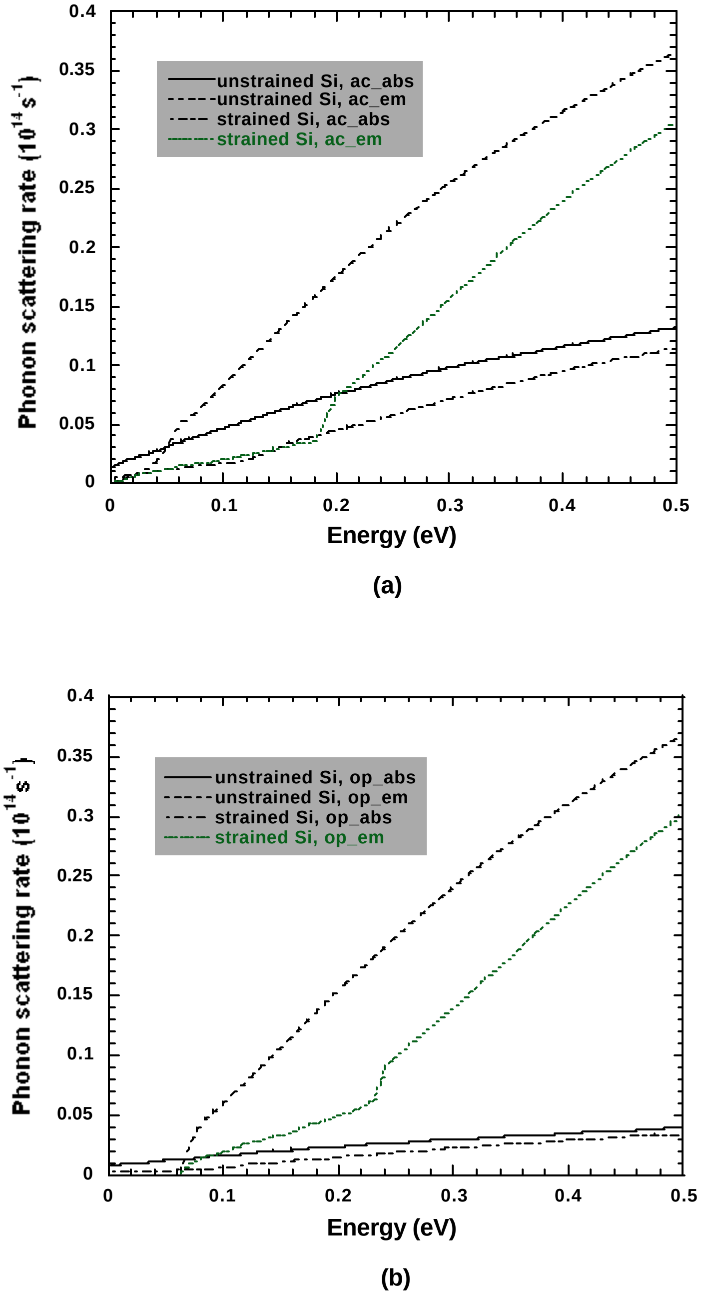

Figure 4.9. Detailed comparison of phonon scattering between unstrained Si and strained Si on relaxed $Si_{0.7}Ge_{0.3}$ in low energy regime. (a) Acoustic phonon scattering. (b) Optical phonon scattering.

4.5 TRANSPORT SIMULATION RESULTS

4.5.1 Tensily-strained Silicon

As we know, the scattering rates in strained Si are smaller than those in unstrained Si due to the valley splitting. The splitting also makes most of electrons occupy the lowest valleys (along growth direction [001]) at low external fields. Thus under the fields ([100] or [010]) perpendicular to the growth directions the electrons have lower effective mass, m_t, and drift velocity at low field is enhanced compared with unstrained Si. But under the field along the growth direction the velocity is lower than that of unstrained Si due to the larger effective mass, m_l. Fig. 4.10(a) shows the drift velocities of strained Si (at 300K and without impurity doping) grown on SiGe with 30% Ge. Compared with experimental measurements [Ism93], the simulation results match well in intermediate field region and are higher at low field region. We also found that the saturation velocity of strained Si is still around 1e7 cm/s, but the velocity saturation occurs at lower field that unstrained Si. The average energy versus field relation is also shown in Fig 4.10(b). Corresponding to the higher drift velocity under the field along [100] direction, the electrons have higher energy.

We found the mobility enhancement saturates for strained Si grown on $Si_{0.75}Ge_{0.25}$ (Fig. 4.11). The saturation mobility enhancement is around a factor of two. One recognizes that the valley splitting of strained Si on SiGe with 25% Ge is approximately 130 meV, which is much larger than thermal energy (around 40 meV). At low fields, most of electrons stay in the lower energy states and have little chance to be scattered into high energy valley. Thus the variation of band structure at high energy region (above 130 meV) do not affect the electron transport.

It is well know that the surface roughness scattering degrades the electron mobility. After considering the surface roughness scattering, the mobility (Fig. 4.12) in strained Si is also reduced from the value, without taking the surface roughness into account. The mobility enhancement over unstrained Si also lower edto around 1.5 instead of 2 in strained Si on $Si_{0.7}Ge_{0.3}$.

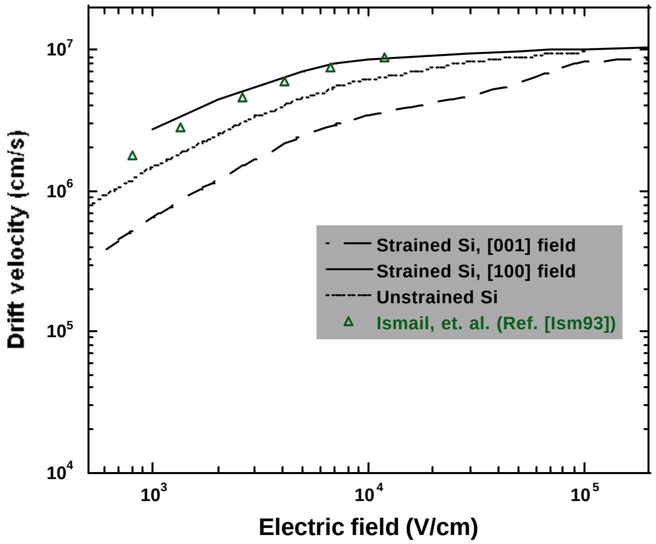

(a)

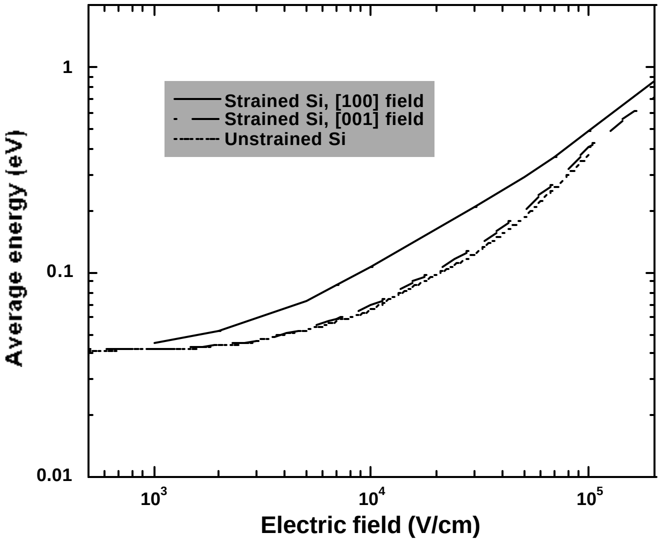

(b)

Figure 4.10. (a) Electron drift velocity of strained Si on relaxed $Si_{0.7}Ge_{0.3}$ under fields along [100] and [001]. (b) Average energy of strained Si. As a comparison the corresponding unstrained Si values are also shown.

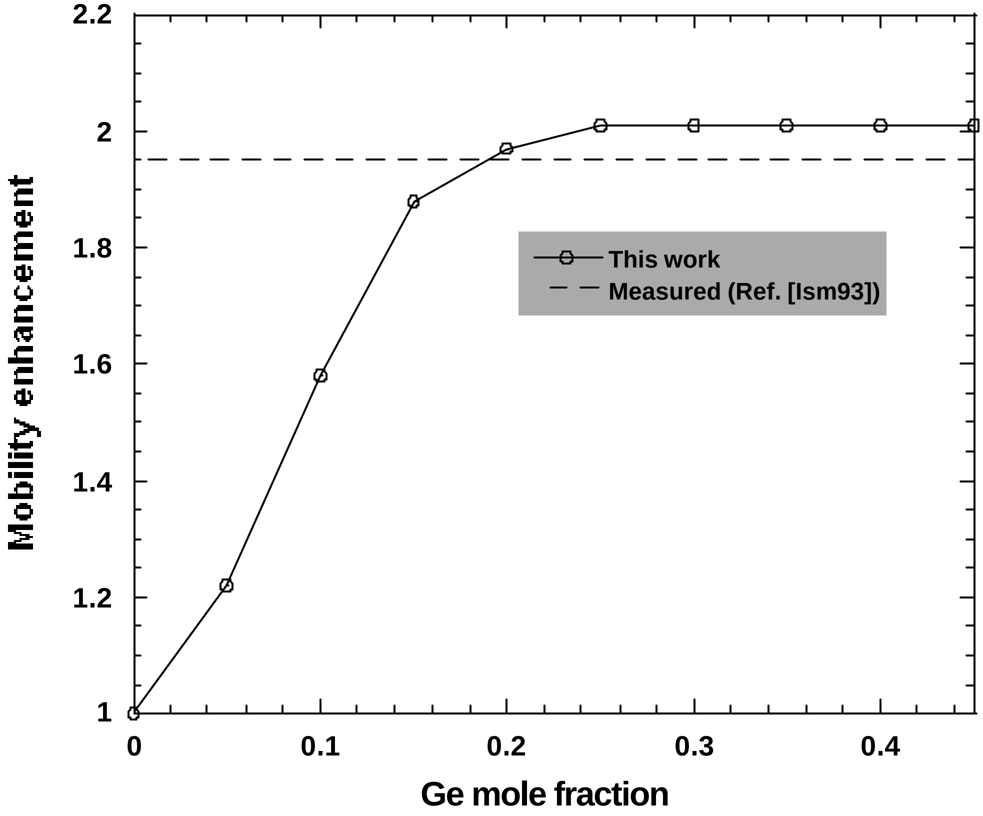

Figure 4.11. The mobility enhancement of various strained Si layer on $Si_{1-x}Ge_x$ compared to unstrained Si.

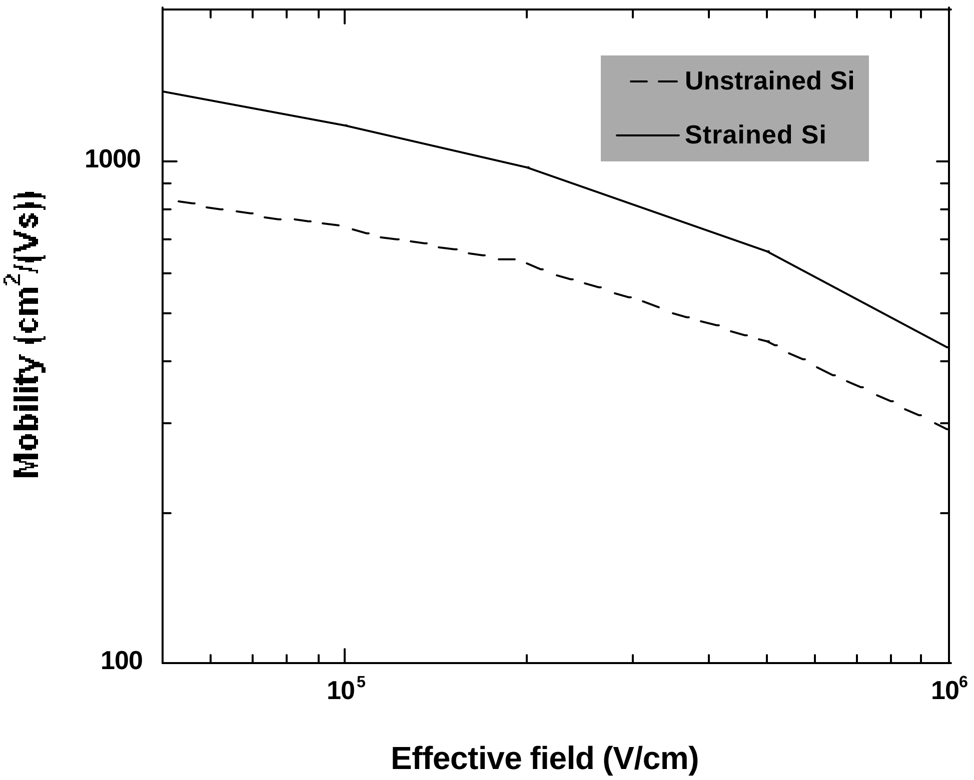

Figure 4.12. Mobility of strained Si on relaxed $Si_{0.7}Ge_{0.3}$ for different normal fields.

4.5.2 50 nm strained Si nMOSFET

We applied the multi-material strained Si code to study the device performance enhancement in strained Si nMOSFET. MIT's 50nm well-tempered device profile [Ant99] was employed. The doping profiles along Si/SiO_2 interface and poly gate are shown in Fig. 4.13. Also the growth direction of strained Si in the device is normal to the Si/SiO_2 interface. This arrangement makes the channel be perpendicular to the growth direction. From Fig. 4.10(a), we know that along that direction strained Si has higher drift velocity. We simulated the 50 nm nMOSFET with unstrained Si and strained Si with 30% Ge in its substrate. In order to emphasize the effect of strained Si, we simply change the material type in the device without considering the threshold voltage change and surface roughness variation with strained Si. Thus the differences in results purely come from the material properties.

The drain current, I_d, versus drain bias, V_d, relation is given in Fig. 4.14 with gate bias, $V_g = 1.2\,\mathrm{V}$. Compared with the drain current in unstrained Si device, the enhancement in drain current of strained Si is around 60%, which corresponds to the mobility enhancement with surface roughness scattering. Also the 60% enhancement in current is maintained in high drain bias. The detailed distribution of average velocity in channel direction and average energy at a low drain bias ($V_d = 0.2\,\mathrm{V}$) are plotted in Fig. 4.15(a) and (b). Under the low drain bias most of channel region is at low field and the electrons have low-field transport properties. So one notes that the velocities in the entire channel of strained Si device are higher than those of unstrained Si. Under a high drain bias ($V_d = 1.2\,\mathrm{V}$), the fields in the channel region close to drain are increased to be higher than 2e5 V/cm where drift velocities saturate in both unstrained and strained Si (see Fig. 4.10(a)). So there is no difference in velocity near drain region at higher bias device (Fig. 4.16(a)) and the average energy (Fig. 4.16(b)) in that region is higher than the valleys splitting (Fig.4.1), which degrades the strain effect. But the difference in velocity near source region is still sufficient. The current in short-channel device is controlled by source region [Lun97]. In that region low-field mobility enhancement is applicable in strained Si. That explains the same current improvement at high drain bias as that at low bias. Fig. 4.17 and Fig. 4.18 give the detailed electron energy distribution in both unstrained and strained Si at various locations. The high-energy tail is larger in strained Si, particularly in the drain region.

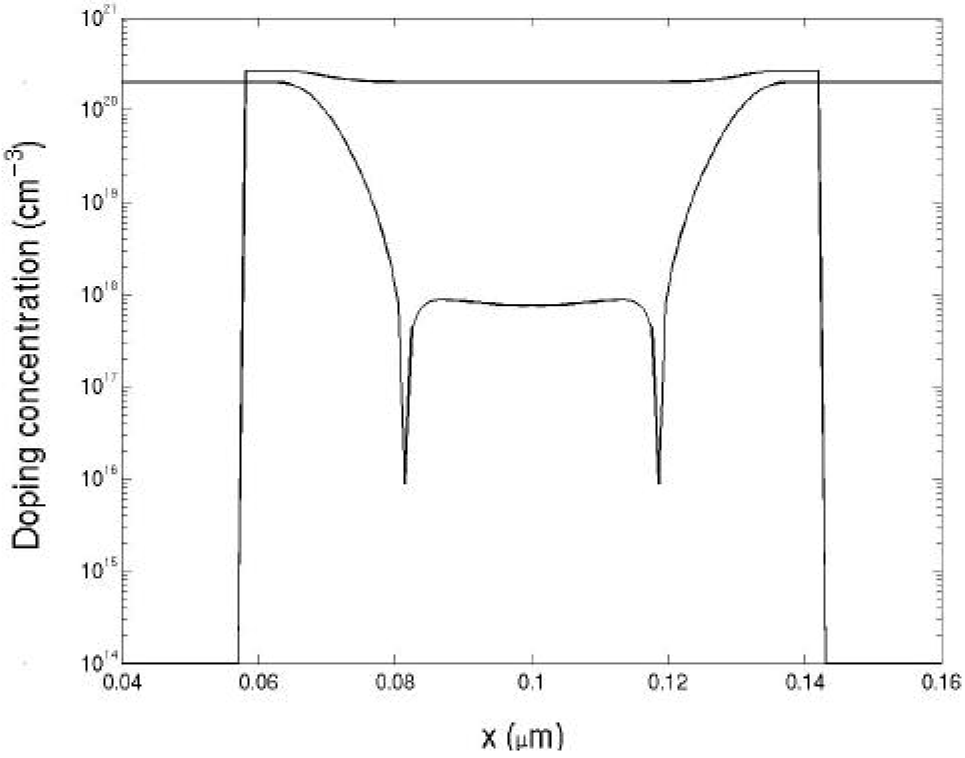

Figure 4.13. The doping profiles along channel/oxide interface and polygate of MIT wtm50nm device.

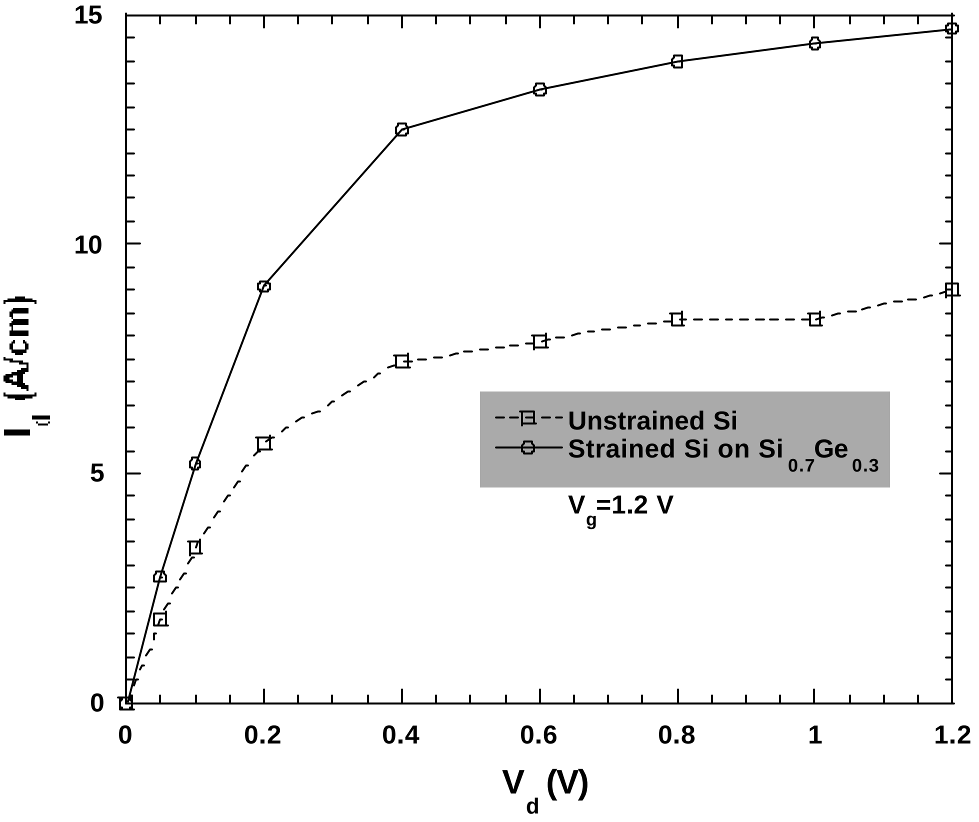

Figure 4.14. Drain current of MIT wtm50nm devices with unstrained Si and strained Si for gate voltage at 1.2V.

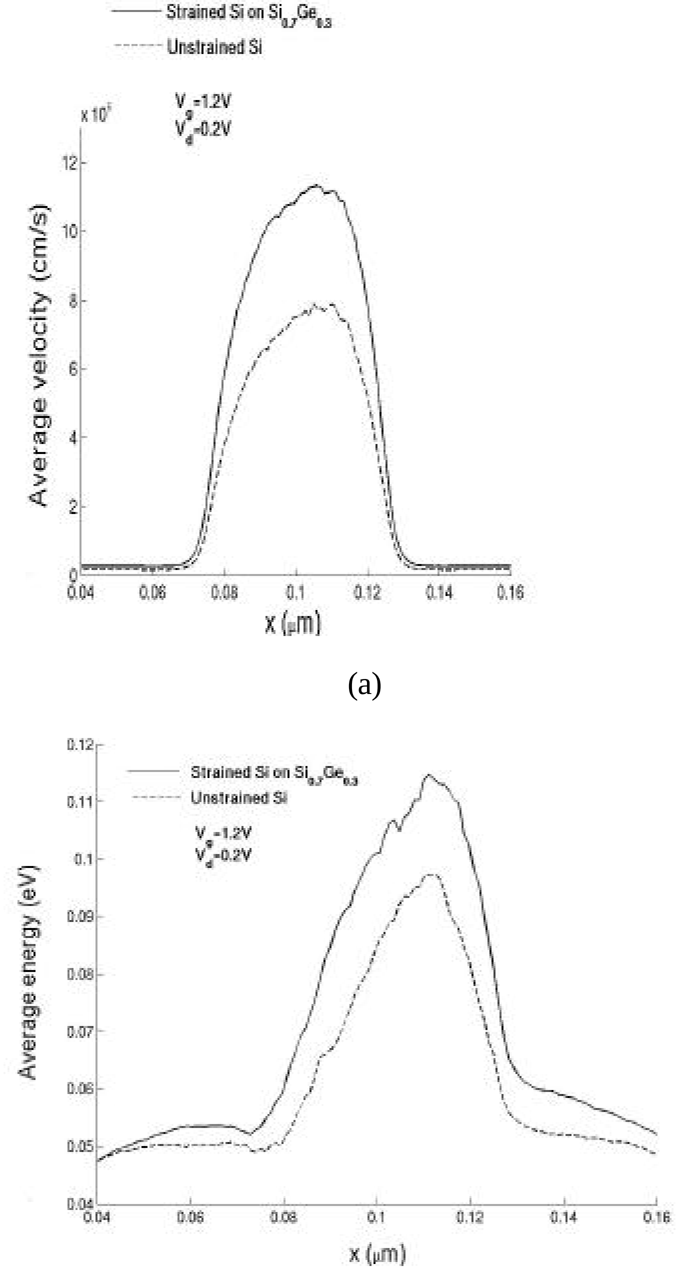

(a)

(b)

Figure 4.15. Average velocity and energy profiles along x axis in unstrained and strained Si wtm50nm devices with V_g=1.2V and V_d=0.2V.

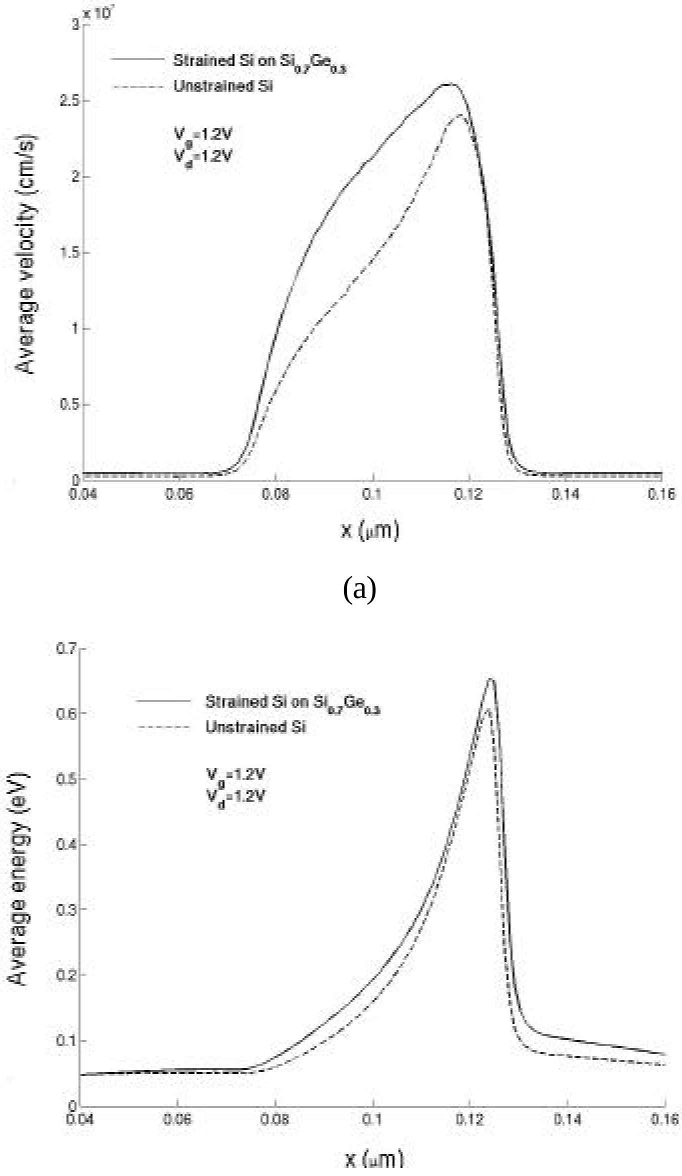

(a)

(b)

Figure 4.16. Integrated average velocity and energy profiles along x axis in unstrained and strained Si wtm50nm devices with V_g=1.2V and Vd=1.2V.

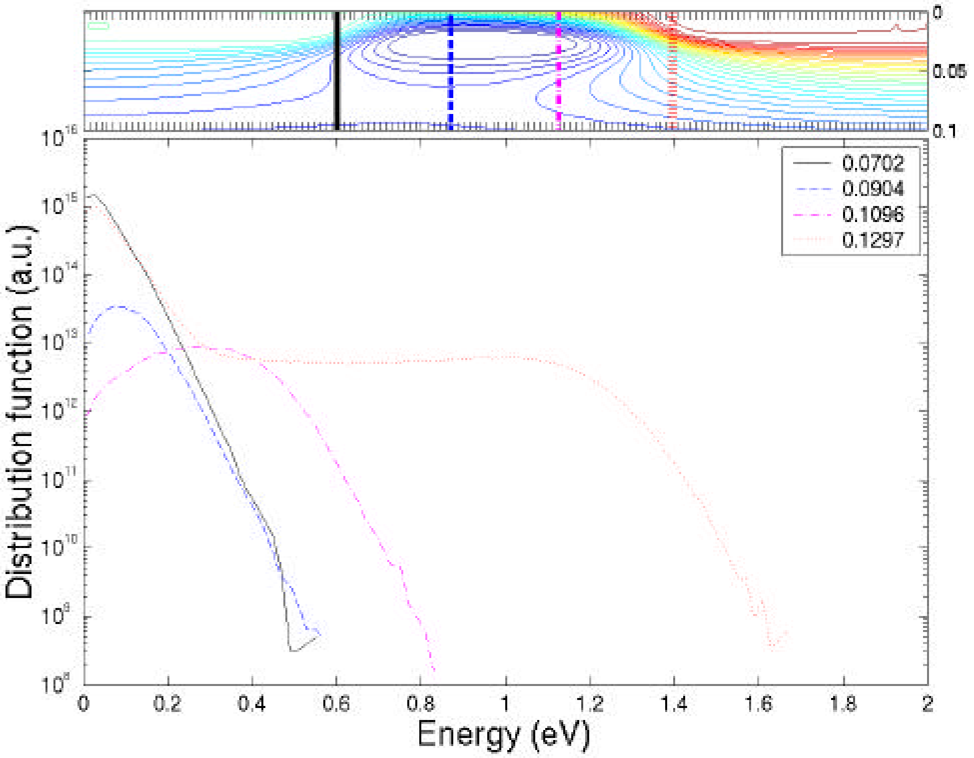

Figure 4.17. Energy distribution at various locations in channel of strained Si wtm50nm devices with V_g=1.2V and V_d=0.2V.

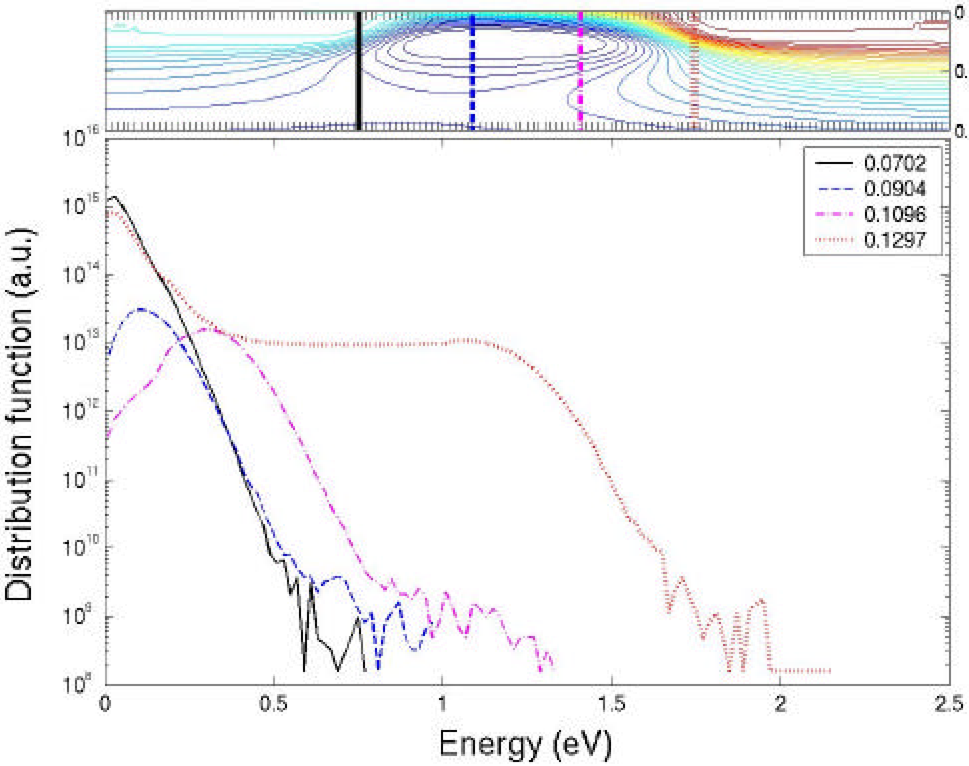

Figure 4.18. Energy distribution at various locations in channel of strained Si wtm50nm devices with V_g=1.2V and V_d=1.2V.

CHAPTER FIVE

Strained SiGe pMOSFET

5.1 MOTIVATION

Improvements of hole transport in pMOSFET have been made by scaling down the channel length and gate oxide thickness. Despite this progress, the drive current in pMOSFET is still not comparable with that in nMOSFET due to the lower hole mobility. That prevents decreasing the width of pMOSFETs in CMOS technology as much as for nMOSFETs. To further improve the drive current at current technology levels, compressively-strained (CS) SiGe is of interest [Sop94] [Ism94] in pMOSFET by exploiting the higher hole mobility in strained SiGe. Further, the large valence band offset in Si/SiGe heterojunction can be used to tailor the channel potential distribution in order to achieve hole acceleration and confinement. In this chapter, we employ the multi-material Monte Carol simulation tool to study the hole transport in strained SiGe material and a simplified pMOSFET with Si/SiGe heterojunction.

5.2 BAND STRUCTURE OF COMPRESSIVELY-STRAINED SIGE

The valence band structures of compressively-strained (CS) SiGe are obtained from tight-binding calculation. The calculation details are described in Sec. 2.2.3 and relevant references. As we know from chapter 2, strain in CS-SiGe splits the heavy and light-hole band degeneracy at the Γ point, and the heavy-hole band has lower energy. The band splitting shown in Fig. 5.1 is linearly proportional to Ge mole fraction. The band splitting causes the decrease and shift in density-of-states (Fig. 5.2). Correspondingly, the scattering rates decrease, which induces high low field mobility. Besides the valley splitting we also show the effective masses change with strain in CS-SiGe in Fig. 5.3. As we know heavy- and light-hole bands at Γ points are warped. So it is hard to model this in terms of a single effective mass. Thus the effective masses along [100], [110] and [111] are shown to describe the whole picture of valence bands and their variation with strain. In the CS-SiGe, the band gap shown in Fig. 5.4 also linearly decreases with Ge mole fraction, which lowers the threshold energy in an impact ionization process.

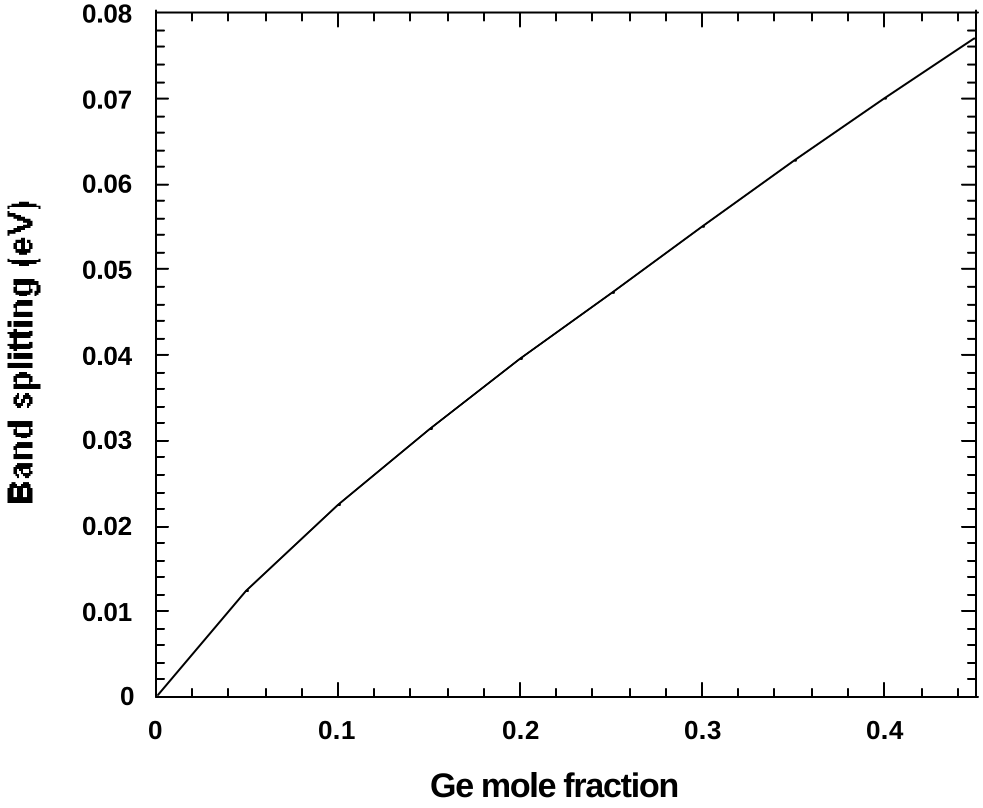

Figure 5.1. Energy splitting between the bottom of the heavy- and light-hole bands in CS-SiGe.

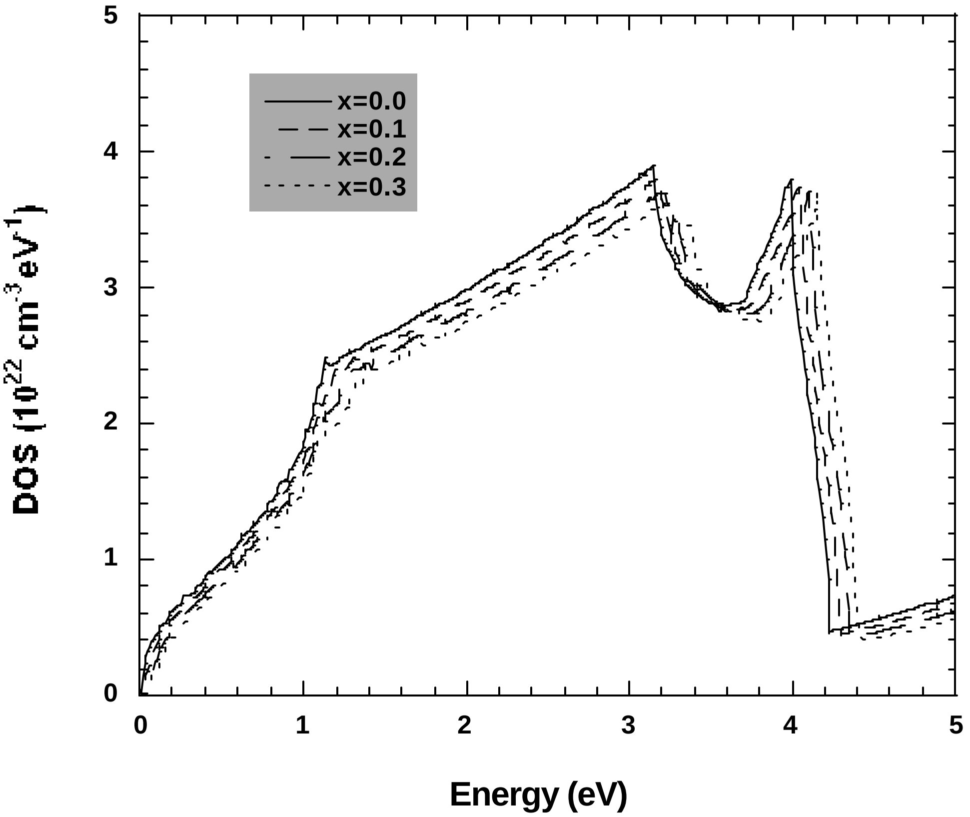

Figure 5.2. Density-of-states in valence bands of various CS-SiGe.

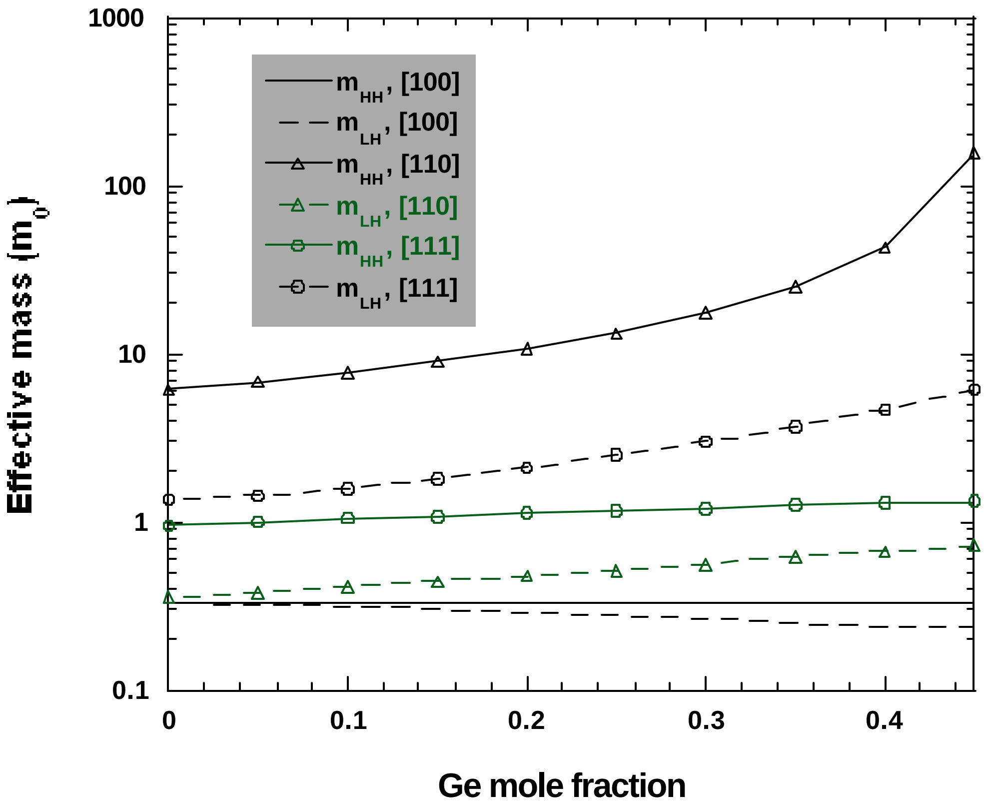

Figure 5.3. Heavy hole (HH) and light hole (LH) effective masses along [100], [110] and [111] directions in CS-SiGe.

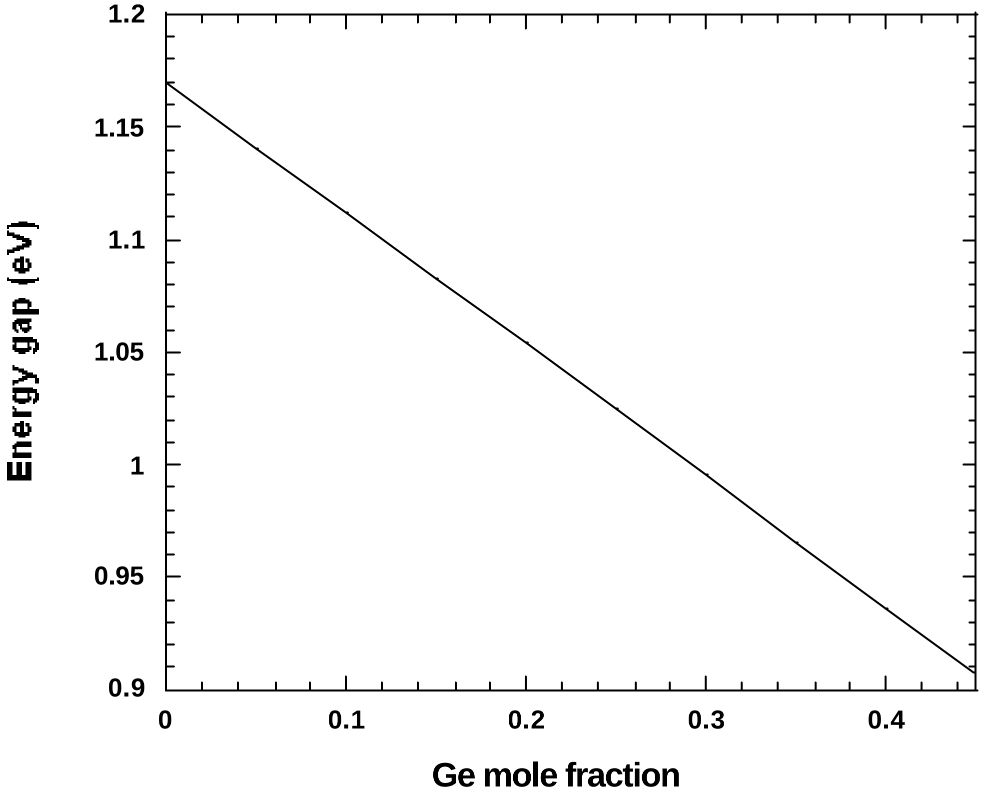

Figure 5.4. Band gap lowering in CS-SiGe.

5.3 CALIBRATION OF HOLE TRANSPORT IN UNSTRAINED SI AND GE

In the study of hole transport in strained SiGe, we first calibrate the hole transport properties in bulk Si and Ge. Also same as in the study of electron transport, we focus on the transport simulation at room temperature. The coupling constants in phonon scattering rates, Eq. 2.13, are adjusted to fit the simulated drift velocity-electric field relation to experimental [Ott75] and other simulation results [Fis88][Yam95][Jac77][Bjo99]. Our best-fitting set for Si is:

$$\begin{aligned} &\Delta_{LA} = \Delta_{TA} = 1.6\ eV \qquad (\mathit{four\ bands}) \\ &\Delta K_{op} = 4.5\times10^{8} eVcm^{-1} \quad (\mathit{four\ bands}); \end{aligned} \tag{5.1}$$

and for Ge is

$$\begin{aligned} &\Delta_{LA} = \Delta_{TA} = \begin{cases} 1.6eV & (1st\ and\ 2nd\ bands) \\ 1.2eV & (higher\ bands) \end{cases} \\ &\Delta K_{op} = \begin{cases} 4.6\times10^{8} eVcm^{-1} & (1st\ and\ 2nd\ band) \\ 2.0\times10^{8} eVcm^{-1} & (higher\ bands) \end{cases}. \end{aligned} \tag{5.2}$$

Fig. 5.5(a) and (b) show the drift velocity and average energy characteristics of holes in bulk Si for the various fields. Compared with experimental and other simulation results, the simulated results in this work give good agreement in velocity-field curve at low and intermediate fields. But the saturation velocity is higher than in other studies. In the average-field curve (Fig. 5.5(b)), the situation is more complicated. At low fields region, Fischetti [Fis88] and Jacoboni's [Jac77] results are around or lower than $3/2kT$ (the thermal energy under parabolic assumption). We know the heavy and light-hole bands are warped, where the thermal energy is higher than $3/2kT$. Our result is in good agreement with Bjorn's work [Bjo99]. At the high energy region, the difference among previous works is quite large. Our results are in between.

Fig. 5.6 gives the velocity and energy characteristics of bulk Ge for the various fields. Compared with simulation results, the results in this work give good agreements in velocity-field curve at low and high fields, while the velocity is a little lower around 1e4 (V/cm) region. The comparison of energy-field curves

(Fig. 5.6(b)) shows the same situation as in bulk Si. At low fields, the energy we got is higher than other studies which are too small on our point of view. At the high fields ours is higher than previous results which also suffers the big discrepancy. Again it should be emphasized that the coupling constant set is not unique. Due to the lack of enough reliable velocity and energy characteristics of SiGe, the coupling constants for SiGe come from the interpolation between the values for Si and Ge. Also we assume the same constants for both strained and unstrained cases. The phonon energies in SiGe are also from the interpolation between Si and Ge.

The impurity and surface roughness scattering in SiGe are treated same as in Si way in the intersest of simplicity. The low-field mobility of holes decreases with the increase of impurity scattering, as shown in Fig. 5.7. It is noted that the simulation results based on Ridley's model agree well with Jacaboni's calculation in low and intermediate doping region, while in high doping region the difference is large. Also the mobility change due to the surface roughness scattering for various effective vertical fields is plotted in Fig. 5.8. Takagi's universal mobility curve is well reproduced by this work.

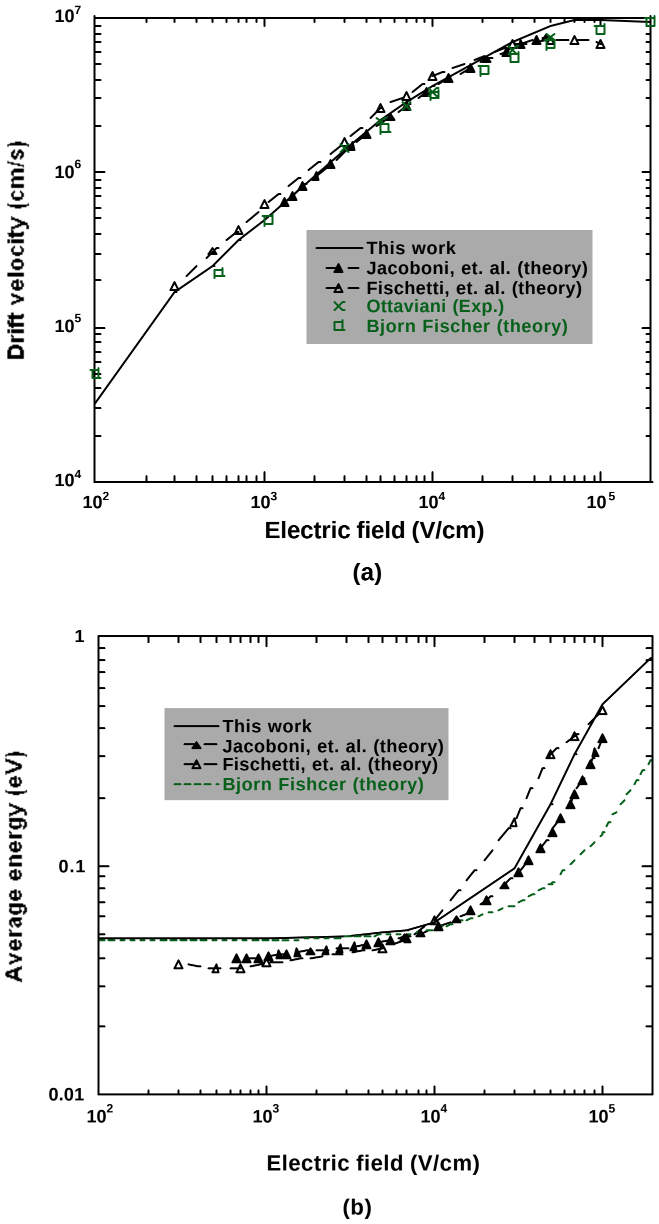

Figure 5.5. (a) Drift velocity of holes in bulk Si as a function of electric field. (b) Average energy of holes in bulk Si as a function of electric field. For comparison, previous measurements and simulation results are also shown.

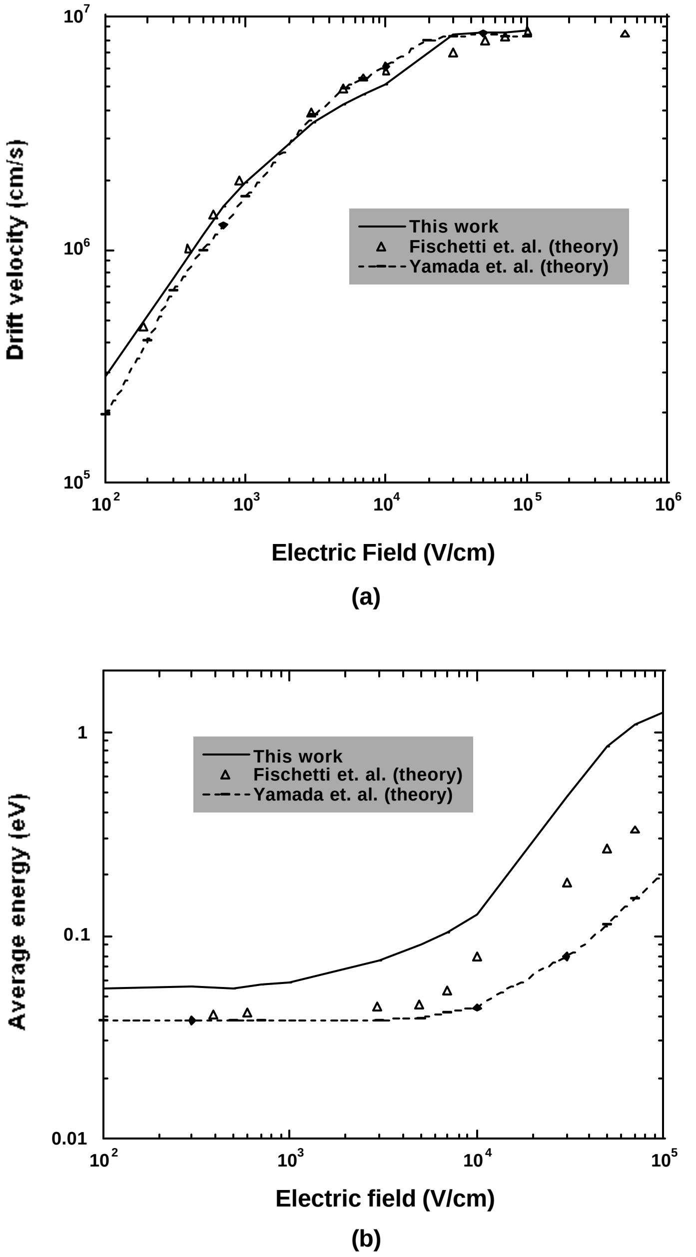

Figure 5.6. (a) Drift velocity of holes in bulk Ge as a function of electric field. (b) Average energy of holes in bulk Ge as a function of electric field. For comparison, previous simulation results are also shown.

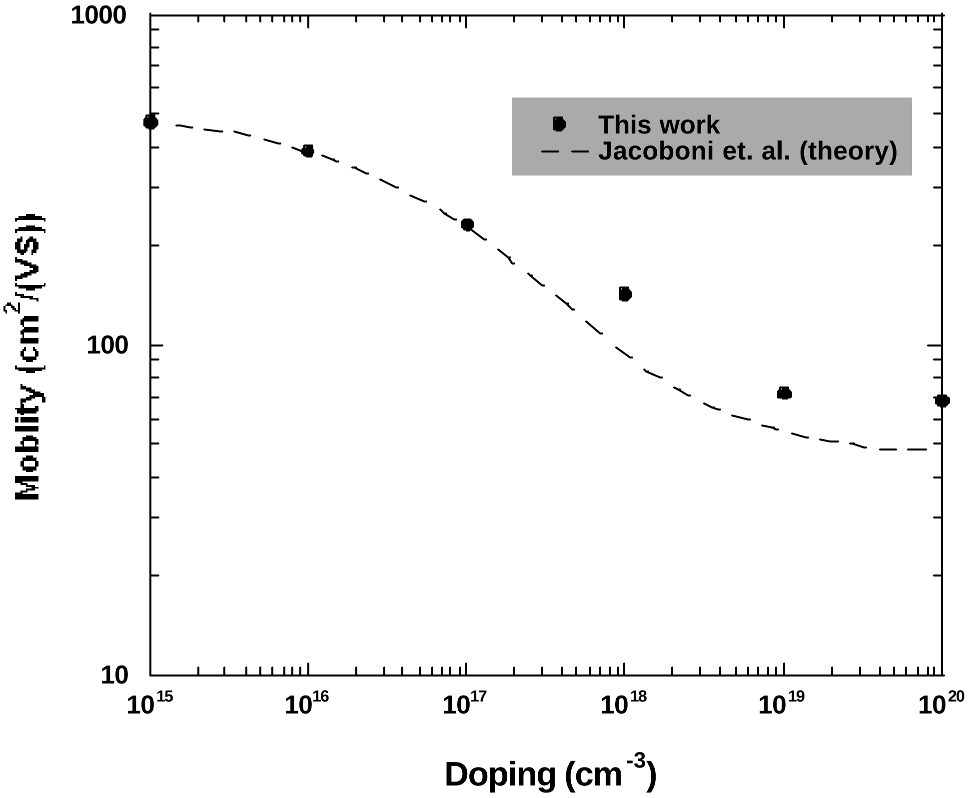

Figure 5.7. Low-field hole mobility in bulk Si versus doping concentration.

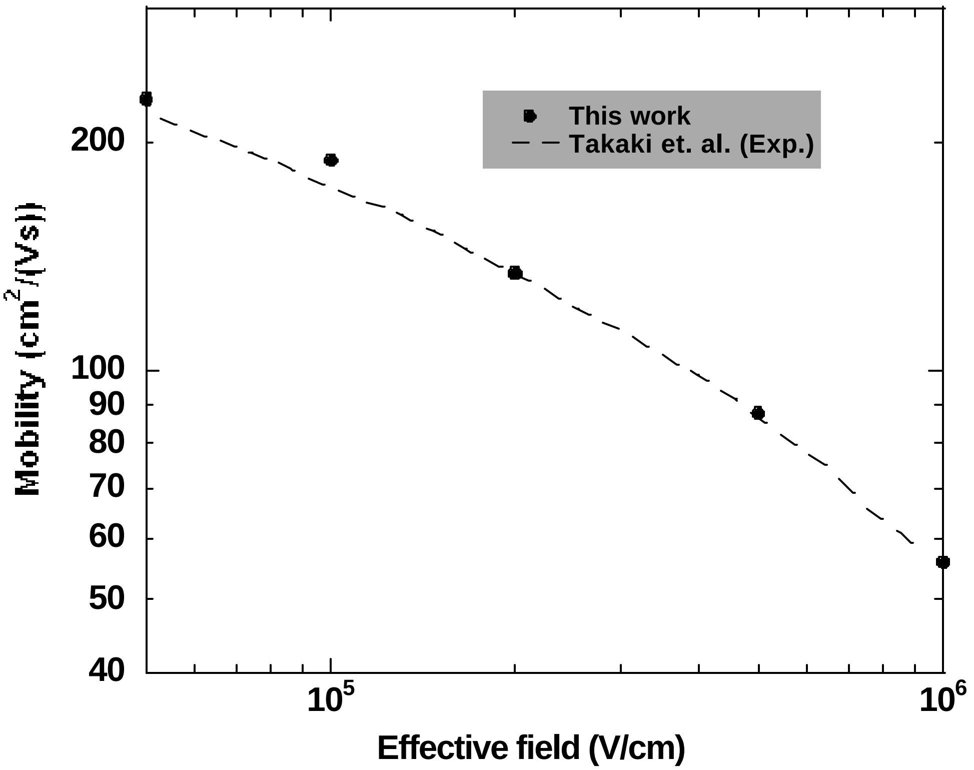

Figure 5.8. Low-field mobility as a function of normal effective field.

5.4 THE SCATTERING RATES

The scattering rates are reduced by the heavy and light-hole band splitting in strained SiGe. Fig. 5.9 show the comparisons of total phonon scattering rates between unstrained Si and strained SiGe with 30% Ge. We show only the first conduction band scattering rates to simplify the plot. The scattering rates of strained SiGe are much lower than those of unstrained Si at low energy region. Fig. 5.10 (a) and (b) show the delicate acoustic and optical phonon scattering rate in energy region below 0.5eV. The strain effect on hole scattering rates are quite simple, which is different from the complicated structure contributed to intervalley scattering in the conduction band in strained Si shown in the last chapter.

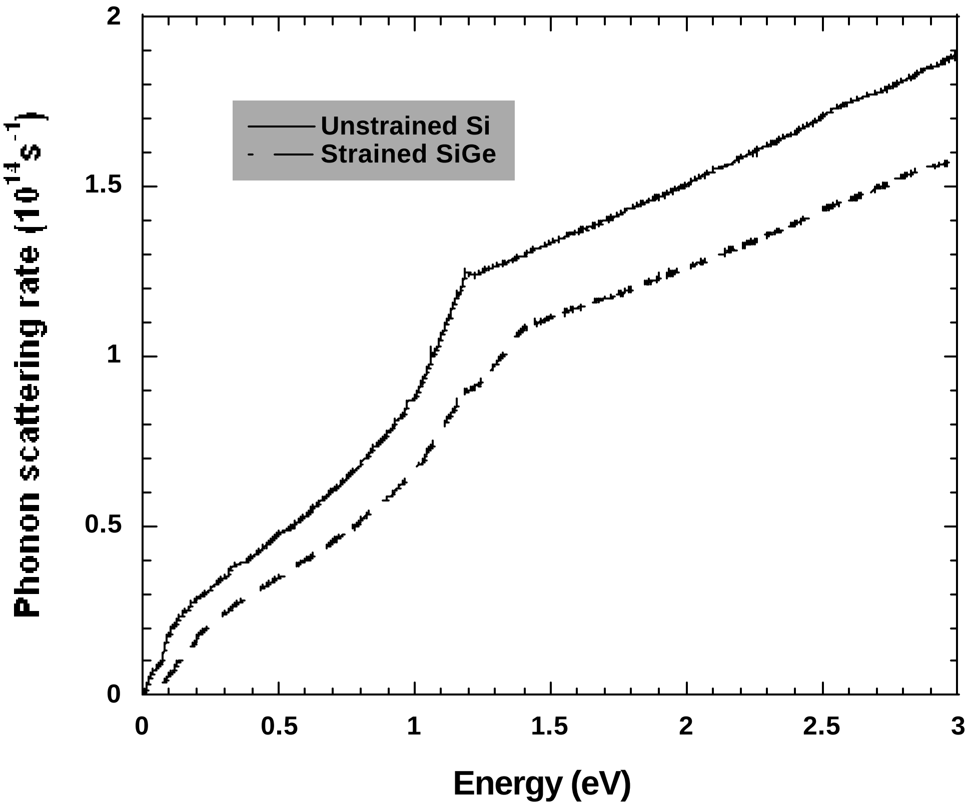

Figure 5.8. Total phonon scattering rates of unstrained Si and CS-$Si_{0.7}Ge_{0.3}$.

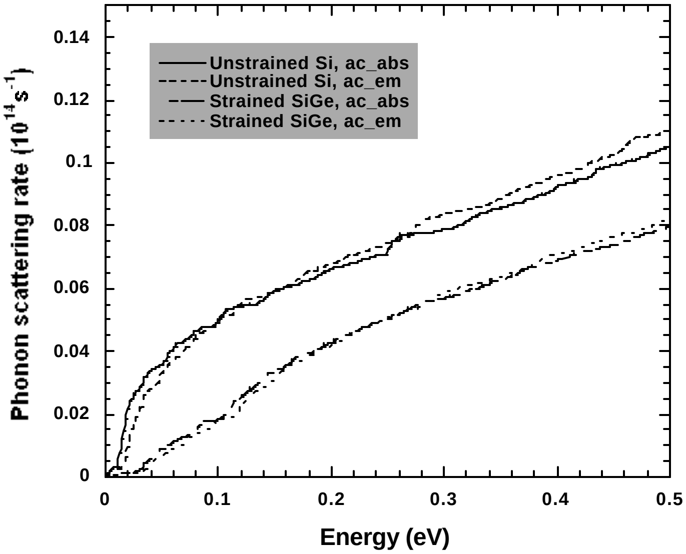

(a)

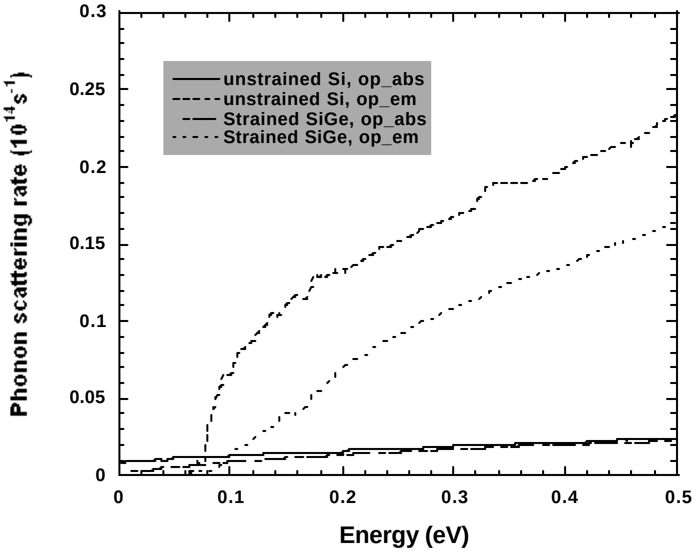

(b)

Figure 5.9. Detailed comparison of phonon scattering between unstrained Si and CS-$Si_{0.7}Ge_{0.3}$ in low energy regimes. (a) Acoustic phonon scattering. (b) Optical phonon scattering.

5.5 TRANSPORT SIMULATION RESULTS

5.5.1 Compressively-strained SiGe

A crucial and uncertain parameter in the treatment of transport in SiGe is the strength of alloy scattering in Harrison and Hauser's model [Har76]. As mentioned in chapter 2, there is big discrepancy in the actual value among previous studies, which suffers from a large scatter of the experimental data and uncertainties regarding the extraction of the drift mobilities from the measurements. In this work we adjust the alloy scattering parameter to fit a new, comprehensive and accurate mobility measurements [Gaw98] in unstrained lightly doped (1e16 cm^{-3}) SiGe at 300K with Ge mole fraction below 13%. Our best fitting, Fig. 5.10, comes from the alloy scattering value at 0.225 eV. The alloy scattering strength we got is smaller compared with previous work mentioned in chapter 2. However it has to be stressed that the actual value depends on not only the measurements it is based on but also the model of band structure and the treatment of phonon scattering. Thus the direct comparison without taking into account experimental data and details of transport treatment is meaningless and not fair.

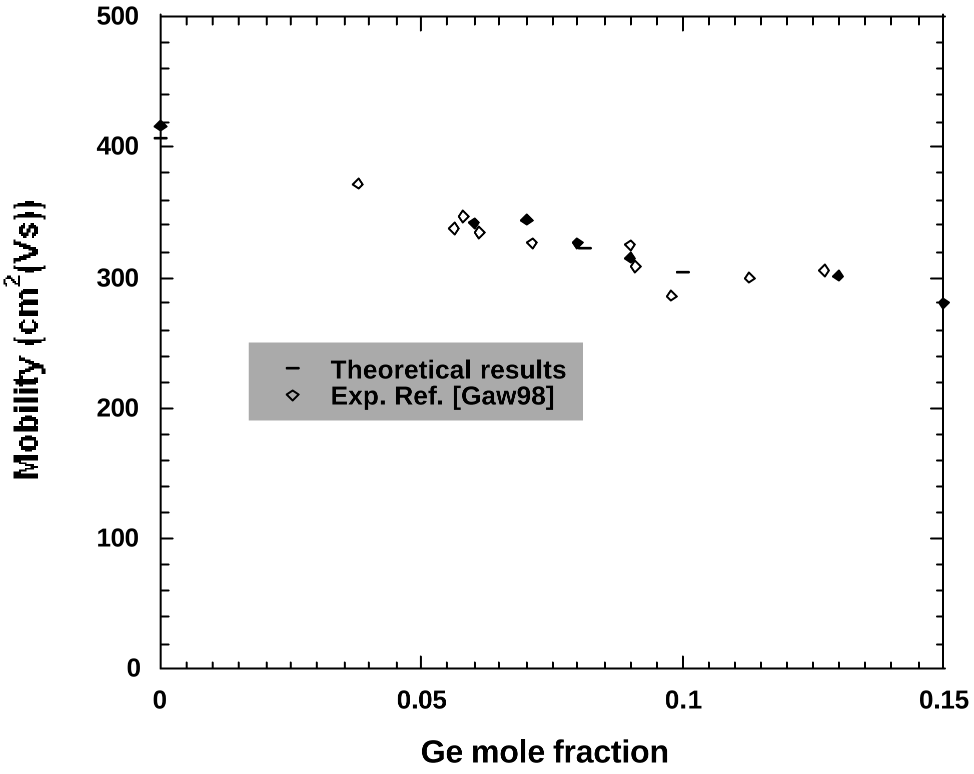

Figure 5.10. Low-field hole mobility as a function of Ge mole fraction in relaxed SiGe alloy with 1e16 cm^{-3} doping.

As we know, the scattering rates in strained SiGe are smaller than those of unstrained Si due to the heavy- and light-hole band splitting. Thus, under the low and intermediate fields drift velocity is enhanced compared with unstrained Si. Fig. 5.11(a) shows the drift velocities of strained $Si_{0.7}Ge_{0.3}$ at 300K without doping. The drift velocity under the [100] field is a little higher than that under [001] field. We also found that the saturation velocity of strained SiGe is reduced compared with unstrained Si, which is also shown in [Buf98]. That is due to the strong alloy scattering and smaller optical phonon energy. The average energy versus field relation is also shown in Fig 5.11(b). Corresponding to the higher drift velocity under the field along [100] and [001] direction, the holes have higher energy.

In strained SiGe strain-induced mobility enhancement and alloy-induced mobility lowering competes each other. The mobility decreases in low Ge mole fraction region (lower than 15%) due to alloy scattering. For highly strained SiGe the mobility enhanced after the strain effect overwhelms the alloy scattering (Fig. 5.12). Also in the strain region we studied, there is no saturation of mobility enhancement.

As in strained Si, the surface roughness scattering degrades the hole mobility. After considering the surface roughness scattering, the mobility (Fig. 5.13) in strained $Si_{0.7}Ge_{0.3}$ is also reduced from the value without taking surface roughness into account. At higher effective field, the lowering is more severe. The effective mobility along [001] direction is even lower than that of unstrained Si. The role of surface roughness in strained SiGe is not very clear in theory and experiment. Also in our treatment we use the parameters from unstrained Si for the sake of simplicity, which is questionable. More comprehensive investigation is needed.

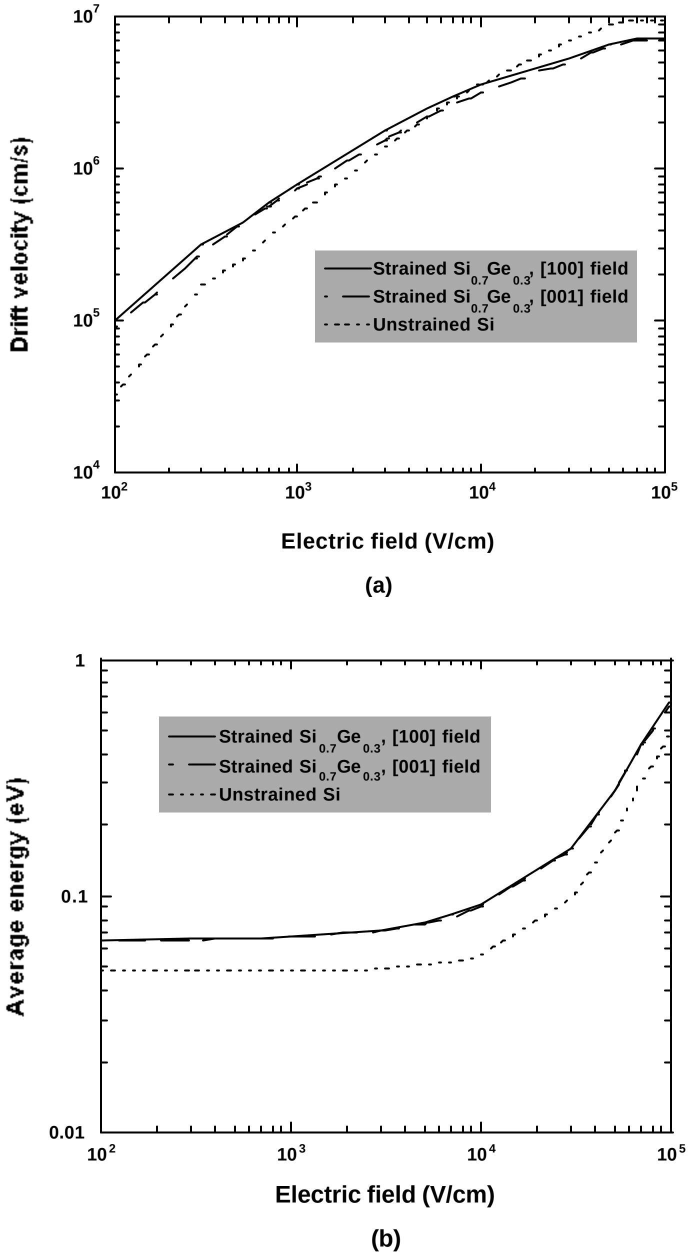

Figure 5.11. (a) Drift velocity of holes in CS-$Si_{0.7}Ge_{0.3}$ as a function of electric field. (b) Average energy of holes in CS-$Si_{0.7}Ge_{0.3}$ as a function of electric field. In CS-$Si_{0.7}Ge_{0.3}$ the results under two oriented fields, [100] and [001], are shown.

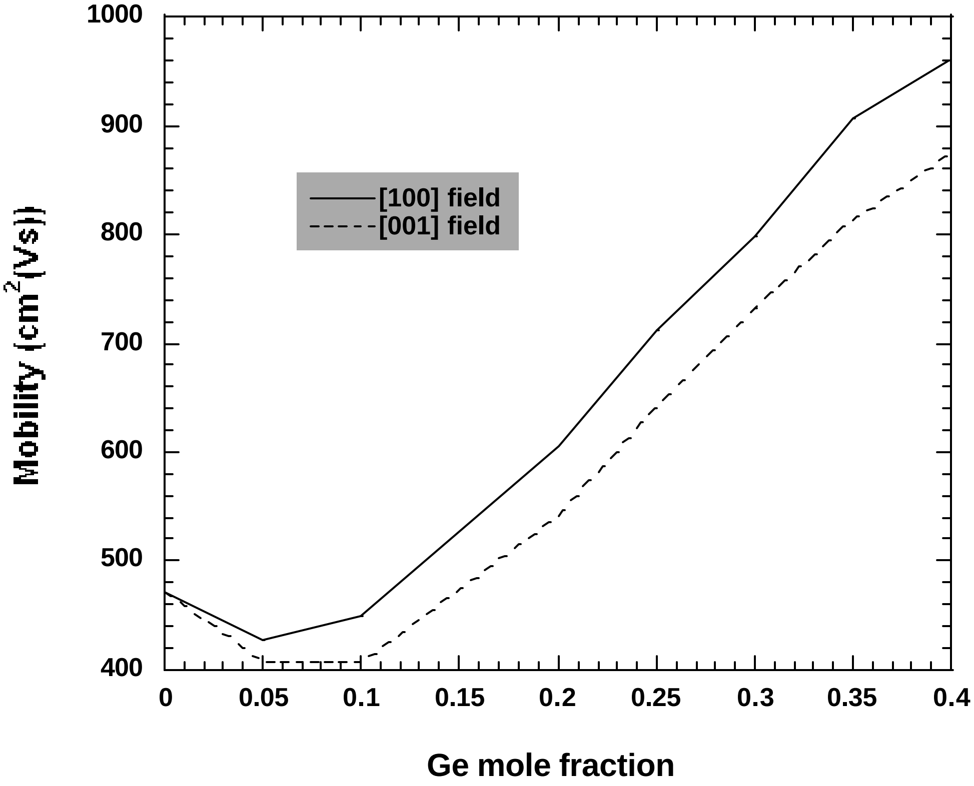

Figure 5.12. The mobility variation with Ge mole fraction in CS-SiGe.

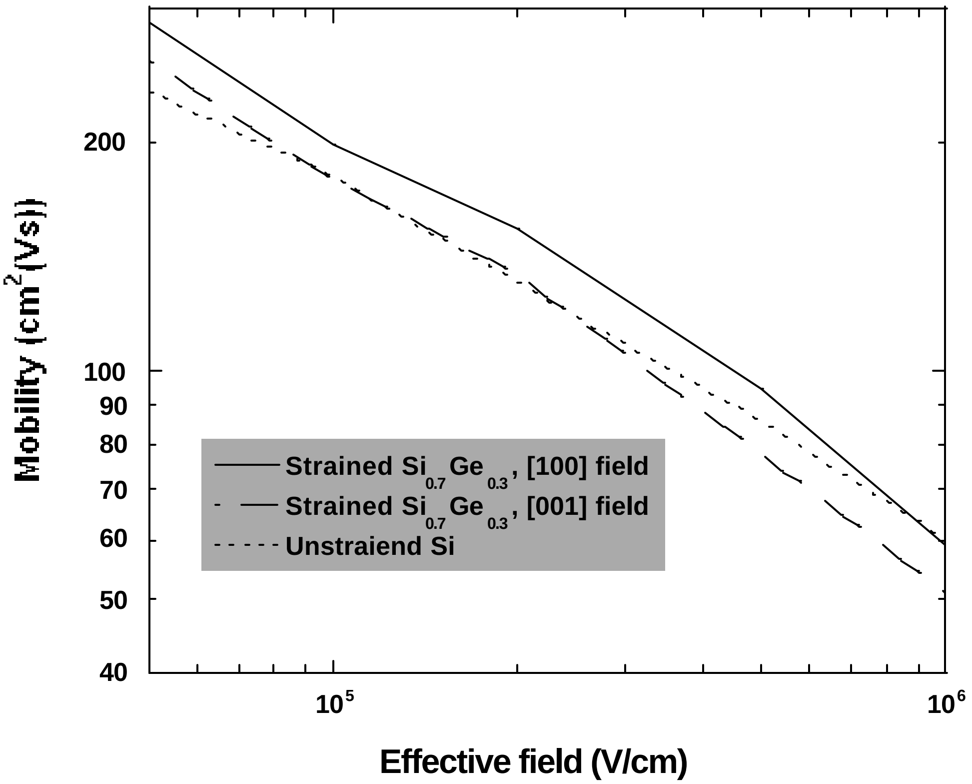

Figure 5.13. Mobility of CS-Si$_{0.7}$Ge$_{0.3}$ under a variety of normal fields. Mobility for fields along [100] and [001] are shown.

5.5.2 50 nm asymmetrical pMOSFET

We applied the multi-material Monte Carlo code to investigate the device performance of a 50nm vertical asymmetrical pMOSFET. The doping profile in the device is asymmetric which can be easily achieved in vertical MOSFETs. The doping profiles along Si/SiO$_2$ interface and poly gate are shown in Fig. 5.14. The high doping concentration on source side is to reduce the short channel effects and off-state leakage current [Yu97]. The low doping profile on the drain side is to reduce the impurity scattering and increase the drive current correspondingly. In the simulation, the gate and substrate are Si, and we explore several material combinations in the source, drain and channel: Si/$Si_{0.7}Ge_{0.3}$ heterojunction at different positions and graded SiGe channel. The details of devices we studied are listed in Table 5.1. And the corresponding valence band edge variations for those devices are plotted in Fig. 5.15. In this work we did preliminary simulation of these devices. We found these devices are quite complicated and interesting. We emphasize that it needs more comprehensive work to obtain conclusive and reliable results. Here we employ these devices as the application of our multi-material MC simulation code. The results here may be questionable.

Device code	Material profile in channel	V_t (V)
Unstrained Si	unstrained Si	0.294
CS-$Si_{0.7}Ge_{0.3}$	CS-$Si_{0.7}Ge_{0.3}$	0.694
Si/$Si_{0.7}Ge_{0.3}$-S	Si/$Si_{0.7}Ge_{0.3}$ with heterojunction in source at 0.788 μm	0.959
Si/$Si_{0.7}Ge_{0.3}$-C	Si/$Si_{0.7}Ge_{0.3}$ with heterojunction in channel at 0.851 μm	0.086
Si/$Si_{0.7}Ge_{0.3}$-C-st	Graded SiGe channel (with 2kT band edge step) starting from 0.851 μm and the maximum Ge mole fraction is 30%	0.341
Si/$Si_{0.7}Ge_{0.3}$-C-lin	Linearly graded SiGe channel starting from 0.851 μm and the maximum Ge mole fraction is 30%	0.077

Table 5.1. The material profiles and threshold voltages of the devices studied in the work.

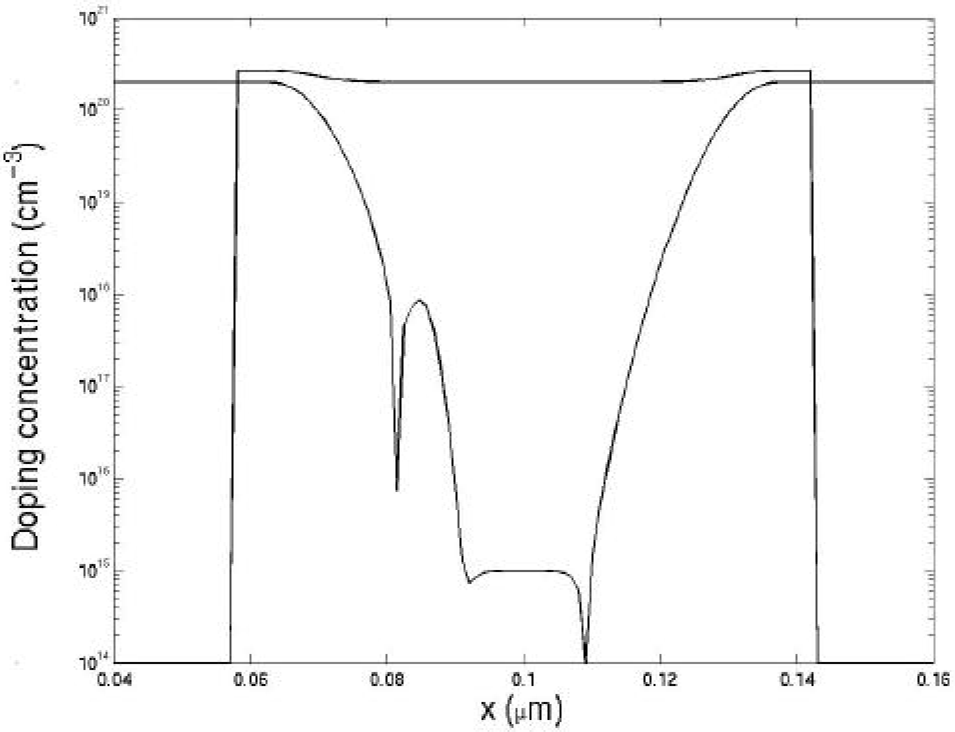

Figure 5.14. The doping profiles along channel/oxide interface and polygate of asymmetrical pMOSFET.

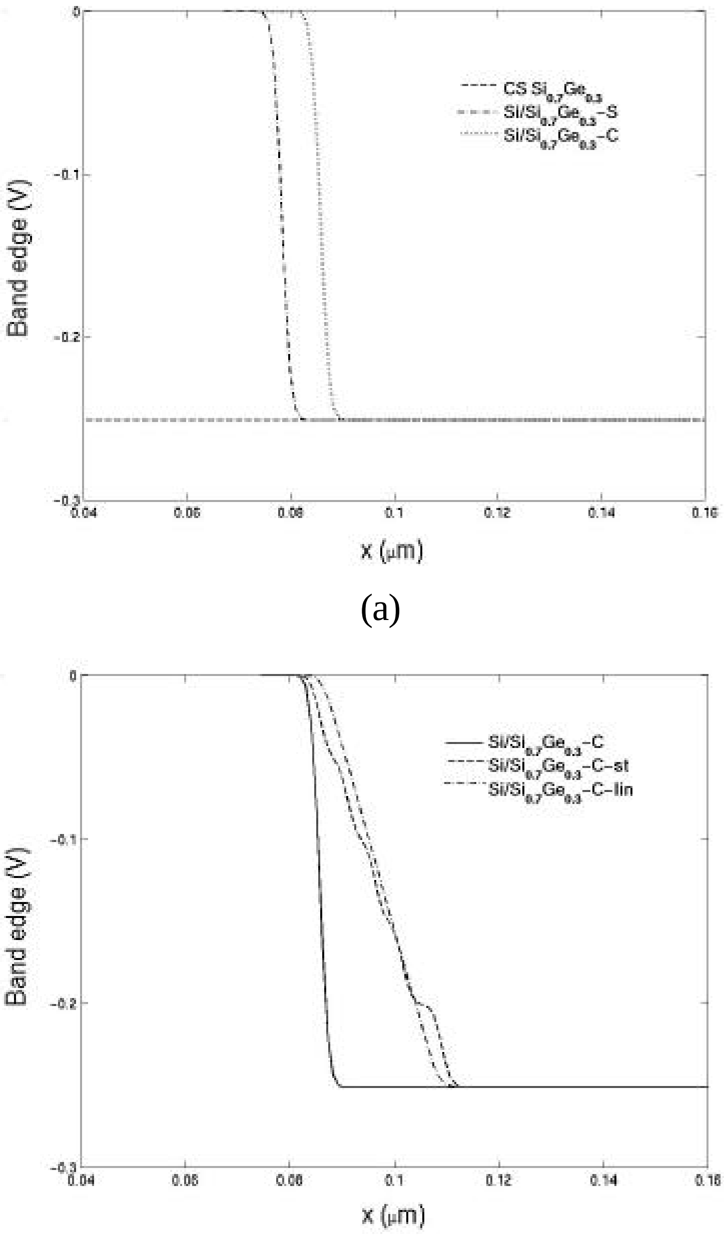

(a)

(b)

Figure 5.15. The valence band edges variation: (a) CS-$Si_{0.7}Ge_{0.3}$, Si/$Si_{0.7}Ge_{0.3}$-S and Si/$Si_{0.7}Ge_{0.3}$-C; (b) Si/$Si_{0.7}Ge_{0.3}$-C, Si/$Si_{0.7}Ge_{0.3}$-C-st and Si/$Si_{0.7}Ge_{0.3}$-C-lin.

In order to make a fair comparison among these devices, we first study their threshold voltages. We calculate the drain currents of these devices with low drain bias (-0.3V), and extrapolate the currents of various gate biases to obtain the threshold voltages. Fig. 5.16 shows the drain currents of these devices with V_d=-0.3V and various gate bias. The extrapolated threshold voltages V_t are listed in Table 5.1. We found the devices with source junction covered by SiGe (CS-$Si_{0.7}Ge_{0.3}$ and Si/$Si_{0.7}Ge_{0.3}$-S) have higher (more positive) V_t. That is caused by the lower valence band edge in channel at source junction, which induced 0.24 V (Fig. 2.4) in flat band. In Si/$Si_{0.7}Ge_{0.3}$-C the source junction is still covered by Si without band offset at that position between source and polygate, although it has $Si_{0.7}Ge_{0.3}$ channel; so the V_t is lower. The comparison of V_t in Si/$Si_{0.7}Ge_{0.3}$-C serial shows no conclusive trend. Also the uncertainty of extraction of V_t is quite large. V_t may change depending on the V_g chosen for extrapolation. The consistency and reliability of the extrapolation needs on further study.

Based on the V_t of these devices, we simulate the drain current in on state (V_d =-1.0V and V_g-V_t =-1.0V). The results are shown in Fig 5.17. The devices can be classified into two categories convenient for comparison. The first category includes the devices with single material in the channel: unstrained Si and CS-$Si_{0.7}Ge_{0.3}$ and with two materials and a single heterojunction: Si/$Si_{0.7}Ge_{0.3}$-S and Si/$Si_{0.7}Ge_{0.3}$-C. The devices in second group have a Si/SiGe heterojunction starting at the same point in the channel and maximum Ge mole fraction in SiGe but a variety of Ge mole fraction distributions along the channel.

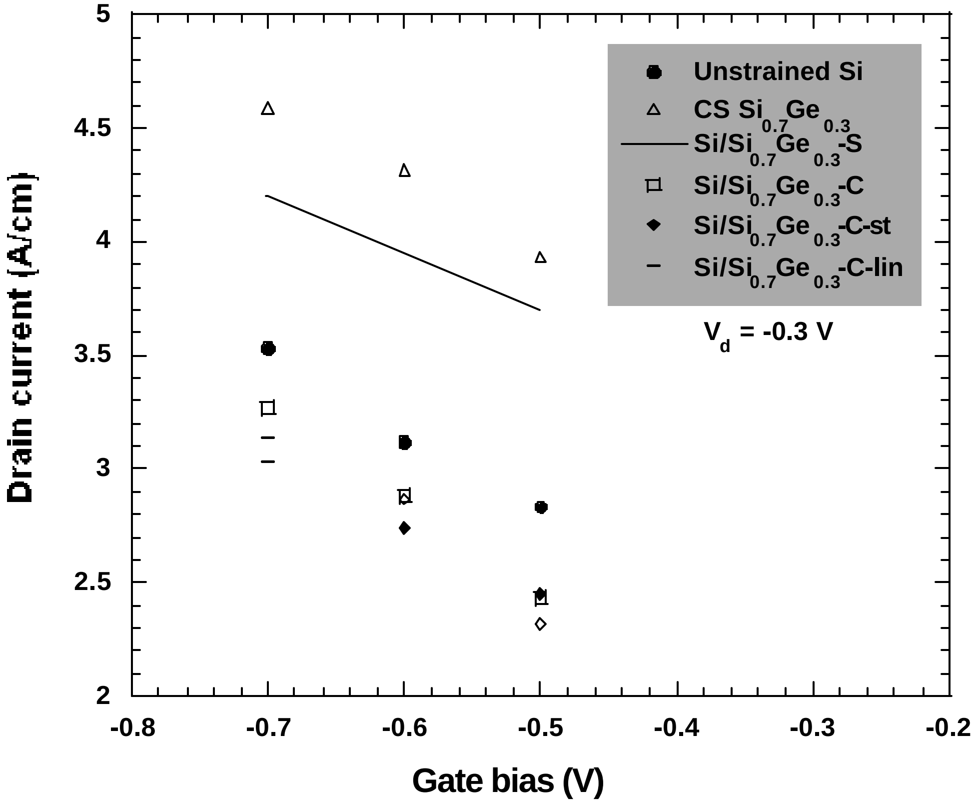

Figure 5.16. The drain currents of a variety of devices with V_d=-0.3V and various gate biases.

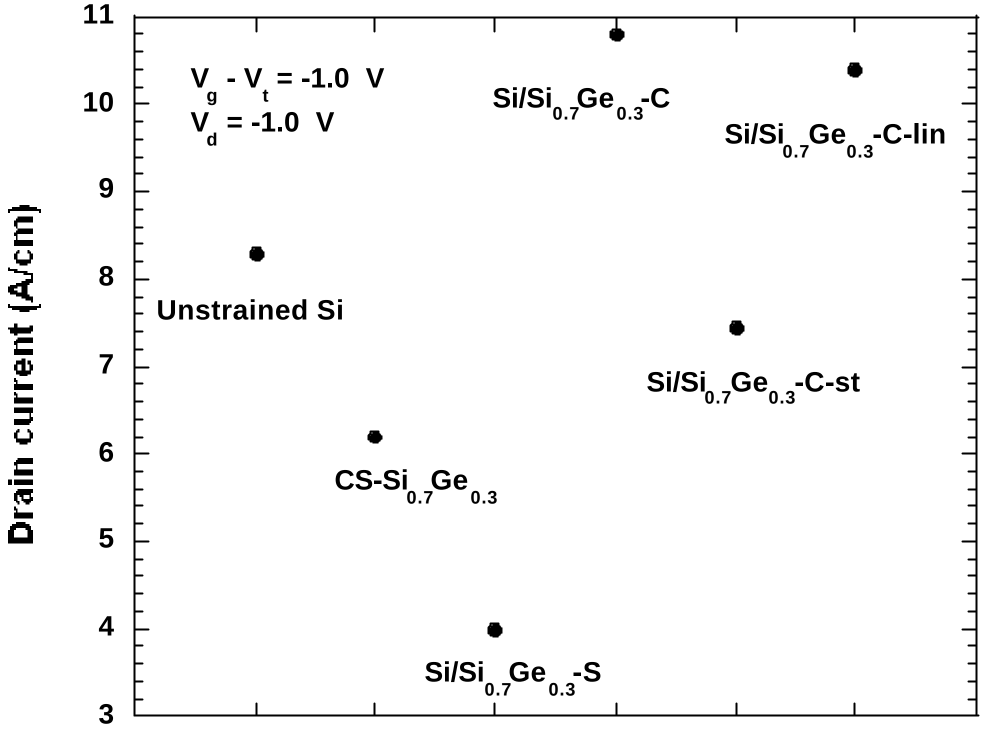

Figure 5.17. The drive current of the investigated devices at V_d = 1.0V and V_g-V_t=-1.0V.

In Fig. 5.18 we found the source barrier of Si/$Si_{0.7}Ge_{0.3}$-C is much lower than other devices in this group, which induces highest carrier concentration (Fig. 5.19) in channel. Also a velocity peak at the heterojunction is easily recognized in Fig 5.20. Although the average velocity at the rest of channel is the lowest in this group, the drain current is still the highest due to the high carrier concentration. The high barrier at the source junction of Si/$Si_{0.7}Ge_{0.3}$-S makes the lowest hole concentration in the channel. So this device has lowest drive current. The other interesting comparison is made between unstrained Si and CS-$Si_{0.7}Ge_{0.3}$. Fig. 5.18

shows the higher source barrier in CS-$Si_{0.7}Ge_{0.3}$ that causes lower hole concentration in channel. Also we found the average velocity is lower than that of unstrained Si device, which is in consistent with the lower effective mobility in high normal field region (Fig. 5.13) and lower high-field velocity in CS-SiGe (Fig. 5.11). Thus, in that design the CS-$Si_{0.7}Ge_{0.3}$ has lower drain current.

Among the devices in the second category, the Si/$Si_{0.7}Ge_{0.3}$-C and Si/$Si_{0.7}Ge_{0.3}$-C-lin has the same barrier height in the source region (Fig. 5.21) that induces the same hole concentration in the channel (Fig. 5.22). The high velocity peak (Fig. 5.23) at the heterojunction in Si/$Si_{0.7}Ge_{0.3}$-C makes higher velocity injection than in Si/$Si_{0.7}Ge_{0.3}$-C-lin and corresponding higher drive current, although the average velocity is lower in the rest of channel induced by lower lateral field. The device with step-like low-energy band offsets, Si/$Si_{0.7}Ge_{0.3}$-C-st, has higher barrier in source region. So it has the lowest hole concentration in this category and lowest drive current.

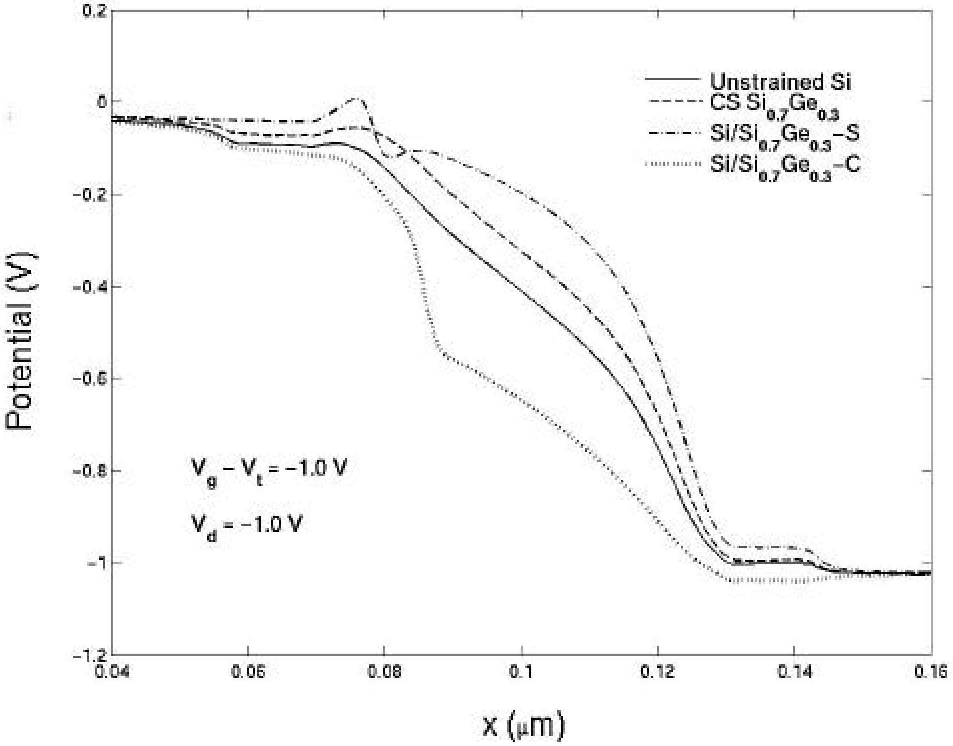

Figure 5.18. Electrostatic potentials at channel and oxide interface along channel direction with V_g-V_t=-1.0V and V_d=-1.0V.

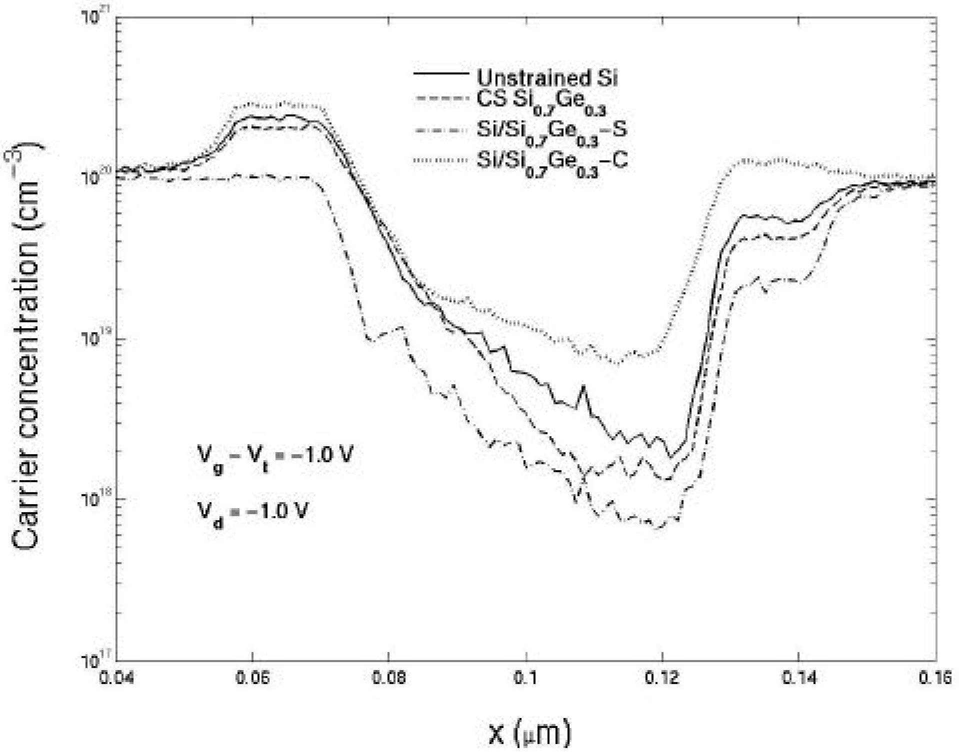

Figure 5.19. Carrier concentrations at channel and oxide interface along channel direction with V_g-V_t=-1.0V and V_d=-1.0V.

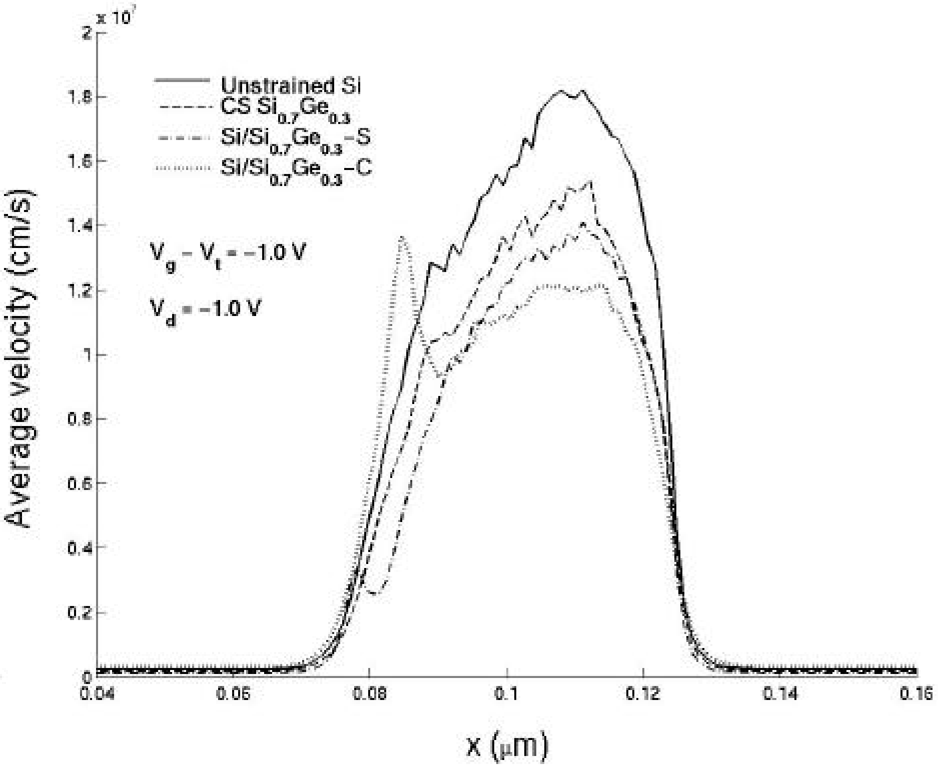

Figure 5.20. Average velocities along channel direction with V_g-V_t=-1.0V and V_d=-1.0V.

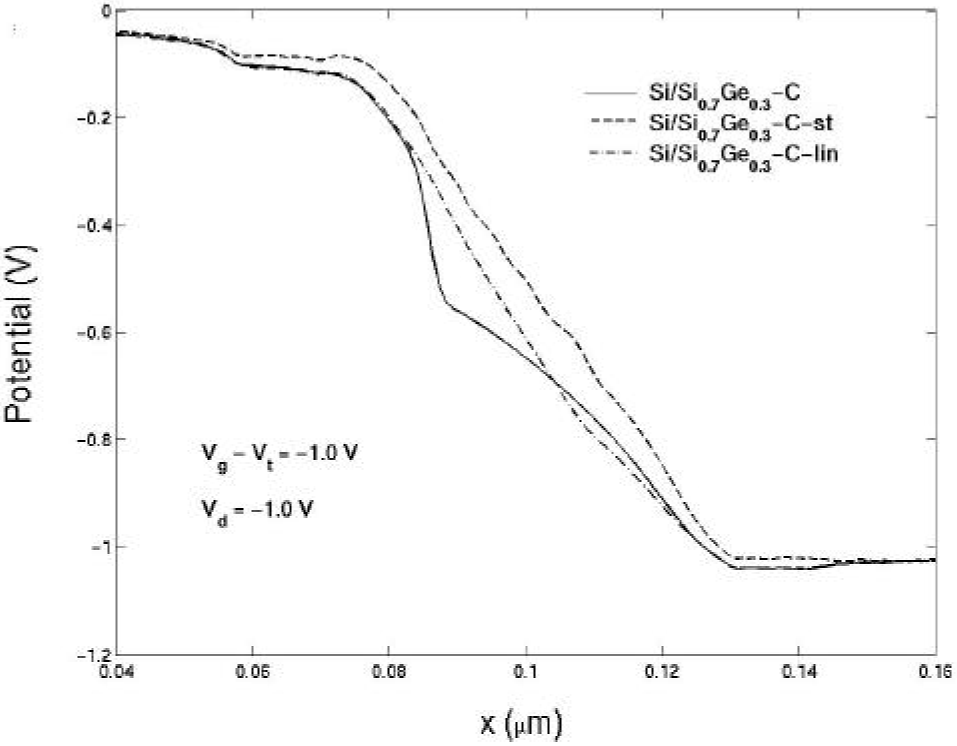

Figure 5.21. Electrostatic potentials at channel and oxide interface along channel direction with V_g-V_t=-1.0V and V_d=-1.0V.

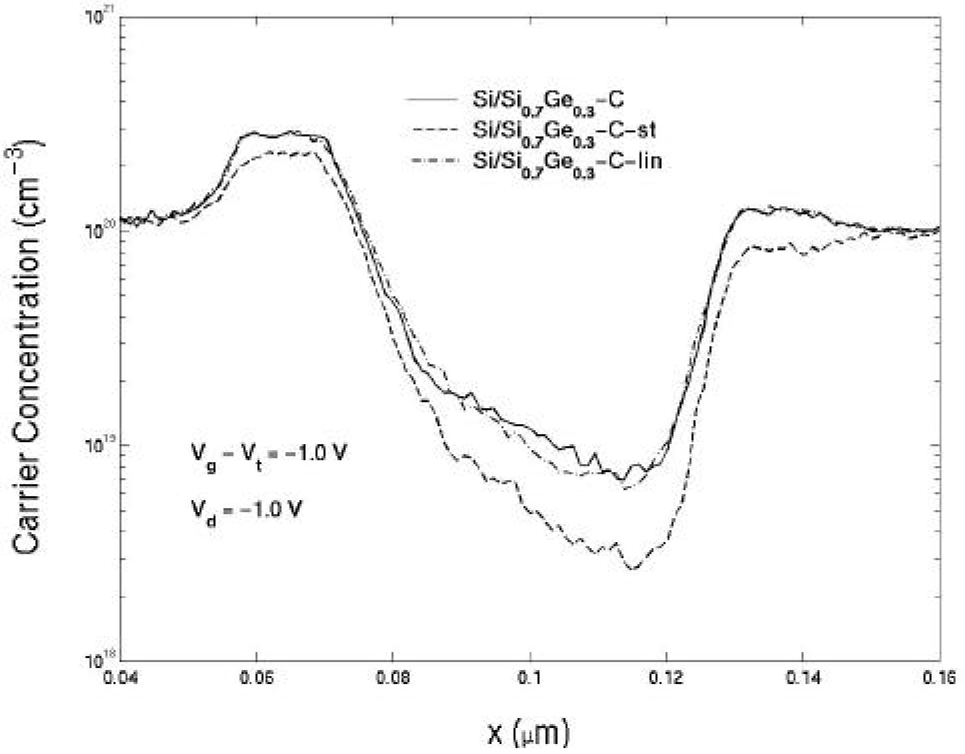

Figure 5.22. Carrier concentrations at channel and oxide interface along channel direction with V_g-V_t=-1.0V and V_d=-1.0V.

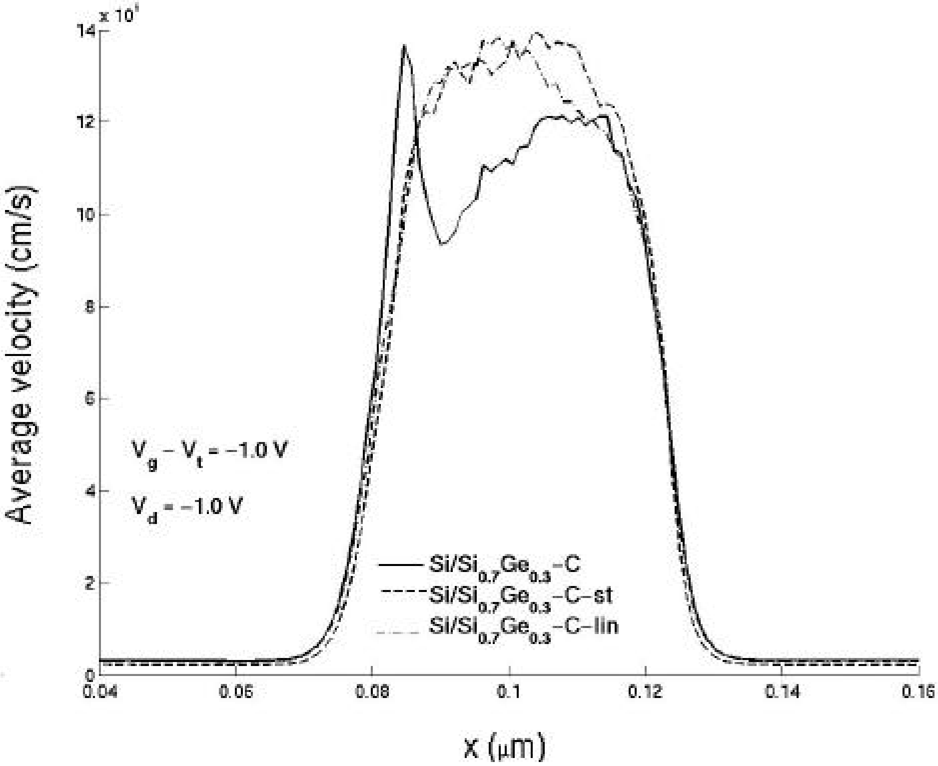

Figure 5.23. Integrated average velocities along channel direction with V_g-V_t=-1.0V and V_d=-1.0V.

CHAPTER SIX

Conclusions and Recommendations

6.1 CONCLUSIONS

A new full-band multi-material Si-based Monte Carlo simulation code has been developed to deep submicron Si-based heterostructure devices. The tool has high flexibility and generality on material type and profiles in the devices. The code provides the simulation ability for both electron and hole. The transport and phonon scattering treatment are full band. The code has been calibrated using unstrained Si data. Also it provides a good framework for further modification and development.

We employ the full-band Monte Carlo simulation tool to investigate the material properties of orthorhombic strained Si. It provides higher low-field mobility compared with bulk Si. Also this material can be easily fabricated with high quality compared with conventional strained Si grown on relaxed SiGe alloy. Material properties of conventional tensilely-strained (TS) Si and compressively-strained (CS) SiGe have been investigated with Monte Carlo simulation. TS Si and CS-SiGe demonstrate higher low-field mobility for electrons and holes, respectively. In device simulations preliminary work has been done on TS Si nMOSFETs and pMOSFET with Si/CS-SiGe heterojunction. nMOSFET with TS-Si as channel shows higher drain current than a Si device. The pMOSFET with Si/CS-SiGe heterostructure shows interesting but complicated phenomena. Further investigation and clarification are needed.

6.2 RECOMMENDATIONS

6.2.1 Code developments

The scattering table used in current version of Monte Carlo code is energy dependent. Strictly speaking it should be momentum dependent, although we prove that the approximation is still valid in strained material. For the sake of be greater accuracy, the scattering rate can be modified to momentum dependent. Also some of the scattering mechanisms, e.g. impurity scattering, are still analytical. It can be modified to full-band style to make the code completely full band. The scattering treatments can be further calibrated with data. Further carrier-carrier scattering should be implemented for future applications to dramatically scaled devices.

The current treatment of quantum confinement in the inversion layer is calibrated for electron transport in bulk Si only. The hole version is needed and the quantum confinement effect on scattering in that layer should also be take into account. Tunneling through heterojunctions is treated by Feynman's "effective potential" approach. The best one should be transfer matrix method, but it requires too much computation time. Effective potential method needs further calibration and test based on the transfer matrix method.

The contact treatment in hole simulation in current version is still not satisfactory. There is always around 40meV potential drop at the boundary of contact and semiconductor. The reason for that is not clear. More work is needed on that aspect.

6.2.2 Device simulation

In this work we did some preliminary work on device simulation of strained Si and strained SiGe device to demonstrate the capability of the code. More work is needed on these kinds of devices. For strained Si nMOSFET a threshold voltage study is needed to make a fair comparison with bulk Si devices. Also there are already lot of experimental data on these kinds of devices. So the comparison and calibration (specifically the surface roughness scattering in strained Si devices) can be done. For strained SiGe devices the role of surface roughness scattering, extraction of threshold voltage and threshold voltage change with SiGe devices, especially devices with Si/SiGe heterojunction, should be clarified in the future. Finally device optimization can be done with the current code.

Bibliography

[Ant99] D. Antoniads, I. Djomehri, K. Jackson, and S. Miller, Well-tempered bulk-Si NMOSFET device, Aug. 1999, http://www-mtl.mit.edu/Well/.

[Bac82] G. B. Bachelet, D. R. Hamann, and M. Schlüter, "Pseudopotentials that work," *Phys. Rev*. **B** 26, p. 4199, 1982.

[Bal65] I. Balsiev, "Influence of uniaxial stressSemi-metals on the indirect absorption edge in silicon and germanium," *Phys. Rev*. vol. 143, p. 636, 1965.

[Bec92] F. Bechstedt, R. Del Sole, G. Cappellini, and L. Reining, "An efficient method for calculating quasiparticle energies in semiconductors," *Solid State Comm*. Vol. 84, p. 765, 1992.

[Bea84] J. C. Bean, L. C. Feldman, A. T. Fiory, S. Nakahara, and I. K. Robinson, "Ge_xSi_{1-x}/Si strained-layer superlattice grown by molecular beam epitaxy," *J. Vac. Sci. Technol*. **A**2, p. 436, 1984.

[Bjo99] D. Bjorn Fisher, "A full-band Monte Carlo charge transport model for nanoscale silicon devices including strain", *Ph.D dissertation*, 1999.

[Boc95] N. Moll, M. Bockstedte, M. Fuchs, E. Pehlke, and M. Scheffler, "Application of generalized gradient approximations," *Phys. Rev*. **B** 52, p. 2550, 1995.

[Boc97] M. Bockstedte, A. Kley, and M. Scheffler, "Density-functional theory calculations for poly-atomic systems," *Comp. Phys. Comm*. Vol. 107, p. 187, 1997.

[Bra58] R. Braunstein, A. R. Moore, and F. Herman, "Intrinsic optical absorption in Germanium-Silicon alloys," *Phys. Rev*., vol. 109, p. 695, 1958.

[Bro51] H. Brooks and C. Herring, "Scattering by ionized impurities in semiconductors," *Phys. Rev*. Vol. 83, p. 879, 1951.

[Bru89] R. Brunetti. C. Jacoboni, F. Venture, E. Sangirogi, and B. Ricco, "A many-band silicon model for hot-electron transport at high energies," *Solid-State Electron*. Vol. 32, p. 1663, 1989.

[Bud92] J. Bude and K. Hess, "Thresholds of impact ionization in semiconductors," *J. Appl. Phys*. Vol. 72, p. 3554, 1992.

[Buf98] F. M. Bufler and B. Meinerzhagen, "Hole transport in strained $Si_{1-x}Ge_x$ alloys on $Si_{1-y}Ge_y$ substrates," *J. Appl. Phys*. Vol. 84, p. 5597, 1998.

[Bur95] J. Burchhardt, M. M. Nielsen, D. L. Adams, E. Lundgren, J. N. Andersen, C. Stampfl, M. Scheffler, A. Schmalz, S. Aminpirooz, and J. Haase, "Formation and structural analysis of a surface alloy," *Phys. Rev. Lett*. Vol. 74, p. 1617, 1995.

[Bus60] G. Bush and O. Vogt, Helv. Phys. Acta Vol. 33, p. 437, 1960.

[Can75] C. Canali, C. Jacoboni, F. Nava, G. Ottaviani, and A. Alberigi-Quaranta, "Hole drift velocity in silicon," *Phys. Rev*. **B** 12, p. 2265, 1975.

[Car93] E. Cartier, M. V. Fischetti, E. A. Eklund, and F. R. McFeely, "Impact ionization in silicon," *Appl. Phys. Lett*. Vol. 62, p. 3339, 1993.

[Cep80] D. M. Ceperley and B. J. Alder, "Ground state of the electron gas by a stochastic method," *Phys. Rev. Lett*. Vol. 45, p. 567, 1980.

[Che76] J. R. Chelikowsky and M. L. Cohen, "Nonlocal pseudopotential calculations for the electronic structure of eleven diamond and zinc-blend semiconductors," *Phys. Rev*. **B** 14, p. 556, 1976.

[Che80] A. B. Chen and A. Sher, "Electronic structure of III-V semiconductors and alloys using simple orbitals," *Phys. Rev*. **B** 22, p. 3886, 1980.

[Fel87] L. C. Feldman, J. Bevk, B. A. Davidson, H. J. Gossman, and J. P. Mannaerts, "Strain in ultrathin epitaxial films of Ge/Si (100) measured by ion scattering and channeling," *Phys. Rev. Lett*. Vol. 59, p. 664, 1987.

[Fey65] R. P. Feynman and A. R. Hibbs, "Quantum mechanics and path integrals," New York: McGraw-Hill, 1965.

[Fis88] M. V. Fischetti and S. Laux, "Monte Carlo analysis of electron transport in small semiconductor devices including band-structure and space-charge effects," *Phys. Rev*. **B** 38, p. 9721, 1988.

[Fis96] M. V. Fischetti and S. E. Laux, "Band structure, deformation potentials, and carrier mobility in strained Si, Ge and SiGe alloys," J. Appl. Phys. Vol. 80, p. 2234, 1996.

[Fri89] P. Friedel, M. S. Hybertsen, and M. Schluter, "Local empirical pseudopotential approach to the optical properties of Si/Ge superlattices," *Phys. Rev*. **B** 39, p. 7974, 1989.

[Gar91] P. M. Garone, V. Venkataraman, and J. C. Sturm, "Mobility enhancement and quantum mechanical modeling in $Si_{1-x}Ge_x$ channel MOSFET from 90 to 300 K," *IEDM Tech. Dig*. p. 21, 1991.

[Gaw98] P. Gaworzewski, K. Tittelbach-helmrich, U. Penner, and N. V. Abrosimov, "Electrical properties of lightly doped p-type silicon-germanium single crystals", J. Apply. Phys. Vol. 83, p. 5258, 1998.

[Gli58] M. Glicksman, Phys. Rev. Vol. 111, p. 125, 1958.

[Gre86] D. W. Greve, "Growth of epitaxial germanium-silicon heterostructures by chemical vapor deposition," *Material Science and Engineering*, **B**18, p. 22, 1993.

[God88] R. W. Godby, M. Schlüter, and L. J. Sham, "Self-energy operators and exchange-correlation potentials in semiconductors," *Phys. Rev*. **B** 37, p. 10159, 1988.

[Ham89] D. R. Hamann, "Generalized norm-conserving pseudopotentials," *Phys. Rev*. **B** 40, p. 2980, 1989.

[Har76] J. W. Harrison and J. R. Hauser, "Alloy scattering in ternary III-V compounds," Phys. Rev. B 13, p. 5347, 1976.

[Has63] H. Hasegawa, "Theory of cyclotron resonance in strained silicon crystals," *Phys. Rev*. vol. 129, p. 1029, 1963.

[Hed69] L. Hedin and S. Lundqvist, *Solid State Physics* , edited by H. Ehrenreich, F. Seitz, and D. Turnbull (Academic, New York, 1969), Vol. 23, p. 1.

[Hoh64] H. Hohenberg and W. Kohn, "Inhomogeneous electron gas," *Phys. Rev*. vol. 136, p. B864, 1964.

[Ism93] K. Ismail, S. Nelson, J. Chu, and B. Meyerson, "Electron transport properties of Si/SiGe heterostructures: measurements and device implications," *Appl. Phys. Lett.*, vol. 63, no. 5, p. 660, 1993.

[Ism94] K. Ismail, J. Chu, and B. Meyerson, "High hole mobility in SiGe alloy for device applications," *Appl. Phys. Lett.*, vol. 64, no. 5, p. 3124, 1994.

[Jac77] C. Jacoboni, C. Canali, G. Ottaviani, and A.A. Quaranta, "Review of some charge transport properties of Silicon," Solid State Electronics, Vol. 20, p. 77, 1977.

[Jac79] C. Jacoboni and L. Reggiani, "Bulk hot-electron properties of cubic semiconductors," *Ad. Phys*. Vol. 28, p. 493, 1979.

[Jac83] C. Jacoboni and L. Reggiani, "The Monte Carlo method for the solution of charge transport in semiconductors with applications to covalent materials," *Rev. of Mod. Phys*. Vol. 55, p. 645, 1983.

[Jal96] S. Jallepalli, "Monte Carlo based analysis of carrier transport in deep submicro silicon MOSFETs", *Ph.D. dissertation*, 1996.

[Kac94] P. Käckell, B. Wenzien, and F. Bechstedt, "Electronic properties of cubic and hexagonal SiC polytypes from *ab initio* calculations," *Phys. Rev*. **B** 50, p. 10761, 1994.

[Kan67] E. O. Kane, "Electron scattering by pair production in silicon," *Phys. Re*v. Vol. 159, p. 624, 1967.

[Kel60] L. V. Keldysh, "Concerning the theory of impact ionization in semiconductors," *Zh. Eksp. Teor. Fiz*. Vol. 37, p. 713, 1960. [*Sov. Phys. JETP* Vol. 10, p. 509,1960].

[Kel89] P. C. Kelires and J. Tersoff, "Equilibrium alloy properties by direct simulation," *Phys. Rev. Lett*, Vol. 63, p. 1164, 1989.

[Kle82] L. Kleinman and D. M. Bylander, "Efficacious form for model pseudopotentials," *Phys. Rev. Lett*. Vol. 48, p. 1425, 1982.

[Koh65] W. Kohn and L. J. Sham, "Inhomogeneous electron gas," *Phys. Rev*. Vol. 140, p. A1133, 1965.

[Kos57] G. F. Koster, in *Solid State Physics*, edited by F. Seitz and D. Turnbull (Academic, New York, 1957), Vol. 5, p. 173.

[Kun96] T. Kunikiyo, M. Takenaka, *et al*., "A model of impact ionization due to the primary hole in silicon for a full band Monte Carlo simulation," *J. Appl. Phys.* Vol. 79, p. 7718, 1996.

[Liu99] K. C. Liu, X. Wang, E. Quinones, X. Chen, X. D. Chen, D. L. Kencke, B. Anantharam, R. D. Chang, S. K. Ray, S. K. Oswal, C. Y. Tu, and S. K. Banerjee, "novel sidewall strained-Si channel nMOSFET," IEEE *IEDM Tech. Dig.*, p. 63, 1999.

[Lun97] M. Lundstrom, "Elementary scattering theory of the Si MOSFET," IEEE Elec. Dev. Lett., Vol. 18, no. 7, p. 361, 1997.

[Maj87] J. A. Majewski and P. Vogl, 'Simple model for structural properties and crystal stability of *sp*-bonded solids," *Phys. Rev.* **B** 35, p. 9666, 1987.

[Man92] T. Manku and A. Nathan, "Electron-drift mobility model for devices based on unstrained and coherently strained $Si_{1-x}Ge_x$ grown on (001) Silicon substrate," IEEE Trans. Electron Devices Vol. 39, p. 2082, 1992.

[Mcs53] H. J. McSkimin, "Measurement of elastic constants at low temperatures by means of ultrasonic waves," *J. Appl. Phys*. Vol. 24, p. 988, 1953.

[Miy93] H. Miyata, T. Yamada, and D. K. Ferry, "Electron transport properties of a strained Si layer on a relaxed $Si_{1-x}Ge_x$ substrate by Monte Carlo simulation," *Appl. Phys. Lett*. Vol. 62, p. 2661, 1993.

[Man91] T. Manku and A. Nathan, "Energy-band structure for strained p-type $Si_{1-x}Ge_x$," *Phys. Rev.* **B** 43, p. 12634, 1991.

[Mon76] H. J. Monkhorst and J. D. Pack, "Special points for Brillouin-zone integration," *Phys. Rev*. **B** 13, p. 5188, 1976.

[Mur95] S. Murtaza, R. Mayer, M. Rashed, A. Choudhury, D. Kinosky, C. Maziar, S. K. Banerjee, A. F. Tasch, Jr., J. Bean, and J. Campbell, "Room temperature electroabsorption in a $Si_{1-x}Ge_x$ PIN photodiode," *IEEE Trans. Electron Devices*, vol. 41, p. 2297, 1995.

[Nau92] K. Nauka, T. I. Kamins, J. E. Turner, C. A. King, J. L. Hoyt and J. F. Gibbons, "Admittance spectroscopy measurements of band offsets in $Si/Si_{1-x}Ge_x$ heterostructures," *Appl. Phys. Lett*. Vol. 60, p. 195, 1992.

[Ott75] G. Ottaviani, L. Reggiani, C. Canali, F. Nava, and A. Alberigi-Quaranta, "Hole drift velocity in silicon," *Phys. Rev.* **B** 12, pp. 3318-3329, 1975.

[Peo84] R. People, J. C. Bean, D. V. Lang, A. M. Sergent, H. L. Störmer, K. W. Wecht, R. T. Lynch, and K. Baldwin, "Modulation doping in Ge_xSi_{1-x}/Si strained-layer heterostructures," *Appl. Phys. Lett.*, vol. 45, p. 1231, 1984.

[Peo86] R. People, "Physics and applications of Ge_xSi_{1-x}/Si strained-layer heterostructures," *IEEE J. of Quantum Electronics*, vol. 22, p. 1696, 1986.

[Per81] J. P. Perdew and A. Zunger, "Self-interaction correction to density-functional approximations for many-electron systems," *Phys. Rev.* **B** 23, p. 5048, 1981.

[Pri79] P. J. Price, *Semiconductors and Semimetals* (Academic, New York), p. 249, 1979.

[Ren82] S. Y. Ren, J. D. Dow, and D. J. Wolford, "Pressure dependence of deep levels in GaAs," *Phys. Rev.* **B** 25, p. 7661, 1982.

[Ric86] S. L. Richardson, M. L. Cohen, S. G. Louie, and J. R. Chelikowsky, "Conduction-band-edge charge densities in elemental and compound semiconductors," *Phys. Rev.* B 35, p. 1388, 1987.

[Rid77] B. K. Ridley, "Reconciliation of the Conwell-Weisskopf and Brooks-Herring formulae for charged-impurity scattering in semiconductors," *J. Phys. C.* Vol. 10, p. 1589, 1977.

[Sop94] S. Vandebroek, E. Crabbe, B. S. Meyerson, D. Harame, P. J. Restle, J. M. C. Stork, and J. Johnson, "SiGe-channel heterojunction p-MOSFET's," IEEE, Trans. Elec. Dev., Vol. 41, p. 90, 1994.

[Tak92] S. Takagi and A. Toriumi, IEDM Tech. Dig. p. 711, 1992.

[Tan83] J. Y. Tang and K. Hess, "Theory of hot electron emission from silicon into silicon dioxide," *J. Appl. Phys.* Vol. 54, p. 5139, 1983.

[Tsu73] R. Tsu and L. Esaki, Appl. Phys. Lett. Vol. 22, p. 562, 1973.

[Van86] C. G. Van de Walle and R. M. Martin, "Theoretical calculation of heterojunction discontinuities in the Si/Ge system," *Phys. Rev.* **B** 34, p. 5621, 1986.

[Van89] C. G. Vand de Walle, "Band lineups and deformation potentials in the model-solid theory," *Phys. Rev.* **B** 39, p. 1871, 1989.

[Vog92] T. Vogelsang and W. Hänsch, "A novel approach for including band-structure effects in a Monte Carlo simulation of electron transport in silicon," *J. Appl. Phys*. Vol. 70, p. 1492, 1992.

[Wan93] X. Wang, V. Chandramouli, C. M. Maziar, and Al F. Tasch Jr., "Simulation program suitable for hot carrier studies: an efficient multiband Monte Carlo model using both full and analytic band structure description for silicon," *J. Appl. Phys*. Vol. 73, p. 3339, 1993.

[Yam95] T. Yamada and D. K. Ferry, "Monte Carlo simulation of hole transport in strained $Si_{1-x}Ge_x$," Vol. 38, pp. 881-890, 1995.

[Yam96] S. Yamakawa, *et al*. "Study of interface roughness dependence of electron mobility in Si inversion layers using the Monte Carlo method," J. App. Phys. Vol. 79, p. 911, 1996.

[Yeo94] K. Yeom, John M. Hinckley, and J. Singh, "Theoretical study on threshold energy and impact ionization coefficient for electrons in $Si_{1-x}Ge_x$," *Appl. Phys. Lett*. Vol. 64, p. 2985, 1994.

[Yu97] B. Yu, C. H. J. Wann, E. D. Nowak, K. Noda and C. Hu, " Short-channel effect improved by lateral channel engineering in deep-submicrometer MOSFE's," IEEE Trans. Electron Devices, Vol. 44,, No. 4, pp. 627-634, 1997.

[Zim60] J. M. Ziman, *Electrons and Phonons*, clarendon Press, Oxford, chap, IV, 1960.

VITA

Xin Wang was born in Shanghai, China on November 26, 1969. After completing his senior high school education at Shanghai No. 2 middle school, he entered Shanghai Jiaotong University as an applied physics major in 1988. He obtained the B.S. degrees in both applied physics and electrical engineering in June 1992. He directly joined the graduate school in the same university exemption without the admission examination due to his excellent performance in undergraduate study. His research area was on long-range electron-phonon correlation and Peierls dimerization in the one-dimensional molecular-crystal model. He obtained the M.A. degree in applied physics in spring 1995 under the supervision of Dr. Hang Zheng. In the same year, he joined the Department of Physics at University of Houston as a graduate student to study the direct solution to the X-ray phase problem supervised by Dr. W. P. Su. And obtained the M.S. degree in summer 1997. He started working with Dr. Sanjay Banerjee toward the doctoral degree in electrical engineering in 1997. He is the member of IEEE, APS and MRS.

Permanent address: 3517 North Hills Dr. Apt.# DD103
Austin, TX 78731

This dissertation was typed by the author.